ISBN 978-82-326-7592-0 (printed ver.)
ISBN 978-82-326-7591-3 (electronic ver.)
ISSN 1503-8181 (printed ver.)
ISSN 2703-8084 (electronic ver.)

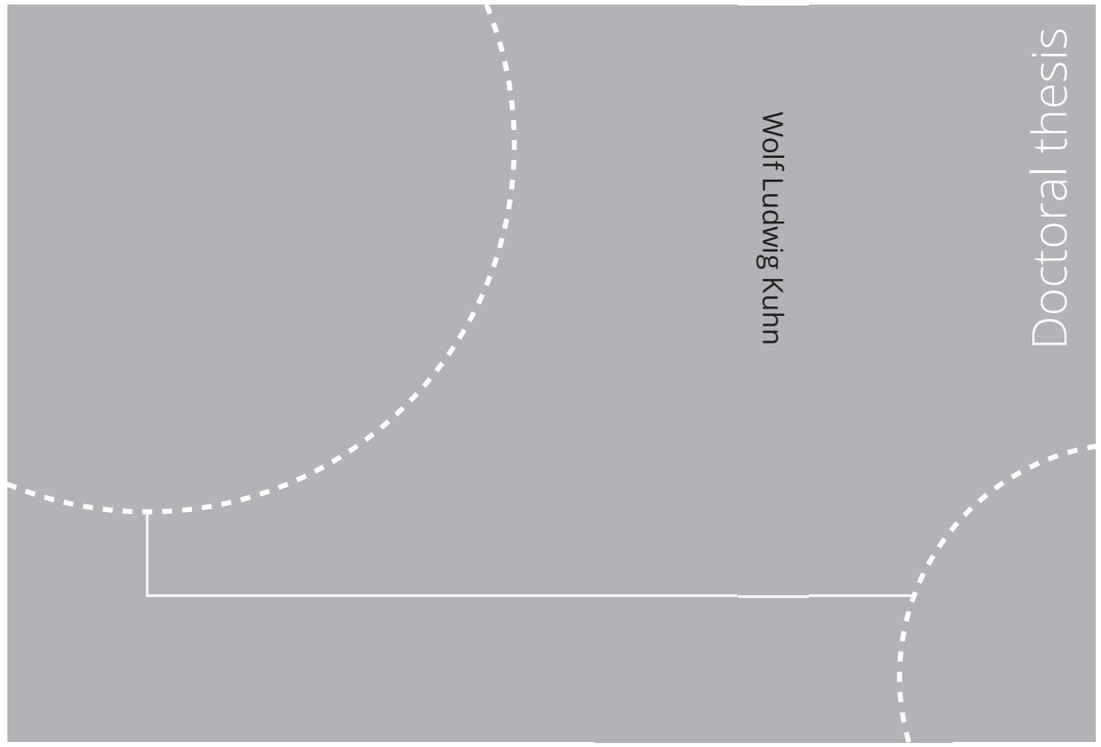

Doctoral theses at NTNU, 2023:445

Wolf Ludwig Kuhn

Evaluation of ultrasonic degasification as a tool to mitigate total dissolved gas supersaturation downstream hydropower plants

NTNU
Norwegian University of
Science and Technology

Doctoral theses at NTNU, 2023:445

NTNU
Norwegian University of
Science and Technology
Thesis for the degree of
Philosophiae Doctor
Faculty of Engineering
Department of Energy and Process Engineering

NTNU
Norwegian University of
Science and Technology

Wolf Ludwig Kuhn

Evaluation of ultrasonic degasification as a tool to mitigate total dissolved gas supersaturation downstream hydropower plants

Thesis for the degree of Philosophiae Doctor

Trondheim, December 2023

Norwegian University of Science and Technology
Faculty of Engineering
Department of Energy and Process Engineering

NTNU
Norwegian University of
Science and Technology

NTNU
Norwegian University of Science and Technology

Thesis for the degree of Philosophiae Doctor

Faculty of Engineering
Department of Energy and Process Engineering

ISBN 978-82-326-7592-0 (printed ver.)
ISBN 978-82-326-7591-3 (electronic ver.)
ISSN 1503-8181 (printed ver.)
ISSN 2703-8084 (electronic ver.)

Doctoral theses at NTNU, 2023:445

PRINTED IN NORWAY
NO - 1598

NORDIC SWAN ECOLABEL
Printed matter
2041 0731

Printed by Skipnes Kommunikasjon AS

Only curiosity leads to knowledge.
- Johann Wolfgang von Goethe

To Sophie.
Thank you for being at my side.

Abstract

This Doctoral Thesis evaluates ultrasonic degasification as a potential tool for mitigating total dissolved gas (TDG) supersaturation in the river downstream a hydropower plant. The volumetric liquid-gas mass transfer coefficient, $k_L a$, is identified as a benchmark for comparing the efficiency of different parameters influencing liquid-gas mass transfer. Natural degasification in case of TDG supersaturation in a river downstream of a Norwegian hydropower plant is evaluated based on TDG saturation measurements, enabling the calculation of $k_L a$ through certain assumptions and simplifications. Laboratory experiments are conducted to explore the degasification of TDG supersaturated water in a controlled environment. A method is developed to increase TDG saturation levels in water for both small- and medium-scale experiments. This water is utilized to test the influence of selected parameters on liquid-gas mass transfer during degasification by technical methods, with a focus on ultrasonic degasification, in both a small-scale batch reactor and a medium-sized degasification test rig. The resulting $k_L a$ values are in agreement with literature, and ultrasonic degasification is identified as a highly effective method for increasing liquid-gas mass transfer, both in static and kinematic conditions, hence reducing TDG saturation levels. An empirical model, derived from batch reactor data and adjusted using test rig results, offers possibilities for estimations regarding application in real-world scenarios.

The study contributes to the understanding of important parameters driving liquid-gas mass transfer during degasification of TDG supersaturated, flowing water. In addition, it advances the understanding of the complexities of degasification mechanisms within formerly unknown fields of application. While offering significant insights, remaining questions, and emerging challenges highlight the necessity of further research. Collaborative efforts among academia, industry, and authorities are vital to expand knowledge, implementation, and regulatory frameworks, in order to enhance aquatic environmental protection and advance hydropower as an environmentally friendly technology. Continuing the pursuit of knowledge is encouraged to build upon the foundation this Thesis establishes.

Sammendrag

Denne doktorgradsavhandlingen er skrevet om undersøkelsen av akustisk avgassing som et potensielt verktøy for å dempe totalgassovermetning i elva nedstrøms et vannkraftverk. Den volumetriske væske-gass masseoverføringskoeffisienten, $k_L a$, er identifisert som et referansepunkt for å sammenligne effektiviteten til ulike parametere som påvirker væske-gass masseoverføring. Naturlig avgassing ved totalgassovermetning i ei elv nedstrøms et norsk vannkraftverk vurderes basert på totalgassmetningsmålinger, noe som muliggjør beregningen av $k_L a$ gjennom visse antakelser og forenklinger. Laboratorieeksperimenter utforsker deretter avgassingen av totalgassovermettet vann i et kontrollert miljø. En metode er utviklet for å øke totalgassmetningsnivåer i vann for både små og mellomstore forsøk. Vannet brukes for å teste påvirkningen av utvalgte parametere på væske-gass-masseoverføring under avgassing ved bruk av tekniske metoder i både en småskala reaktor og en mellomstor avgassingstestrigg, med fokus på akustisk avgassing. De resulterende $k_L a$-verdiene er i samsvar med litteraturen, og akustisk avgassing er identifisert som en svært effektiv metode for å øke væske-gass-masseoverføring, både under statiske og kinematiske forhold, og dermed reduserer totalgassmetningsnivåer. En empirisk modell, utledet fra reaktordata og justert ved hjelp av testriggresultater, gir muligheter for estimeringer angående anvendelsen i naturlige scenarier.

Denne studien forbedrer forståelsen av viktige parametere som driver væske-gass-masseoverføring under avgassing av totalgassovermettet, strømmende vann. I tillegg fremmer den forståelsen av kompleksiteten av avgassingsmekanismer innenfor tidligere ukjente bruksområder. Mens de tilbyr betydelig innsikt, fremhever gjenværende spørsmål og nye utfordringer nødvendigheten av pågående forskning. Samarbeid mellom akademia, industri og myndigheter er avgjørende for å utvide kunnskap, implementering og regelverk. Slike samarbeidsinnsatser er avgjørende for å beskytte vannmiljøet og fremme vannkraft som en miljøvennlig teknologi. Det oppfordres til å fortsette kunnskapsøkningen ved å bygge på grunnlaget denne avhandlingen etablerer.

Zusammenfassung

Diese Doktorarbeit evaluiert akustische Entgasung als ein potentielles Werkzeug zur Abmilderung von Totalgasübersättigung im Fluss stromab eines Wasserkraftwerks. Der volumetrische Flüssigkeits-Gas-Massentransportkoeffizient, $k_L a$, wird als Bezugsgröße für die Vergleichbarkeit von unterschiedlichen Parametern identifiziert, welche den Massentransport zwischen Flüssigkeit und Gas beeinflussen. Die natürliche Entgasung im Falle von Totalgasübersättigung in einem Fluss stromabwärts eines norwegischen Wasserkraftwerks wird anhand von Totalgassättigungsmessungen bewertet und ermöglicht die Berechnung von $k_L a$ unter Zuhilfenahme bestimmter Annahmen und Vereinfachungen. In Laborexperimenten wird daraufhin die Entgasung von totalgasübersättigtem Wasser unter kontrollierten Bedingungen untersucht. Es wird eine Methode entwickelt, um den Grad der Totalgassättigung in Wasser sowohl für kleine als auch mittelgroße Experimente zu erhöhen. Mithilfe dieses Wassers wird der Einfluss ausgewählter Parameter auf den Flüssigkeits-Gas-Stofftransport bei der Entgasung mit technischen Methoden, mit Schwerpunkt auf akustischer Entgasung, sowohl in einem kleinen Reaktor als auch in einem mittelgroßen Entgasungsprüfstand getestet. Die resultierenden $k_L a$-Werte stimmen mit der Literatur überein, und die akustische Entgasung wird als hochwirksame Methode zur Erhöhung des Flüssigkeits-Gas-Massentransfers sowohl unter statischen als auch kinematischen Bedingungen identifiziert. Somit folgt eine Reduzierung des Totalgassättigungsniveaus. Ein empirisches Modell, abgeleitet aus experimentellen Daten aus den Reaktorexperimenten und angepasst anhand von Prüfstandsergebnissen, bietet die Möglichkeit für Abschätzungen hinsichtlich der Anwendung in realen Szenarien.

Die Studie verbessert das Verständnis wichtiger Parameter, die den Flüssigkeits-Gas-Massentransfer während der Entgasung von totalgasübersättigtem, fließendem Wasser beeinflussen. Darüber hinaus fördert es das Verständnis der Komplexität von Entgasungsmechanismen in bisher unbekannten Anwendungsfeldern. Obwohl sie wichtige Erkenntnisse liefert, verdeutlichen verbleibende Fragen und neue Herausforderungen die Notwendigkeit fortlaufender Forschung. Gemeinsame Anstrengun-

gen zwischen Wissenschaft, Industrie und Behörden sind von entscheidender Bedeutung, um sowohl Wissen, Umsetzung und regulatorische Rahmenbedingungen zu erweitern, als auch den Schutz der Gewässerumwelt zu verbessern und Wasserkraft als umweltfreundliche Technologie voranzubringen. Es wird empfohlen, auf der Grundlage dieser Arbeit aufzubauen und das Streben nach Wissen fortzusetzen.

Preface

More than three years of studies led to the accomplishment of this Doctoral Thesis. It comprises work done between August 2020 and August 2023 within the Waterpower Laboratory and the Hydrogen Energy and Sonochemistry Laboratory, which are both placed at the Department of Energy and Process Engineering at the Norwegian University of Science and Technology (NTNU). The funding for this study was provided by the DeGas project (2020-2024, NFR#308747), which intends to raise the knowledge within the field of mitigating total dissolved gas (TDG) supersaturation generated by hydropower plants using technical methods. This has been achieved by generating experimental data, as well as through discussions with colleagues, peers, project collaborators, and supervisors from Norway and all over the world.

The following pages summarize a scientific journey characterized by the joys and sorrows of multidisciplinarity under ever-changing external circumstances. It is the author's hope that this work has an impact on the scientific community, industry, and policymakers nationally and abroad, as well as on the public reception of the hydropower sector. Furthermore, it shall inspire follow-up research and motivate future scholars to continue on the scientific path pioneered.

Alongside the Thesis, the author contributed to scientific publications in collaboration with different research groups and projects. One peer-reviewed journal publication was made possible by an invitation from James A. Crossman (BC Hydro, Canada), and led to a contribution to the following review:

- Li, P., Zhu, D. Z., Li, R., Wang, Y., Crossman, J. A., & Kuhn, W. L. (2022). Production of total dissolved gas supersaturation at hydropower facilities and its transport: A review. *Water Research, 223*, 119012. `https://doi.org/10.1016/j.watres.2022.119012`

Another peer-reviewed publication, which is under consideration for publication, was handed in at the International Symposium on "Current Research in Hydropower Technologies, CRHT-XI" in Kathmandu, Nepal, in 2023. Within this paper,

preliminary results from Chapter 3 of this Thesis, and the experimental methods of the degasification test rig described in Chapter 5 are presented:

- Kuhn, W. L., Solemslie, B. W., Hihn, J.-Y., & Dahlhaug, O. G. (n.d.). Evaluating natural degassing in a river to create a baseline for comparison to technical degassing methods. *IOP Journal of Physics: Conference Series*.

During the course of a workshop in Canada, organized by the HYCANOR project ("Partnership on Sustainable Hydropower in Canada and Norway"), another idea for a journal publication came to life. This is on a different, yet not less important aspect of hydropower, and is currently under review:

- Piczak, M. L., McAllister, K., Bottoms, J., Grenier, G., Harper, M., Jetter, C. N., Kuhn, W. L., Smith, D. A., Twardek, W. M., Sundt-Hansen, L. E., Crossman, J. A., Amundsen, P.-A., Cooke, S. J., Helland, I. P., & Power, M. (n.d.). A Winter Perspective on Fish in Hydropower Reservoirs. *Reviews in Fisheries Science and Aquaculture*.

In addition, more parts of this Doctoral Thesis are under preparation to be published in peer-reviewed journals. A full overview of the aforementioned publications, including their respective abstract, is found in Appendix B.

Acknowledgments

First, I want to express my gratitude to my main supervisor, Ole Gunnar Dahlhaug (professor at NTNU), who took me into the Waterpower Laboratory at NTNU. It has been a pleasure to be guided by you, with lots of liberties and yet the possibility to come to your office with any idea, problem, or thought in mind. Thank you for both opening doors and helping along the way. Secondly, I was privileged to receive support from my first co-supervisor, Jean-Yves Hihn (professor at the Université de Franche-Comté). Without this, the work presented would be far from being both complete and as consistent as it turned out to be. I really enjoyed the visits to Besançon, as well as your visits to Trondheim. Thank you for the long discussions and the shared brainstorming to develop the methods applied within this Thesis. Last, but not least, I want to thank my third supervisor, Bjørn Winther Solemslie (researcher at NINA, associate professor II at NTNU). Your support during the laboratory work at the Waterpower Laboratory, as well as for presentations, reports, and applications was worth a mint. I hope to have the opportunity to continue working in cooperation with all of you.

To my colleagues at the Waterpower Laboratory, I am grateful for stimulating discussions and exchange of valuable ideas at work, and for fun times and good memories off work. The same goes for the community of temporary scientific employees, both at the department and the entire NTNU, which I was fortunate enough to represent for two consecutive years in The interest organization for temporary scientific employees at NTNU (DION). Thanks to my fellow board members for the journey together during these periods.

Heartfelt thanks go to my family, which has supported me and my decision to go abroad, and my friends. Without you, I might not have had the strength to conduct this work. Lastly, I want to thank Sophie for the blessing of sharing my life with you. I could not have wished for a better partner to go with me through this time, facing similar problems and challenges and, at last, conquering them all. Thank you for being at my side, and for bringing joy to my life.

Thank you all.

Contents

List of Tables

List of Figures

List of Symbols

Greek

Symbol	Definition	Unit
α, β	model constant	
δ	diffusion layer thickness	m
δ_{TDG}	sensor time constant	s
ε	surface roughness	m
ρ	density	$\mathrm{kg\,m^3}$
τ	residence time	s
φ, Φ	mass flux	$\mathrm{kg\,m^{-2}\,s^{-1}}$

Latin

Symbol	Definition	Unit
a	interfacial area	$\mathrm{m^2\,m^{-3}}$
A, B, C	empirical constant	
c	molar concentration	$\mathrm{mol\,m^{-3}}$
C	mass concentration	$\mathrm{g\,m^{-3}}$
C_p	specific heat capacity	$\mathrm{J\,kg^{-1}\,K^{-1}}$
D	diameter	m
E_{pot}	potential energy	J
f	frequency	Hz
f_{D}	Darcy friction factor	
H	head	m
H_g	gross head	m
H_n	net head	m
k_G, k_L	partial transfer conductance	$\mathrm{m\,s^{-1}}$

$k_L a$	(volumetric) liquid-gas mass transfer coefficient	s^{-1}
K_H	Henry constant	$mol\,m^{-3}\,Pa^{-1}$
L	length	m
m	mass	kg
M	molar mass	$g\,mol^{-1}$
p	pressure	Pa (bar, mwc)
p_{atm}	atmospheric pressure	Pa (atm)
p_G	partial pressure	Pa
p_{TDG}	total dissolved gas pressure	Pa
p_{TGP}	total gas pressure	Pa
P	power	W
P_{ac}	acoustic power	W
P_n	net power	W
Q	volumetric flow rate	$m^3\,s^{-1}$
Q_a	air flow rate	$m^3\,s^{-1}$
R^2	coefficient of determination	
Re	Reynolds number	
S_{TDG}	TDG saturation	%TDG
t	time	s
T	temperature	°C, K
U_{cs}	cross-sectional flow velocity	$m\,s^{-1}$
v	mean flow velocity	$m\,s^{-1}$
V	volume	m^3
V_p	pump voltage	V
x, y	variable	
$\mathcal{X}$	mole fraction solubility	

Mathematical constants

Symbol	Definition	Value
e	Euler's number ($\exp x = e^x$)	2.71828
π		3.14159

Physical constants

Symbol	Definition	Value
g	gravitational acceleration	$9.8067\,m\,s^{-2}$

Subscripts

Symbol	Definition
a	air
ac	acoustic
atm	atmospheric
avg	average
A, B	at point A, B
$corr$	corrected
cs	cross-section
$bulk$	liquid bulk
e	end
g	gross
gas	gas
G	gas, gas phase
H	Henry
i	control variable
L	liquid, liquid phase
max	maximum
mdl	model
n	net
p	pump (except C_p)
pv	pressure vessel
pot	potential
s	start
set	set, setting
TDG	total dissolved gas
$\%$	share

Superscripts

Symbol	Definition
i	control variable
$*$	baseline value
$'$	deconvoluted value

List of Acronyms

CAD	computer-aided design
CFD	computational fluid dynamics
DAQ	data acquisition
DO	dissolved oxygen
GBD	gas bubble disease
GCM	general circulation models
NFR	Norges Forskningsråd
NI	National Instruments
NORCE	Norwegian Research Centre
NTNU	Norges teknisk-naturvitenskapelige universitet
NVE	Norges vassdrags- og energidirektorat
RCP	representative concentration pathway
TDG	total dissolved gas
TGP	total gas pressure

List of Terms

The definitions of the terms used in this Doctoral Thesis are taken from *A Dictionary of Mechanical Engineering* (Escudier and Atkins, 2019), if not specified otherwise.

Catchment area

The area of land from which water flows into a river, lake, or reservoir (CUP, 2023a).

Cavitation

The formation of vapour- or gas-filled cavities in a liquid due to reduction of the local pressure, often due to acceleration of the fluid, such as in flow through a convergent nozzle.

Concentration

The exact amount of one particular substance that is found in another substance (CUP, 2023b).

Deconvolution

A process of resolving something into its constituent elements or removing complication in order to clarify it (O'Haver, 2023).

Degasification

The removal of dissolved gases from liquids.

Diffuser

A duct or nozzle in which the kinetic energy of a flow is converted into pressure energy.

Discharge

The act of sending out waste liquid or gas (CUP, 2023c).

Dissolution

The process where a solute in gaseous, liquid, or solid phase dissolves in a solvent to form a solution (Lu et al., 2023).

Efficiency

A measure of the performance of a machine or system, the ratio of the actual performance to the theoretical performance.

Environmental flow

The hydrological regime required to sustain freshwater and estuarine ecosystems (Acreman, 2016).

Flow rate

The rate at which fluid, or fluid-borne solid particles, flows through a pipe, duct, flow meter, or machine.

Frequency

The number of cycles per second in an oscillation or the repetition rate for a cyclic process.

Friction

The resistance that a body encounters when sliding over another body, or experiences when a viscous fluid flows over its surface.

Head

A pressure difference Δp expressed in terms of the vertical height of a column of liquid.

Head loss

A loss in stagnation pressure in internal flow due to wall friction and minor losses in fittings.

Headrace

An open channel or tunnel that conveys water into a hydraulic turbine.

Hydropower

The shaft power generated by a hydraulic turbine from a head of water, either for generating electricity or for direct mechanical purposes.

Load

The power drawn from an engine or mechanism that transforms thermal, chemical, electrical, pressure, or any other source of energy into mechanical energy.

Mean

The result you get by adding two or more amounts together and dividing the total by the number of amounts (CUP, 2023d).

Median

The median value is the middle one in a set of values arranged in order of size (CUP, 2023e).

Morphology

The form, shape, or structure of a stream or organism (TPWD, 2023).

Nozzle

A duct, usually circular and of varying cross section, through which there is flow.

Penstock

An enclosed pipe, which may include a gate and a valve, that delivers high pressure water to the inlet of a hydraulic turbine.

Power

The rate at which work is done on or by a system or device.

Rated capacity

The maximum power output that can be sustained continuously for any power-producing machine or system, such as an engine or a power plant.

Residence time

The average length of time during which a substance, a portion of material, or an object is in a given location or condition.

Saturation

The degree to which something is dissolved in something else, compared with the maximum possible degree (CUP, 2023f).

Solubility

The maximum concentration of solute that may be added to a solvent without formation of a new phase.

Specific speed

A non-dimensional quantity used to characterize turbomachinery performance.

Spillway

An open channel used for the controlled release of excess water flow, e.g. from a dam.

Stator

A ring of non-rotating blades or nozzles in a compressor, turbine, or other turbomachine, which directs fluid flow into an adjacent rotor.

Steady state

A process or motion which is independent of time.

Tailrace

An open channel or tunnel that conveys water away from a hydraulic turbine.

Tidal power

Power that comes from the movement of the tide and that can be used especially for producing electricity (CUP, 2023g).

CHAPTER

ONE

Introduction

The world experiences an accelerating change of climate fueled by man-made emissions of greenhouse gases (IPCC, 2023). This produces a need for reducing these emissions by implementing policies, adapting industries, and changing lifestyles. Especially the transition towards low- or zero-emission energy production has been in focus in recent years, as burning fossil fuels contributes to a large extent to greenhouse gas emissions (IPCC, 2013). Hydropower plays an important role on the way towards these goals (Berga, 2016; Wasti et al., 2022). Even though considered a "green", i.e. renewable, energy, the construction and operation of hydropower plants create changes for, and potentially increase endangerment of the aquatic ecology (Alp et al., 2020; Botelho et al., 2017; Zarfl et al., 2019).

One such threat is total dissolved gas (TDG) supersaturation, which brings a silent and short-termed, yet dangerous alteration of the water used as a habitat for fish and other aquatic lifeforms. TDG supersaturation defines the surplus of the sum of air-content gases above the usual concentration (Berg, 1992; Huang et al., 2010). Far from all existing hydropower plants are at risk of creating TDG supersaturation in water, but due to climate change, the number is expected to increase. While studying the occurrence and consequences of this problem is on the rise in countries with a large share of electricity generation from hydropower, methods to prevent or mitigate it need to be developed, too. From a civil engineering perspective, the research is already advanced (Li et al., 2022b; Pulg et al., 2018). Nevertheless, not all hydropower plants are capable of retrofitting the solutions offered. This is especially valid for Norway, where the topological conditions lead to a hydropower sector that differs a lot from the ones in most other hydropower-utilizing countries in the world (Graabak et al., 2017; Innovation Norway, 2023). Therefore, a need arises to find solutions available in other engineering disciplines.

Among these answers, reducing the TDG saturation level by ultrasonic degasification stands out. While being mainly applied to static or low-kinematic solutions in a broad range of fields, the use of degasification in a highly kinematic environment has not been studied to-date. Those situations impose challenging problems, as e.g. the exposure time decreases drastically. Within the DeGas project (2020-2024, Norges Forskningsråd (NFR)#308747), a knowledge-building project funded by the NFR and several Norwegian hydropower companies, the focus was set on studying the application of different degasification methods within such a kinematic setting. The research is conducted by multiple Norwegian research institutes under the lead of the Norwegian University of Science and Technology (Norges teknisk-naturvitenskapelige universitet (NTNU)). The project consists, besides the experimental studies of the aforementioned methods, of the development of numerical tools to predict the outcome of the degasification method depending on parameters given by the power plant's operation, the numeric simulation of the distribution of TDG supersaturation within the waterways downstream the power plant, and the evaluation of biological consequences of the degasification.

This Thesis is a compilation of the results from the experimental research conducted within the DeGas project, with a focus on ultrasonic degasification. To provide a thorough understanding of the principles from both fields of hydropower and liquid-gas mass transfer, a separate chapter comprising the relevant background and literature is following this introduction (Chapter 2). While the hydropower part focuses on the mechanisms leading to the generation of TDG supersaturation by hydropower plants, as well as the status within Norway and the future perspectives in light of climate change, the physio-chemical basics are focussing on the principle mechanisms of liquid-gas mass transfer, and possibilities to increase the mass transfer, with a focus on ultrasonic degasification. It concludes with the gap in knowledge of applying technical methods other than of civil engineering nature to hydropower, to achieve mitigation of TDG supersaturation. Afterwards, the Thesis addresses the following topics in depth:

1. the volumetric liquid-gas mass transfer coefficient during natural degasification in a river downstream a hydropower plant (Chapter 3),
2. the influence of selected operating parameters on the volumetric liquid-gas mass transfer coefficient during small batch reactor experiments (Chapter 4), and
3. the production and degasification of TDG supersaturated, flowing water using power ultrasound during medium-sized experiments (Chapter 5).

The methods needed to achieve the results of each chapter are described in detail, followed by a presentation and discussion of the outcome. All laboratory studies are conducted within laboratories at the Department of Energy and Process Engineering at NTNU, using both existing and tailor-made equipment to conduct the experiments.

In addition to the individual discussions, the results from the individual chapters are summarized in a broad discussion (Chapter 6). The final conclusion (Chapter 7) is followed by a brief outlook (Chapter 8).

The study sheds light on the degasification mechanisms taking place in case of TDG supersaturation. By having the possibility to compare the processes taking place within three different situations with varying levels of scale, differences, challenges, and opportunities are identified. Moreover, the methods established give unique possibilities for further research, thus enabling a continued increase in knowledge.

CHAPTER
TWO

Background

This chapter starts with an introduction of hydropower and the design of hydropower plants, followed by the importance of hydropower in Norway, hydropower's role in the generation of total dissolved gas (TDG) supersaturation, the ecological consequences arising from it, and an overview of existing guidelines. Afterwards, the scientific background to solutions and concentration will be given, including an introduction to the topics of solubility and gas dissolution. This is used as a basis for introducing the volumetric liquid-gas mass transfer coefficient, which will be used as a comparison tool throughout the Thesis. Finally, methods to measure TDG saturation levels and enhance the degasification process are presented, including an overview of the currently used measures to prevent or mitigate TDG supersaturation generated by hydropower plants.

2.1 Hydropower

Within this section, the field of hydropower is described, including the design of hydropower plants, the importance of the sector in Norway to date and implications of climate change on it, as well as the generation of TDG supersaturation at or within hydropower plants. For the design part, the focus is put on the components of hydropower plants that are relevant for the occurrence of TDG supersaturation. Further information is found in textbooks, e.g. Breeze (2018), Brekke (2015) and Dixon and Hall (2014), which are also used to make this section.

2.1.1 Design of a hydropower plant

Hydropower plants are designed depending on the geographical and topological conditions at the side of the power plant (Blanchard, 1924; Breeze, 2018; Görtz et al., 2022), as well as ecological, social, and economical factors that have to be taken into account (De Faria et al., 2017; EIB, 2019; Pontoni et al., 2018). These factors and conditions will determine several parameters, on which the final

design of the power plant depends. The design process is iterative, meaning that after arriving at the first rough parameter estimations, feedback loops will provide constant improvement of the design parameters (Brekke, 2015).

In general, the generation of electrical energy using hydropower utilizes the potential energy, E_{pot}, of water at a certain height, H, above sea level, as calculated using Equation 2.1:

$$E_{\text{pot}} = mgH. \tag{2.1}$$

The theoretically available specific energy is defined by the gross head H_g, which is the height difference between the water level upstream and downstream the power plant. The net head, H_n, excludes head loss and is used to describe the energy that is available for the hydraulic turbine (Bergh, 2012). Using this, the available or net power for the hydraulic turbines in the power plant is calculated using, H_n, and the volumetric flow rate, Q:

$$P_n = \rho Q g H_n. \tag{2.2}$$

The derivation of Equation 2.2 is found in e.g. Dixon and Hall (2014).

Following the net power as a main target of the power plant's design, the design choices are mainly dependent on the availability of water, i.e. the volumetric flow rate or discharge, Q, and the height difference, H. The water that is available throughout the year at a specific location is determined by the catchment area, while the head is dependent on the location of the inlet and outlet of the power plant as well as the subsequent placement of the powerhouse. Afterwards, a choice will be made on the type of dam used in the project, the type and number of hydraulic turbines utilized to convert the energy into mechanical energy, and the subsequent design of the generator and transformer (Pereira, 2021).

Categorization of hydropower plants

A first and major distinction is made between a reservoir-type and a run-of-river power plant. In the former, a dam structure is used to create a reservoir of water which is used for the generation of electric energy inside the power plant. This type has the advantage of greater possibilities for regulation, but comes at high civil-engineering and ecological as well as social costs (in case of large projects). The amount of water available is largely determined by the reservoir size, making reservoir-type power plants more independent of variations in precipitation. Yet, these power plants are having cycles of reservoir-filling, often during spring, and -emptying, which takes place during dry seasons (Bakken et al., 2022; Breeze, 2018; Sommers, 2004).

Pumped-storage power plants are seen as a special type of reservoir power plants, as they are in need of both an upper and a lower reservoir for the respective

storage and release of energy. Here, both reservoirs do not necessarily need a catchment area to sustain a volumetric flow. A run-of-river project diverts parts of the flow of water from a river into the power plant. In comparison with a reservoir type, the ecological, social, and economical costs are lower, but the possibility of regulation is largely lost, as the water available is largely dependent on precipitation and snow or ice storage. A determination of the power plant's design starts therefore from a flow duration curve (J. Glover, 2022). While the aforementioned types of hydropower plants are land-based, hydroelectric generation may also occur on sea, e.g. from tidal power.

Another way to categorize hydropower plants is by the installed rated capacity. Here, a separation between micro, mini, small, and large power plants is made (Breeze, 2018). The respective capacity range for these categories is listed in Table 2.1. In Norway, the categories of small and large hydropower plants end and start at 10 MW, respectively (NVE, 2023).

Table 2.1: Categorization of hydropower plants by installed rated capacity (Breeze, 2018).

Category	Installed rated capacity
micro	1 kW to 100 kW
mini	100 kW to 1 MW
small	1 MW to 10 MW–30 MW
large	above 10 MW–30 MW

Dam

The dam is the main civil structure of a reservoir-type hydropower plant. It is used to block the natural flow of water along its riverbed, thus creating a large volume of water. Different types of dams exist, with the major categories being embankment, gravity, buttress, and concrete arch dam. The choice of dam is dependent on the geology and topography of the dam side and the requirements of the reservoir that is to be formed (Brandt et al., 2017; Breeze, 2018).

In addition to its major task of creating water storage, dams are used for flood control. During times of large run-off, e.g. during heavy rainfall events, dams and their reservoirs can play an important role in dampening and mitigating the water flow. For this purpose, each dam is equipped with gates that help regulate the water height in the reservoir. An emergency spillway assures that the dam is not breached in times of gate failures or extreme floods (Alfredsen and Bruland, 2022; Bakken et al., 2022).

Waterways

The waterways of a hydropower plant comprise the way of the water from the intake to the outlet. In most cases, an inlet or headrace tunnel will lead the water on a small decline toward the penstock, where the decline increases up to 90° (Breeze, 2018). Depending on the specific design of the power plant, it can be a singular or multiple penstocks. In difference to the headrace tunnel, which in Norway to-date usually is a rock-walled tunnel (in some cases with a concrete lining), the penstock is often formed as a steel pipe to reduce friction losses (Kumar, 2022). Within the junction between headrace tunnel and penstock, one or multiple surge tanks may be placed to reduce dynamic effects in case of emergency shutdowns (Killingtveit, 2019). The penstock ends in the powerhouse, where the hydraulic turbine(s), generator(s), and the transformer are placed. Finally, an outlet or tailrace tunnel will lead the water back to the waterways downstream the power plant (Breeze, 2018).

Cavernous power plants may have not only one, but multiple water reservoirs or streams feeding water into the system. If there are one or more minor, unregulated intakes, they are referred to as Brook or secondary intakes (Perzyna, 2017). Those may cause TDG supersaturation in case their intake rists get clogged, or during flood situations (Pulg et al., 2018).

Turbine

The hydraulic turbine of the hydropower plant is the major contributor to the energy transfer. In all cases, the energy contained within the water (both potential and kinetic) will be used to drive the hydraulic turbine, thus creating a rotational motion. Different hydraulic turbine designs are available, which mainly depend on the net head, H_n, and the discharge, Q (Brekke, 2015). Within modern hydropower plants, hydraulic turbines are divided into the main categories impulse and reaction turbines. The most used types within those categories are Pelton turbines for the former and Francis and Kaplan turbines for the latter category. An overview of the working areas of these three turbines in dependency of head and discharge is given in Figure 2.1 (Dixon and Hall, 2014).

In an impulse turbine, the pressure drop takes place entirely in the turbine stator, where the specific energy is completely converted to kinetic energy. The turbine stator is in this case one or multiple nozzles, which release a jet of water that is directed onto the turbine blade. In addition, the nozzle is used for regulating the turbine by changing the volumetric flow through opening and closing of a needle valve. The energy transfer within the turbine is introduced by impulse forces, i.e. the change of direction of the velocity vectors within the turbine blade (Dixon and Hall, 2014). Due to this working principle, a characteristic of impulse turbines is the operation in free air, as partial or full submergence would create drag forces

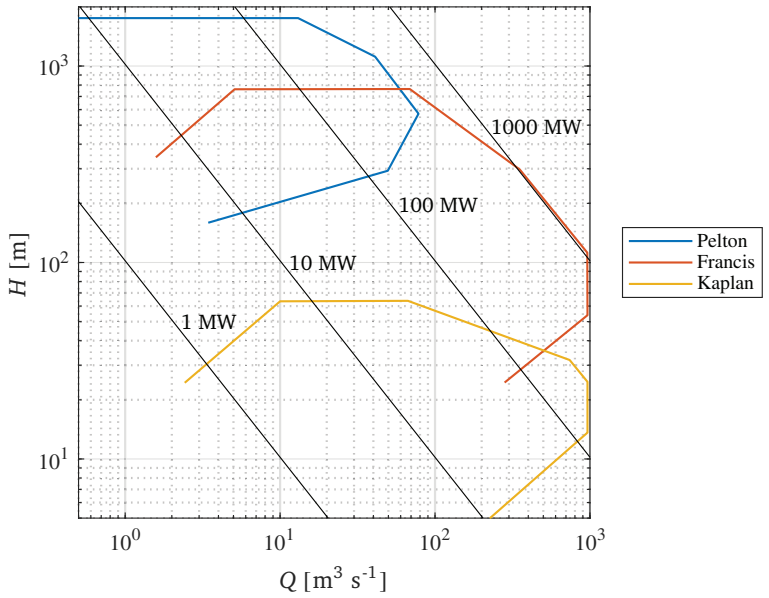

Figure 2.1: Working areas of the three major types of hydraulic turbines in dependence of head, H, and discharge, Q, with lines of constant power calculated using Equation 2.2 (adapted from Dixon and Hall (2014)).

(Breeze, 2018). Impulse turbines operate at low specific speeds and medium- to high-heads. They have a very distinct peak efficiency and therefore do not operate well in part-load (Brekke, 2015; Dixon and Hall, 2014).

Reaction turbines on the other hand work by using the pressure difference between turbine inlet and outlet. Here, the specific energy is partly made up by the pressure energy at the inlet, which is then converted to kinetic energy. The energy transfer is then happening by the change of direction of flow in addition to the pressure difference (Brekke, 2015; Dixon and Hall, 2014). A reaction turbine is usually fully immersed (Breeze, 2018), with water entering radially from the stator (in case of Francis turbines on the entire circumference of the turbine, with an exit of the flow in axial direction). The stator is usually made up by a spiral chasing with stay vanes, leading to a uniform inflow. In addition, guide vanes or adjustable wicket gates are used for regulation of the turbine. Some reaction turbines, e.g. Kaplan turbines, have the additional possibility to regulate the operation by adjustable turbine blades. Downstream the turbine, a draft tube acts as a diffuser to create additional suction (Dixon and Hall, 2014). Reaction turbines operate at higher specific speeds than impulse turbines, but are used for lower heads (this applies especially to Kaplan turbines). Their peak efficiency can be higher than that of

impulse turbines, and some of them operate well in part-load (Brekke, 2015; Dixon and Hall, 2014).

2.1.2 Status in Norway

The Norwegian climate, topography, and geology are ideal for the exploitation of hydropower. About 40 % of the land mass lies above elevations of 600 m (Graabak et al., 2017), and the average annual precipitation for the period of 1991-2020 was 1122 mm, well above the European average of 827 mm in 2020. What the average does not show is a distinct division between a drier inland in the east and the western coastline, where the annual precipitation can reach above 2000 mm (World Bank Group, 2021). In addition, evaporation is low due to the latitudinal position and the subsequent colder climate. Another factor that favors hydropower in Norway is the solid rock mass that is found in the majority of the country (Basnet and Panthi, 2018).

All those factors helped in the early hydropower development in the late 19th century. Since then, there has been a continuous growth in both number of power plants and total installed capacity (NVE, 2017). In 2022, a total of 33 391 MW capacity was installed in hydropower plants in Norway. This is the highest number in Europe and the 7th highest in the world (IHA, 2022). To date, about 90 % of all electricity generated in Norway stems from hydropower (OED, 2023).

The Norwegian Water Resources and Energy Directorate (Norges vassdrags- og energidirektorat (NVE)) lists all hydropower plants in Norway in a database. A total of 1799 hydropower plants, including 32 pumped-storage power plants, are listed as of May 05th, 2023 (NVE, 2023). Those power plants are categorized using the installed rated capacity presented in Table 2.1. The results in Table 2.2 show the importance of large hydropower plants for the electricity generation in Norway. As almost all the projects with large potential have been developed already, the trend has in recent years moved towards the implementation of power plants with a capacity of less than 10 MW, in addition to refurbishing and upgrading of existing projects (Bakken et al., 2012).

Table 2.2: Number of hydropower plants by category in Norway, including installed capacity and average annual production (1991-2020) per category (NVE, 2023).

Category	Number	Installed capacity [MW]	Average annual production [TWh]
micro	240	10.85	0.04
mini	355	194.42	0.72
small	829	3153.89	11.22
large	343	30 352.88	125.16

Using the knowledge about the Norwegian topography providing medium head sizes and the importance of power plants with large capacities, an analysis of Figure 2.1 reveals that most of the Norwegian power plants utilize Francis turbines. In fact, a feature of Norwegian hydropower is the use of high-head Francis turbines, i.e. Francis turbines operating with a head of > 300 m, which account for about 40 % of the installed capacity from Francis turbines in the Nordics (Ellefsrød et al., 2016). The Norwegian landscape with its large number of natural reservoirs provides another advantage that more recently increased in importance: the possibility for energy storage in pumped-storage hydropower plants. The total capacity for storing energy in existing hydropower reservoirs is currently 87 TWh, which is about 50 % of the European electricity storage capacity (Jensen et al., 2022). Upgrading existing reservoir-type hydropower plants to pumped-storage type hydropower plants and implementing new projects could allow for flexible timescales of providing energy ranging between a few hours and up to months. A potential of about 60 GW pumped storage hydropower plant capacity has been estimated to exist in Norway (Charmasson et al., 2018), even though less than 1.5 GW capacity are currently installed (Pitorac et al., 2020). These features are giving Norway a unique position within Europe, as other mountainous regions lack the special topography to implement pumped-storage hydropower at a similar scale (Charmasson et al., 2018).

The potential for pumped-storage hydropower plants makes the Norwegian hydropower system a key player in the upcoming energy transformation towards emission-free electricity generation. Using the storage function, it is possible to (partially) store intermittent energy sources such as wind and solar power generated in northern, central, and western Europe. Thus, some call Norway the "green battery" of Europe (Gøtske and Victoria, 2021; Graabak et al., 2017; Gullberg, 2013; Skar et al., 2018). The interconnection with other European countries' electricity grids by landlines and subsea cables already has a capacity of 9 GW (Jensen et al., 2022). To fulfill the task of fully flexible storing and releasing energy from Norwegian hydropower reservoirs, the interconnectivity has to increase further. Alvik et al. (2022) expect the transmission capacity between Norway and other European countries to increase by 5 GW during the 2030s, while Skar et al. (2018) estimate the capacity to be 27.8 GW by 2050 in a modeled baseline scenario. Thus, the transition towards renewable energies and the inclusion of the Norwegian hydropower storage capacity into the European energy market needs both national and international efforts and cooperation.

But Norwegian hydropower does not only give possibilities to even out energy fluctuations in a larger European perspective, it also provides base load opportunities for the Norwegian power market. With wind and solar power making up a rising share of the power production in Norway as well, and expected capacity increases of

43.9 GW wind (thereof 7.5 GW onshore and 36.4 GW offshore) and 10.7 GW solar power by 2050 (Skar et al., 2018), fluctuations in the electricity grid are expected to grow. This has to be countered by large, rotating masses, as they are found in large hydropower plants' generators, evening out the fluctuations. A different problem arising from this is the change in operational patterns to more flexible operations, thus leading to increased stresses and reduced lifetime of hydraulic turbines (Skorpen, 2018).

2.1.3 Effects of climate change

Hydropower operations are dependent on inflow conditions and, in temperate regions, water storage. Snowpack or permanent ice storage has important implications for the rule curves that drive reservoir and hydropower operation, particularly reservoir refill during the winter months (Mo et al., 2018). In addition, hydropower makes operational flood control during high runoff events possible (Hansen, 2018). The global climate changes due to increased emission of greenhouse gases since the industrial revolution and the subsequent increase in radiative forcing (IPCC, 2013), which leads to rising temperatures. Changes are observed worldwide, but impacts show regional and seasonal differences, e.g. temperate climates experiencing a general trend towards warmer and wetter winters (Hanssen-Bauer et al., 2017). The associated change in water availability throughout the year could lead to operational regimes outside the original scope for many hydropower systems. But rising temperatures also implicate additional changes for the hydropower industry, such as changes in precipitation and runoff extremes or increased water demand and evaporation. This in combination with changes in wind extremes leads to different operation of dams and may affect their structural integrity and safety (Jjunju et al., 2022; Wasti et al., 2022).

The projection of climate changes throughout the 21st century is established by using modeling techniques such as general circulation models (GCM). Even though modeling outcomes are highly uncertain and dependent both on the climate model itself and the representative concentration pathway (RCP) used for the prediction (Hagemann et al., 2013), a general prediction is possible by taking larger numbers of studies into account. Doing this shows a general increase in land-based temperatures in the northern hemisphere, with higher increases in higher latitudes. In addition, a much faster warming in winter than in summer is predicted (Hansen et al., 2014; Kreyling et al., 2019; Mayer et al., 2023; Smalås, 2021; USEPA, 2021b; Wang et al., 2021).

The overall conclusion of precipitation modeling is an increase in precipitation and subsequent river runoff for northern mid and high latitudes, as reported e.g. in Lehner et al. (2005) for Scandinavia and northern Russia, van Vliet et al. (2016) for North America, northern Europe and northern Asia, Turner et al. (2017) for Scandinavia and central Asia, and Gøtske and Victoria (2021) for Northern

Europe. A problem poses the predicted seasonal variation of precipitation, as the increases in runoff are expected to generally coincide with high flow seasons, thus increasing flooding potential (Arnell, 2004). In connection with rising winter temperatures, another change affecting hydropower operations is a decrease in the snow-to-precipitation ratio. This has been reported for northern U.S. weather stations for the period from 1949. As a result, precipitation in winter is increasingly appearing as rain instead of snow. This corresponds with a decrease in seasonal snowpacks and a subsequent time shift in reservoir inflow (USEPA, 2021b). Similar developments have been observed elsewhere, as summarized by Wasti et al. (2022). Increased precipitation as rain in winters combined with earlier snowmelt in spring will make water availability in the drier months more difficult to manage, with storage depending on reservoir size. While larger reservoirs may be able to buffer some inflow variability, reservoirs with small storage capacity are more easily overwhelmed during periods of elevated inflows, either through rapid snowmelt or more intense storms, and therefore are not as effective in regulating inflow variability (Ehsani et al., 2017).

An additional effect of climate change is revealed by historical data from lakes in North America and Europe, which shows a general increase in lake surface temperature over time due to rising air temperatures. This leads to increased restrictions for native and possible advantages for invasive species using lakes and hydropower reservoirs as their habitat (Dokulil et al., 2021; USEPA, 2021a). In addition, river water temperatures are projected to be elevated as well (van Vliet et al., 2016; van Vliet et al., 2013). This will directly influence the solubility of gases in the water[1].

Summarizing, the effects of climate change on hydropower in northern hemispheres are projected to be primarily increased surface and water temperatures, and subsequent decreased snow-to-precipitation ratio in winter, including a shift in inflow patterns. Furthermore, increased precipitation is predicted, and thus increased runoff extremes. Especially the latter will affect the occurrence of TDG supersaturation events. While the predicted temperature increases in water will decrease the solubility of gases in water, this effect has only a minor influence on the generation and degasification of TDG supersaturation in the river.

2.1.4 Hydropower-induced total dissolved gas supersaturation

The design parameters for a hydropower plant, head, H, and discharge, Q, as described in Section 2.1.1, allow for the generation of TDG supersaturation. This term describes the state where too much gas is dissolved in a liquid in relation to the ambient pressure of the system[2]. With the solubility of air-content gases being directly proportional to the pressure, a power plant with a medium- or high-head

[1]The solubility of gases is described in Section 2.2.1.

[2]For a detailed description of the dissolution process of gas in a liquid refer to Section 2.2.1.

allows for a large increase in air solubility. The prerequisites for creating TDG supersaturation are, besides a higher pressure, the intrusion of air into the system and a certain residence time.

In addition, only hydropower plants with immersed hydraulic turbines are known to cause TDG supersaturation. Therefore, power plants using Pelton turbines are rarely experiencing this problem[3]. Kaplan turbines are used for lower heads and larger discharges, meaning that the dissolution of possibly entrained air in the water will not happen to a large extent due to low pressure and residence times. Thus, TDG supersaturation is also not common in power plants utilizing Kaplan turbines. Subsequently, most hydropower plants with occurrence of TDG supersaturation are utilizing Francis turbines.

Generation of total dissolved gas supersaturation

Three ways of TDG supersaturation in rivers generated by hydropower plants are reported in the literature. The first one is the creation at high dams during flood discharge. Here, gate operations lead to the release of usually large volumes of water over the dam spillway into the plunge pool below the dam. If during this process air bubbles are entrained into deep water, the hydrostatic pressure and the subsequently increased solubility of air lead to dissolution of the air-content gases. During the transport downstream, this water will eventually leave the areas of larger hydrostatic pressure and therefore show a supersaturation of the TDGs. A review of known hydropower plants producing TDG supersaturation is found in Li et al. (2022b).

The described type of TDG supersaturation induced by hydropower plants into the downstream waterways is the first one reported by literature by reports from the Lower Columbia River system in the 1960s (Weitkamp and Katz, 1980). The reason was quickly identified as spring spill operations for flood relief, e.g. at Bonneville Dam (Schneider and Barko, 2006). An illustration of this process is given in Figure 2.2. Additional cases of TDG supersaturation in the waterways downstream high dams are known from other parts of the USA (Orlins and Gulliver, 2000; Witt et al., 2017), Canada (Kamal et al., 2016; Kamal et al., 2019; Kamal et al., 2020), China (Chen et al., 2022; Huang et al., 2016; Huang et al., 2010; Ma et al., 2013; Ou et al., 2016; Zhang et al., 2022; Zhang et al., 2017), and recently from Brazil (Agostinho et al., 2021; Ovelar et al., 2022). This way of generating TDG supersaturation usually takes place at large rivers with a flow rate $\geq 1000\,\mathrm{m^3\,s^{-1}}$ (Pulg et al., 2018).

The second way of hydropower plants to cause TDG supersaturation is taking place due to air intrusion into the power plant's waterways and the subsequent exposure to high pressure leading to air dissolution. At high dams, air needs to be

[3]For a detailed description of degasification enhancement due to aeration, refer to Section 2.3.2.

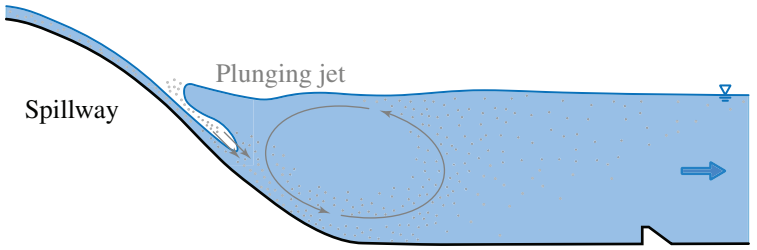

Figure 2.2: An example of air entrainment during spill operations at a hydropower plant's dam and subsequent creation of TDG supersaturation (adapted from Politano et al. (2016)).

entrained and drawn down into a certain depth to reach the intake and thereby make its way into the power plant. Within reservoir-type power plants, the entrainment of air into the tunnels takes place at an intake. This process is mainly described by literature from Norway, where the first reports of TDG supersaturation were published in the 1970s. In the following years, numerous studies were conducted on this topic (Berg, 1992; Berg et al., 1984; Heggberget, 1984). The main reason for air intrusion into the power plants' tunnels was identified as underdimensioned brook intakes. Figure 2.3 displays a schematic of this process. Adjusted design guidelines as well as constructive measures, namely vacuum intakes, were introduced by the Norwegian authorities to prevent or reduce TDG supersaturation (Berg, 1987; Pulg et al., 2018). Increasing run-off extremes are expected to lead to more cases of TDG supersaturation in Norwegian hydropower plants in the future (as discussed in Section 2.1.3).

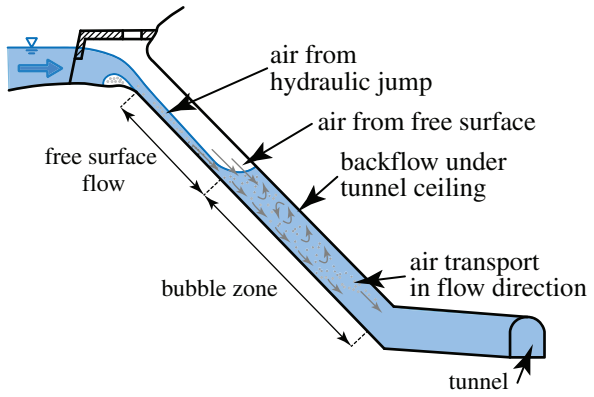

Figure 2.3: Schematic overview of air entrainment, due to a hydraulic jump and a free surface flow, at a deep shaft of a Brook intake (adapted from Stokkebø et al. (1988)).

The third way is an operational procedure called turbine aeration, which is used in hydropower plants with reaction turbines. This takes place to relieve the turbine in certain operational regimes from stresses coming from unsteady flow patterns or self-induced oscillations, or to avoid or decrease cavitation on the turbine runner. In addition, turbine aeration is used to regulate the dissolved oxygen (DO) content at reservoirs prone to Oxygen (O_2) depletion (Pitorac, 2017). The aeration takes place by flushing in air close to the turbine runner, which is possible by central aeration through the shaft, distributed aeration using the turbine blades, or peripheral aeration from the inner wall of the draft tube (Rohland et al., 2010). For the first-mentioned types of turbine aeration, the hydrostatic pressure and a relatively small bubble size may lead to increased air dissolution in the water. Reports show that the levels of TDG supersaturation due to this method are comparably little, with values reaching up to 120 %TDG (Pulg et al., 2018).

It is worth noting that TDG supersaturation occurs naturally in rivers as well. This takes place when e.g. air is entrained into deep pools below waterfalls, where it dissolves due to the hydrostatic pressure. Increased photosynthesis taking place during algae blooming can cause TDG supersaturation as well (Pulg et al., 2018; Weitkamp and Katz, 1980). In the latter case, the increase in TDG saturation level stems from the production of O_2. As shown by Nebeker et al. (1979), N_2 is the air-content gas that is mainly responsible for mortality of fish due to the gas bubble disease (GBD), and that an increase in O_2 reduces the mortality[4]. Nevertheless, N_2 is not the single reason for GBD in fish, and supersaturation of water with O_2 can lead to fish mortality as well, even though the tolerance is higher in this case (Weitkamp and Katz, 1980). Ma et al. (2013) studied the relationship between TDG and DO, concluding that the DO level in a river should not be used as a proxy for the TDG saturation level as their correlation was found to be poor. Ma et al. (2013) studied the relationship between the level of TDG and the level of DO in water, discovering a poor correlation between them due to different water qualities in natural conditions. They therefore come to the same conclusion and recommend that the DO concentration level should not be used as a proxy for the concentration level of TDG.

Ecological consequences

Hydropower plants releasing TDG supersaturated water into the waterways downstream threaten the aquatic ecology using these waterways as their natural habitat. Fish and aquatic invertebrates are mainly affected by the GBD, which is defined as gas bubbles forming up within the organism. Those bubbles may appear within the tissue, for fish especially within the fins and the head. Furthermore, gas bubbles can form up in the blood vessels and organs, being responsible for

[4]The GBD is explained in Section 2.1.4.

lethality due to gas embolism. Secondary effects of the GBD are increased stress, open wounds, or secondary infections. In addition, the gas bubbles can increase the buoyancy of aquatic invertebrates, thus increasing the danger of being caught by predators or being carried away from the habitat by the water current (Pulg et al., 2018). The intensity and lethality of the GBD are dependent on the exposure time, the local water depth, the stage of life of the exposed organism, and the TDG saturation level within the water. Studies show different thresholds for that level, with a general consensus on an upper threshold range of 110 %TDG to 115 %TDG (Geist et al., 2013; Pulg et al., 2018; Weitkamp and Katz, 1980). The range stems from the fact that different species are affected in different ways by increased TDG saturation levels.

The GBD is related to the divers' disease (also known as compression sickness). These two sicknesses are both potentially lethal due to gas embolism as a result of TDG supersaturation of the blood. The divers' sickness is experienced by divers increasing the amount of dissolved gases in the blood due to the hydrostatic pressure in deep water, which leads to possible gas embolism during a too fast rise to the water surface. Its process can therefore be described as an internal TDG supersaturation, which is overcome by readjusting the TDG saturation level in the blood by taking breaks on the way up. The GBD on the other hand affects the organism from the outside. Fish breathe through their gills, where osmosis takes place. The partial pressure of the dissolved gases within the water and the blood will create a pressure difference that drives the gas exchange. In a regular case, the gas exchange will take place due to the surplus of Carbon dioxide (CO_2) and O_2 depletion of the blood. If the TDG saturation level in the water is increased, the osmosis will lead to an increased influx of dissolved gases into the blood.

A natural method to decrease the danger of GBD is to increase the hydrostatic pressure, as can be achieved by e.g. diving into deeper water. For each 1 m water depth, 9.7 %TDG are compensated (Pleizier et al., 2019). This depth is termed compensation depth and is defined as the water depth at which the hydrostatic pressure is equal to or greater than the pressure introduced by the TDGs in solution. While being above the compensation depth, bubbles nucleating in the liquid are growing due to natural gas diffusion. Being below the compensation depth will lead to the collapse of these bubbles due to the hydrostatic pressure. A representation of the compensation depth is displayed in Figure 2.4.

The actual avoidance behaviour of fish depends on the species. Experimental evidence is only available for a limited amount of species. A recent study by Lennox et al. (2022) showed that even though observed in laboratory experiments, brown trout does not show a self-regulating behaviour by moving into deeper regions of a natural river. Similar results are found by Lund and Heggberget (1985) and Pleizier et al. (2021b). On the contrary, Huang et al. (2010) found a strong avoidance beha-

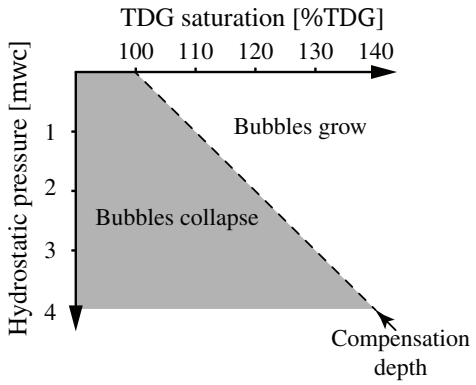

Figure 2.4: Representation of the compensation depth in dependence of the TDG saturation level and the hydrostatic head (reproduced from Pleizier et al. (2021a)).

viour in juvenile rock carp. Similar differences between fish species are reported in a review by Weitkamp and Katz (1980). As a result, existing possibilities to avoid TDG supersaturation in water bodies with larger water depths cannot be generalized into the allowance of higher TDG saturation levels in these waterways.

The GBD was first documented during the emergence of public aquaria (Gorham, 1899). A similarity to the decompression sickness discovered in deep-sea fishes being drawn to the water surface quickly led to the conclusion of pressure reduction being the reason for the disease. Only after further investigation, the cause was found to be the pressure-dependent saturation level of TDG, and a thorough description of the disease itself and its effect on different fish species was provided by Marsh (1908) and Marsh and Gorham (1905). Following this, numerous studies were conducted on the effects of GBD on further fish species, fish eggs, larvae, fry, and invertebrates (Weitkamp and Katz, 1980). Most of the research is limited to North American fish species, and only in recent years a number of studies on European and Asian freshwater fish species were presented (see Table 15 in Pulg et al. (2018)).

Official guidelines and threshold values

Having an overall agreement on the threshold of the TDG saturation level marking the values from which on the danger of the GBD appearing in fish is increasing, authorities of countries utilizing hydropower can intervene and provide limitations to the amount of TDGs in rivers downstream the power plant. Nevertheless, only the two countries have introduced such a threshold to limit TDG supersaturation. The USA defined the upper threshold as 110 %TDG (USEPA, 1976). In the *Canadian Water Quality Guidelines for the Protection of Aquatic Life*, the threshold for TDG supersaturation is defined with regard to the local depth of the water body. In areas

where it exceeds 1 m, the TDG saturation level should not exceed 110 %TDG, while the threshold for shallower water bodies is set to 103 %TDG (CCME, 1999). Both countries allow their individual states or provinces to impose individual guidelines, leading to regional deviations.

More commonly found are threshold values for DO, even though these usually describe only a lower threshold, e.g. needed for survival of fish. In Germany, the water quality class I is reached with DO concentrations above 8 mg dm^{-3}, while the lower quality classes III and IV are reached with values below 2 mg dm^{-3} (Adam, 2003). The immission guideline in Austria requires the DO concentration in running waters to be above 6.5 mg dm^{-3} (Pichler, 1996). The minimum criterion for DO in the USA is defined as 90 % of the natural concentration, even though the actual coldwater minimum is put to 4 mg dm^{-3} (USEPA, 1986). Only in South Africa exists an upper threshold. There, a target for the water quality with regard to DO ranges in between 80 % to 120 % concentration (Department of Water Affairs and Forestry, 1996).

The Research Council of Norway (NFR) funded the project *Hydropower induced supersaturation in freshwaters: effects on ecosystems, mitigation and solutions* (SUPERSAT, NFR#294742). It was led by Norwegian Research Centre (NORCE) and cooperated with international partners from Germany, Austria, and the USA. Within the project, hydropower plants are investigated with regard to their risk of generating TDG supersaturation by constructing a risk matrix. It shows that especially large Norwegian hydropower plants are at great risk of introducing TDG supersaturation into the waterways downstream the power plant (Pulg, 2021). The results of the risk analysis are displayed in Table 2.3. In cooperation with several hydropower plant owners, a measurement campaign to verify the risk matrix is planned. In addition, the SUPERSAT project aimed to raise the knowledge about biological effects of TDG supersaturation on certain European aquatic species. The final outcome of the project is intended to build a basis for establishing TDG saturation thresholds in regulated waterways in Norway and other European countries (Pulg et al., 2020).

Table 2.3: Results of the risk analysis by NORCE, showing the number of Norwegian hydropower plants per risk class (1 - low risk, 9 - high risk) and the respective sum of installed capacity.

Risk class	Number	Installed capacity [GW]
1	645	8.3
2	160	1.7
3	64	0.9
4	23	1.0
5	14	1.5
6	240	3.8
7	84	1.6
8	44	3.1
9	66	10.5

2.2 Physio-chemical considerations

The basis for the generation of TDG supersaturation and its removal from water are lying within chemical and physical fundamentals. This section describes the process of gas solubility and dissolution, as well as the drive of systems to reach an equilibrium. An overview of liquid-gas mass transfer is provided and an estimation of required values for resolving TDG supersaturation in hydropower plants is presented.

2.2.1 Gas dissolution in liquids

The topic of TDG supersaturation requires an introduction to the process of gas dissolution in liquids, which includes the physical principles of mass transfer and solubility. Those then define the gas concentration in the liquid and provide an understanding of the concepts of gas dissolution in liquids as well as the in this project desired degasification from the liquid volume. Degasification is here defined as the liberation of dissolved gases from a liquid medium, which takes place when gas bubbles grow to a sufficient size to leave the liquid entirely due to their buoyancy (Leong et al., 2011).

Liquid-gas mass transfer

Each liquid has a specific capacity to retain dissolved gases, depending on ambient and thermodynamic conditions. The basics for this are found in Henry's discovery of the solubility of gases in water in dependence of the pressure (Henry, 1803). Through thorough small-scale experiments, he found out that under equal circumstances of temperature, water takes up the same volume of condensed gas as

of gas under ordinary pressure, i.e. water takes up an amount of dissolved gas that is proportional to the gas' partial pressure in the gas phase. Within this section, a focus is put on the four main content gases of dry air, namely Nitrogen (N_2), Oxygen (O_2), Argon (Ar), and Carbon dioxide (CO_2), which together make up 99.9972 % of air. Other air-content gases such as Neon (NE), Helium (HE), or Methane (CH_4) are neglected due to their small partial pressure.

In mathematical form, the molar concentration, c, of a gas within an aqueous phase is calculated from the partial pressure of the gas, p_G, multiplied by Henry's law constant, K_H (i.e. a proportionality factor):

$$c = K_\mathrm{H}\, p_G. \tag{2.3}$$

Following Warneck and Williams (2012), Henry's law constant is calculated for the temperature range of 0 °C to 35 °C by using thermodynamic considerations[5]:

$$\ln K_\mathrm{H} = -\mathrm{A} + \frac{\mathrm{B}}{T} + \mathrm{C} \ln T. \tag{2.4}$$

A, B, and C are empirically determined coefficients related to the entropy and heat of a solution as well as the capacity difference of the substances between gaseous and liquid phases (Warneck and Williams, 2012). The calculation of the concentration of the air-content gases in an aqueous phase requires the partial pressure of the respective gas i in air. To arrive at the mass concentration, C, the molar mass of the gas, M, and the ambient pressure, p, have to be taken into account as well:

$$C_i = K_{\mathrm{H},i}\; p\; p_{G,i}\; M_i. \tag{2.5}$$

Using the values listed in Table 2.4, the mass concentration of the air-content gases is calculated using Equation 2.5. As visible from this equation and Equation 2.4, the mass concentration is dependent on the temperature and the pressure. With increasing temperature, the concentration decreases, while the pressure dependence is direct. In Figure 2.5, the mass concentration is plotted over the temperature and in dependence of the pressure. The temperature range is the one used for the calculation of Henry's law constant.

In Figure 2.6, the individual mass concentrations of the four main air-content gases in water are displayed for an atmospheric pressure of 1 atm. The calculated share of concentration values for a pressure of $p = 1$ atm and a temperature of $T = 10$ °C are displayed in Table 2.5. A direct comparison between the partial

[5] As CO_2 reacts with water to form ions (thus involving a dissolution equilibrium), it also depends on the pH of the solution (Warneck and Williams, 2012). This is neglected in the rest of the Thesis.

Table 2.4: Values used for the calculation of gas concentration in water (Warneck and Williams, 2012).

	N_2	O_2	Ar	CO_2
$p_{G,\%}$	78.08 %	20.95 %	0.93 %	0.03 %
M [g mol^{-1}]	28.01	32.00	39.95	44.10
A	177.57	175.33	146.40	11.55
B	8632.10	8747.50	7476.30	2440.00
C	24.80	24.45	20.14	0.00

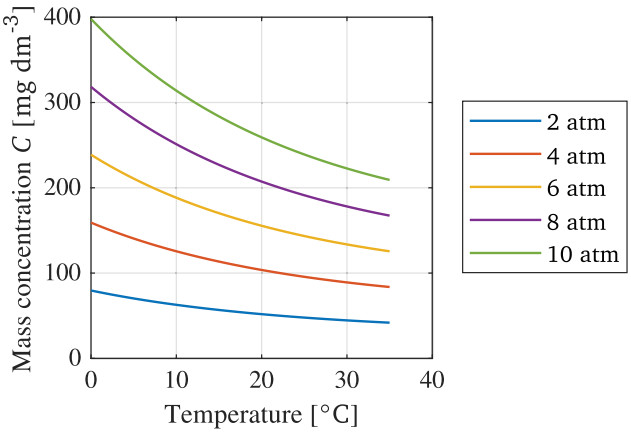

Figure 2.5: Mass concentration, C, of the TDGs in water over temperature for multiple pressures, p.

pressure of the air-content gases and their respective share in concentration shows that N_2 has a lower concentration share in water than its partial pressure would suggest, while the other air-content gases have a higher share in concentration. One reason for this is the mole fraction solubility, $\mathcal{X}$, which is twice as high for O_2 than N_2, and even higher for the other two gases. Battino and Seybold (2011) discussed the differences between the O_2 and N_2 solubility. They identified the effective volumes of the gases in water and the influence of these volumes on solution cavity formation terms to be the plausible cause.

As discussed earlier, the concentration of gases in water is dependent on the ambient pressure and the temperature. For each combination of the two parameters, the theoretical concentration of the air-content gases is given by Equation 2.5. The state in which all the driving forces are balanced is called equilibrium. The gas solubility then refers to the quantity of dissolved gas within the liquid at equilibrium conditions. Also, no net mass transfer occurs at equilibrium (Fair and Kister, 2003).

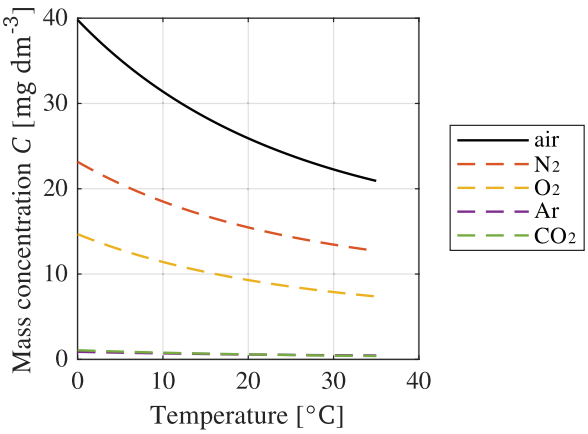

Figure 2.6: Mass concentration, C, of air-content gases and air in water over temperature for $p = 1$ atm.

Table 2.5: Partial pressure share, $p_{G,\%}$, concentration share, $C_{\%}$, (at $T = 10\,°C$) and mole fraction solubility, $\mathcal{X}$, (at $T = 25\,°C$, (Scharlin et al., 1998)) of air-content gases in water at $p = 1$ atm.

	N_2	O_2	Ar	CO_2
$p_{G,\%}$	78.08 %	20.95 %	0.93 %	0.03 %
$C_{\%}$	58.92 %	36.31 %	2.21 %	2.48 %
$\mathcal{X}$	$1.18 \cdot 10^{-5}$	$2.30 \cdot 10^{-5}$	$2.53 \cdot 10^{-5}$	$61.48 \cdot 10^{-5}$

An equilibrium at the interface between a gas and a liquid is simplified in Figure 2.7. Displayed are the partial transfer conductances on the side of the gas phase and the liquid phase, k_G and k_L, respectively. The difference between the concentration at the interface is a graphical representation of Henry's law constant.

Following the film theory, the interface is stable and separates the two phases. Mass is transferred instantaneously to ensure that the interface always stays at equilibrium. On both sides of the interface, there is a film with thickness δ_i, in which the fluid motion is slow. Therefore, in case of a deviation from the equilibrium, only diffusion contributes to mass transport in this region, thus leading to concentration gradients. At a certain distance from the interface, the fluid motion is assumed to be high, leading to rapid and equal distribution of mass. Thus, the concentration there is assumed to be constant (Fair and Kister, 2003).

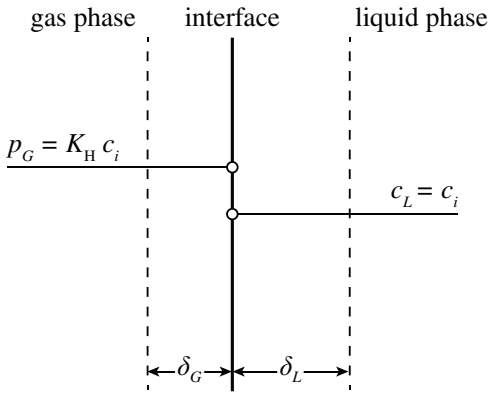

Figure 2.7: Equilibrium state at the interface between a gas and a liquid phase. δ_G and δ_L are the diffusion layer thicknesses in the gas and liquid phase, respectively, p_G is the partial gas pressure in the gas phase, K_H is Henry's law constant, c_i is the gas concentration at the interface, and c_L is the gas concentration in the liquid phase. Adapted from Hihn (1992).

In Figure 2.8, the interface between a gas and a liquid is displayed for the case of non-equilibrium. The film theory is apparent from the concentration gradients, which are apparent only in the liquid and the gas film, δ_L and δ_G, respectively. Again, the concentration difference at the interface stems from Henry's law constant.

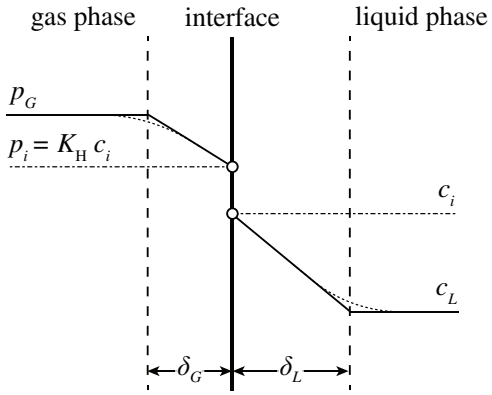

Figure 2.8: Deviation from equilibrium leading to mass transfer at the liquid-gas interface. δ_G and δ_L are the diffusion layer thicknesses in the gas and liquid phase, respectively, p_G is the partial gas pressure in the gas phase, p_i is the gas pressure at the interface, K_H is Henry's law constant, c_i is the gas concentration at the interface, and c_L is the gas concentration in the liquid phase. Adapted from Fair and Kister (2003) and Hihn (1992).

Governing equations

The mass flux across the liquid-gas interface is represented by the diffusion equations for each film, using a linear approximation of the concentration gradients[6]:

$$\varphi = k_G\,(y - y_i) = k_L\,(x - x_i)\,, \tag{2.6}$$

with the mass transfer coefficients in the gas and the liquid phase, k_G and k_L, respectively. The equation shows that the mass transfer is proportional to the concentration difference between the bulk and the liquid-gas interface. The resistance to mass transfer in the phases is expressed by the reciprocal of the respective mass transfer coefficient. Assuming a hypothetical bulk-gas y^* being in equilibrium with the concentration in the liquid phase, and mass transfer from the gas to the liquid, i.e. dissolution, Equation 2.6 is rewritten as:

$$\varphi = \frac{1}{\frac{1}{k_G} + \frac{1}{k_L}}\,(y - y^*)\,. \tag{2.7}$$

Here, the overall resistance to mass transfer equals the sum of the phase resistances. In case of the air-content gases in consideration, the resistance is known to be mostly present in the liquid phase. Neglecting the resistance in the gas phase, Equation 2.7 is simplified to:

$$\varphi = k_L\,(y - y^*)\,. \tag{2.8}$$

An illustration of this state is displayed in Figure 2.9. The concentration gradient in the gas film is missing as consequence of the missing resistance to mass transfer.

Instead of mole fractions, the mass flux can be expressed by the mass concentration and the partial gas pressure in the liquid and gas phases, respectively. With the bulk gas assumption introduced in Equation 2.7, the mole fraction of the bulk gas is substituted with the mass concentration of the bulk, C_{bulk}. The mole fraction in the gas phase is represented by the partial gas pressure, as the resistance in the gas phase is still neglected:

$$\varphi_i = k_{L,i}\left(\frac{p_{G,i}}{K_{\mathrm{H},i}} - C_{bulk,i}\right). \tag{2.9}$$

Using Henry's law, the partial pressure is substituted by the mass concentration at equilibrium, C^*. Additionally, the interfacial area between the phases is often difficult to determine, especially if there is no resistance to mass transfer in the gas phase (Alvarez et al., 2002). Therefore, it is easier to consider the volumetric mass

[6]The derivation of the equation for the liquid-gas mass transfer coefficient $k_L a$ in this section follows Fair and Kister (2003).

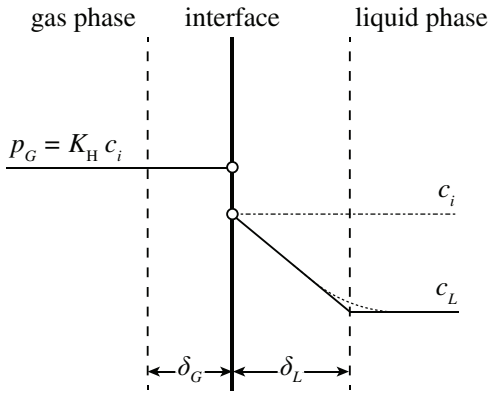

Figure 2.9: Mass transfer at a liquid-gas interface with neglected resistance in the gas phase. δ_G and δ_L are the diffusion layer thicknesses in the gas and liquid phase, respectively, p_G is the partial gas pressure in the gas phase, K_H is Henry's law constant, c_i is the gas concentration at the interface, and c_L is the gas concentration in the liquid phase. Adapted from Hihn (1992).

transfer coefficient, i.e. the product of partial transfer conductance and interfacial area. This leads to:

$$\varphi = k_L a\,(C^* - C_{bulk})\,, \tag{2.10}$$

where C^* denotes the equilibrium concentration in the gas phase. Assuming that the mass flux is introduced by a change in concentration, Equation 2.10 is written as:

$$\frac{\mathrm{d}C_L(t)}{\mathrm{d}t} = k_L a\,(C^* - C_{bulk}(t))\,, \tag{2.11}$$

where $C_L(t)$ is the concentration level in the liquid phase over time. In case of mass transfer taking place within a volume, Equation 2.10 changes to:

$$\Phi = k_L a\; V\,(C^* - C_{bulk})\,. \tag{2.12}$$

Throughout this Thesis, all data is recorded as saturation instead of concentration. This does not contradict the derived equations, since saturation and concentration are interchangeable, as they are directly proportional for all cases under consideration.

2.2.2 Estimation of mass transfer requirements

Using the equations derived in Section 2.2.1, an estimation for the required values of the volumetric liquid-gas mass transfer coefficient, $k_L a$, is made. The target for any degasification application used downstream a hydropower plant is to decrease the TDG saturation level in the water to 110 %TDG, as discussed in

Section 2.1.4. Assuming a hydropower plant with a discharge of $Q = 100\,\mathrm{m^3\,s^{-1}}$ and an outlet cross-section area of $A_{outlet} = 20\,\mathrm{m^2}$, the required $k_L a$ is calculated in dependence of the length over which a degasification application is active and the level of TDG supersaturation[7].

The resulting curves are presented in Figure 2.10. It is apparent that the higher the TDG saturation level, the higher the liquid-gas mass transfer coefficient needs to be. Additionally, the possibility to implement a degasification application in a way that it covers a larger distance will decrease the required $k_L a$. Three general considerations are resulting from this:

1. a higher degree of TDG supersaturation in the water exiting the hydropower plant increases the required $k_L a$,
2. the degasification application's covered length is inversely correlated to $k_L a$, and
3. the range of $k_L a$ is assumed to be in the range of $10 \cdot 10^{-3}\,\mathrm{s^{-1}}$ to $100 \cdot 10^{-3}\,\mathrm{s^{-1}}$.

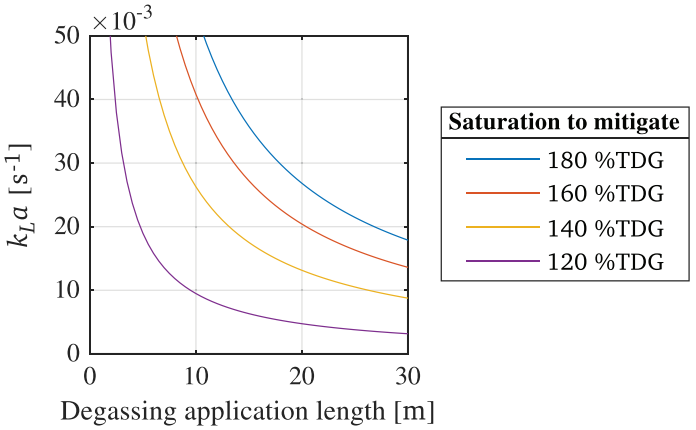

Figure 2.10: Estimation of the $k_L a$ needed to reduce the TDG saturation level at an arbitrary hydropower plant with $Q = 100\,\mathrm{m^3\,s^{-1}}$ and $A_{outlet} = 40\,\mathrm{m^2}$ from different TDG supersaturation levels to 110 %TDG.

In other words, the lower the initial TDG saturation level and the longer distances covered by a degasification application are, the easier will it be to lower the TDG saturation level to ecologically tolerable values. Mitigating a severe TDG supersaturation of e.g. 180 %TDG on a short distance, on the other hand, requires a liquid-gas mass transfer coefficient that is at the upper border compared to observed mass transfer rates reported by literature (see Section 3.3). It has to be noted that these calculations are of theoretical nature, and that each hydropower plant gener-

[7]The required steps for the calculation of $k_L a$ using the TDG saturation level are presented in Section 3.2.

ating TDG supersaturation will have individual requirements in dependence of its discharge, outlet area, tailrace turbulence, etc.

2.3 Technical considerations

In order to detect TDG supersaturation within water, measurement techniques were developed to quantify the amount of dissolved gases within a liquid. A short introduction to the sensors available is given within this section, followed by an overview of possibilities to enhance the degasification process by technical and physio-chemical means. The section concludes with methods used to date to prevent the generation of TDG supersaturation at or within hydropower plants, or mitigate its effects in the waterways downstream.

2.3.1 Measurement techniques

Different methods to determine the amount of gas being dissolved in liquids exist, as the approach is usually dependent on the gas species in solution. In general, the determination is possible by chemical methods or direct measurements using sensors. In the course of this project, gas measurements were taken only by use of sensors. Therefore, the chemical determination of dissolved gases is not further explained in this Thesis. Common sensors for dissolved gas determination make use of optical (Jiang and Ma, 2021) or membrane-based methods (D'Aoust, 2007; Pleizier et al., 2021a). In addition, membrane-inlet mass spectrography (Chatton et al., 2017; Kapit and Michel, 2021) or gas chromatography is used (Schelter et al., 2014; Swinnerton et al., 1962). Besides their capacity to detect a single or multiple gas species, these methods also differ in terms of their applicability in situ or ex situ, suitability for field or laboratory settings, measurement time, and economic aspects.

The measurement of the TDG saturation level is possible by multiple of the above-mentioned methods. Yet, the measurement is not trivial, as single-gas solutions are rare in nature, and therefore all or at least the major air-content gases have to be taken into account. A good representation for this is the total gas pressure (TGP), which is defined as the sum of all partial gas pressures of the gases in solution:

$$p_{\mathrm{TGP}} = \sum_i p_{G,i}. \tag{2.13}$$

Following this approach, the determination of the TGP is possible by measuring the concentration of multiple dissolved gases, followed by a determination of the partial gas pressure, e.g. by using Equation 2.5. For the scope of this project, measurements are required to take place in situ with the fastest possible response time. The choice is therefore made to consider only optical or membrane-based gas sensors. While it is possible to directly measure the concentration of single

air-content gases such as O_2, CO_2, or Ar, the lack of sensors for direct and real-time measurements of N_2 poses a challenge. As a result, utilizing multiple single-gas sensors for the determination of the TGP and thereby the TDG saturation level becomes unattainable, as Equation 2.13 cannot be applied. This is why the primary method in use for direct TDG measurements is membrane-based sensors called Weiss saturometer (Fickeisen et al., 1975).

In general, the Weiss saturometer is utilizing a pressure sensor to record the dissolved gas pressure of all gas species in solution. The most common type consists of a sealed silastic tubing serving as a membrane, which is coiled onto a cartridge. The silastic tube is semipermeable, allowing only for the diffusion of dissolved gases and water vapor. A sealed housing fits the onboard electronics and the pressure sensor, and both the cartridge and the silastic tubing are attached to it. Another type consists of a flat, semipermeable membrane that is placed in front of a hollow chamber within the housing. Depending on the TDG saturation level in the solution, dissolved gases will diffuse through the semipermeable membrane by osmosis, thus changing the pressure within the tubing or chamber. The reading of the attached pressure sensor then represents a direct measurement of the TGP. A common approach to report the TDG saturation level of the solution is to relate the TGP to the atmospheric pressure, which is simultaneously measured ex situ:

$$S_{\mathrm{TDG}} = \frac{p_{\mathrm{TGP}}}{p_{\mathrm{atm}}} \cdot 100. \tag{2.14}$$

An advantage of using this approach is the independence on S_{TDG} on the water depth, as the result is not calculated as a relation of saturation, which would change in dependence of the hydrostatic pressure, but as a relation of pressures. On the other hand, a dependency on the altitude at which the atmospheric pressure is determined exists, as discussed by Pleizier et al. (2021a) They therefore recommend to either report the atmospheric pressure together with the TDG saturation level, or to introduce the difference between TGP and atmospheric pressure:

$$\Delta p_{\mathrm{TDG}} = p_{\mathrm{TGP}} - p_{\mathrm{atm}}. \tag{2.15}$$

This difference is a representation of the main driving force of gas diffusion (Pleizier et al., 2021a). Substituting Equation 2.15 into Equation 2.14 leads to

$$S_{\mathrm{TDG}} = \frac{\Delta p_{\mathrm{TDG}} + p_{\mathrm{atm}}}{p_{\mathrm{atm}}} \cdot 100. \tag{2.16}$$

In any case, the measurement of the TDG saturation level requires the simultaneous measurement of both TGP and atmospheric pressure.

Following the definition of the TDG saturation level (Equation 2.14), a liquid-gas system at equilibrium would correspond to 100 %TDG. This shows a disadvantage of the Weiss saturometer. As it only reacts to the TGP within the system, an

imbalance between the gas species in solution where e.g. one species is elevated and others are diminished, can theoretically result in a reading of 100 %TDG.

Another disadvantage are rather long response times of the Weiss saturometer. Due to the semipermeable nature of the silastic tubing, the time to equilibrium between the pressure inside the tube and the TGP is dependent on the speed of osmosis and thus on the temperature. A common estimate from manufacturers for the time to saturation within the sensor is around 5 min, depending on the TDG saturation level within the solution and the temperature (D'Aoust, 2007). In contrast to this, saturation times of up to 15 min to 30 min have been reported by literature (Pleizier et al., 2021a).

Finally, the measurement of the TDG saturation level using Weiss saturometers has to be carried out with regard to the compensation depths related to TDG supersaturated liquids[8]. When measurements are taken above the compensation depths, air bubbles can nucleate on the silical tubing of the sensor and falsify the sensor reading. This is overcome by either moving the sensor to deeper measurement areas or by introducing a flow velocity high enough to detach the forming bubbles (Pleizier et al., 2021a).

Even though the presented disadvantages of the Weiss saturometer make their application difficult, to date they present the only technique to determine the TDG saturation level in real-time and in situ. Due to the incapability of determining the different partial pressures of the gas species in solution, it is recommended to take parallel measurements using DO sensors. This will allow for an estimation of the share of the main air-content gases in solution found in nature, N_2 and O_2. Throughout the following chapters of this Thesis, a Weiss saturometer will be referred to as TDG sensor.

2.3.2 Enhancement of degasification

As shown in Section 2.2.1, the dissolved gas concentration of a liquid is directly proportional to the ambient pressure. A change within this pressure will therefore result in a drive towards equilibrium. Having a TDG supersaturation at atmospheric pressure thus leads to a natural degasification of the liquid. This process is dependent on several parameters, such as temperature or turbulence, but will in general be slow[9]. In addition, bubble nucleation will take place on surfaces within TDG supersaturated liquids due to gas cavities. This will lead to a slow increase in natural degasification, but is dependent on the local velocity and pressure (Jones et al., 1999).

Therefore, enhancement of degasification to increase its efficiency is often required, as different fields show the need to temporarily or permanently reduce or remove one or multiple dissolved gas species from a liquid phase. Several ways

[8] As introduced in Section 2.1.4.

[9] This will be further elaborated upon in Chapter 3.

to achieve efficient solution degasification were developed over time, with the first applications being described in the early 20th century. All methods require specific mechanisms to extract the dissolved elements or molecules from the liquid body. The purpose of removing dissolved gases depends on the type of industry utilizing the degasification application, and ranges from product quality improvement over product processing to the prevention of chemical reactions. The different mechanisms used to enhance the degasification process are described in detail within this section. A special focus is laid on ultrasonic degasification as a possible tool for the prevention of TDG supersaturation in the river downstream a hydropower plant.

Chemical degasification

Dissolving certain chemicals in a solution leads to the degasification of dissolved gas species due to chemical reactions. These chemicals are often referred to as gas scavengers or reductants. This method was used to prevent oxidation within water supply pipes by corroding filler material in tanks, thus removing the DO from the water (McDermet, 1924). Today, specialized products are available to target certain dissolved gas species in water management (TETRA Technologies Inc., 2023). Other examples for applications of chemical degasification are found in metallurgy (Campbell, 2015) or natural gas processing (Poe and Mokhatab, 2017). Apart from chemicals, the use of certain additives within the system also promotes the degasification process, by e.g. boundary mixing effects or inhibition of bubble coalescence (Ho et al., 2020).

Increased surface contact or specific interface

A group of methods to enhance degasification relies on increasing the surface contact of dissolved gases, i.e. the interfacial area a in the liquid-gas mass transfer coefficient. This is usually done by increasing the surface area of the liquid. In the following, the methods of aeration, spraying, and membranes are explained.

Aeration The wording "aeration" is used for two different methods of degasification. In the first interpretation, it describes the increase in the liquid surface area. This was described in simple experiments by Marsh and Gorham (1905), who investigated the degasification from TDG supersaturated water by studying the free fall from an elevated position and the subsequent splashing on the water surface. During the splashing, the liquid body breaks up into drops, thus increasing its surface area. As a result, aeration removes excess gas from the liquid body[10]. In addition, this method was shown to increase undersaturation. In follow-up experiments, Marsh (1908) used sets of rectangular pans with a specific number of holes to reduce the amount of N_2 and CO_2 and increase the O_2 content in water. Similar

[10]This type of aeration is the reason why TDG supersaturation rarely occurs in hydropower plants with Pelton turbines.

devices are still in use today, going under terms such as gravity aerator (Davenport et al., 2001; Roy et al., 2022).

The second interpretation of aeration is the introduction of gas bubbles to the liquid body, also known as gas stripping or inert gas flushing. Due to buoyancy, the bubbles rise to the liquid-gas interface and disappear from the liquid (Crawford et al., 2017). In this case, the gas transfer is broken into the gas transfer at the liquid's surface and the gas transfer at the liquid-gas interfacial area. Due to the disequilibrium between the dissolved gases present in the liquid bulk and within the bubbles, dissolved gases migrate from the liquid into the rising bubbles. In addition, a mixing of the liquid due to the ascensional, i.e. large-scale recirculatory, motions contribute to the degasification (Zhang et al., 2017). Once the gas bubbles reach the liquid surface, they disappear from the system, which represents the degasification. A small amount of gas injected into the liquid is sufficient to achieve a rapid and effective decrease of dissolved gas, but the method is dependent on the number and size of the injected gas bubbles. Diffused aeration systems make use of porous diffusers to generate a bubble plume rising through the liquid bulk (Wilhelms and Martin, 1992). This method has been shown to decrease the TDG saturation level in water in dependence of water depth, gas flow rate, and bubble size and number (Ou et al., 2016).

A combination of the two aeration methods is a packed column, i.e. an inexpensive and reliable film-flow aerator (Colt, 1984). The liquid is flowing under gravity from the top of a tower to the bottom, passing a packing media and forming a film layer on the packing surfaces, thus increasing the liquid surface area. Simultaneously, gas is blown upwards the column, stripping dissolved gas from the counterflowing liquid (Singh, 2015). This technique is used in aquaculture and water treatment operations (Crawford et al., 2017)

In the field of metallurgy, aeration by inert gas flushing is the most common way of removing hydrogen from aluminum, magnesium, and copper alloy molts (Neff, 2008). The inert gas flux leads to a large difference in concentration between the dissolved hydrogen and the gas bubbles, thus increasing the degasification. An increased efficiency is achieved by decreasing the bubble size and dispersing them homogeneously in the molt due to mixing. A wide range of similar processes are used for secondary steelmaking ('Steel Melt Processing' 2008). In combination with chemical degasification methods such as chloride refining, the degasification efficiency further increases (Wang et al., 2009).

Spraying Using nozzles to split a liquid bulk into small droplets is referred to as spray degasification. The increase in the liquid surface area leads to the degasification of dissolved gas species. This technique is used e.g. as an alternative method for hydrogen removal from molten aluminum, where it is combined with an ambient inert gas into which the molten metal is sprayed. Thus, both increased

liquid surface area and increased concentration difference lead to more efficiency during the degasification process. Compared to the other degasification methods within metallurgy, advantages in form of better kinetic conditions, avoidance of hydrogen absorption, and inert gas recycling are shown (Wu et al., 2005).

Membranes The use of special membranes to increase the degasification of liquids is built upon the increase in surface area and large concentration differences as well. They are therefore similar to the aforementioned packed columns, and are mainly used for the degasification of O_2 and CO_2 (SnowPure Water Technologies, 2023). In general, a liquid flows into a membrane contactor, where it is split into several cylindrical chambers, thus increasing the liquid surface area. These are separated by hydrophobic, hollow-fiber membranes. Within these membranes, a countercurrent flow of inert gas or liquid, or a vacuum is present. This leads to the diffusion of dissolved gas species through the membrane into the countercurrent flow or vacuum due to the concentration difference (HydroGroup, 2018). Degasification membranes are mostly utilized within water treatment (Bandara et al., 2013; Singh, 2015) or for the degasification of non-aqueous solutions (Rzechowicz and Pashley, 2006).

Modifying thermodynamic conditions

By modifying the thermodynamic conditions of a system, degasification of a liquid is possible. This is achieved by altering the temperature, pressure, or turbulence of the system. These factors are often combined to increase the efficiency, as will be presented in the following.

Temperature With an increase in the temperature of a system, the insolubility of dissolved gases will increase (as explained earlier in Section 2.2.1, see also Figures 2.5 and 2.6). Therefore, the dissolved gas species will be driven out of the system. This effect increases with increasing concentration values (Shen et al., 2014). Once the liquid is heated to the boiling point, dissolved gases will be taken up by bubbles during their rise to the liquid surface. As bringing large volumes to boiling is very energy extensive and usually comes along with undesired side effects, this method is usually combined with other degasification methods to enhance their efficiency.

Pressure Following Henry's law, a reduction of the ambient pressure of a system will lead to a difference in the concentration at an interface of the liquid with an atmosphere. The resulting drive to equilibrium forces dissolved gas species out of solution. Early industrial-scale deaerators for protection of e.g., pipelines and boilers from corrosion were based on this method, injecting heated water into a region of vacuum (Elliot Company, 1923; McDermet, 1924). There, violent and explosive boiling occurs, liberating dissolved gases from the water. The principle of those deaerators is still in use to date, e.g., in industrial steam systems, with the same intent of protecting the systems from the effects of corrosive gases (USDOE,

2012). A similar method is used to remove dissolved gas species from coolant water of nuclear reactors (Battaglia and Fleming, 1987; Gramer and Korn, 1974; Jie et al., 2013; Yamamoto et al., 2019). The liquid is pressurized, heated, and partially vaporized, thus having an increase in the liquid surface area in addition. With a reduction of the treated volume and a reduction of the ambient pressure, the process becomes more efficient (Zhong et al., 2018).

Freeze-pump-thaw cycling The degasification using freeze-pump-thaw cycling is deployed to remove dissolved gases from small, liquid volumes. During the process, the liquid is frozen quickly by e.g. using liquid N_2. Then, pumping is applied on the sample at this temperature to create a vacuum. After isolating the headspace of the apparatus, the sample is allowed to thaw. During the thawing, any noncondensable gases will boil out of the material and move into the headspace where they are pumped away. This cycle is repeated several times to improve the degasification result (Shriver and Drezdzon, 1986).

Turbulence As described earlier, degasification of TDG supersaturated liquids will naturally take place on the liquid's surface to the atmosphere due to the drive to equilibrium. In a static liquid, this drive will decrease due to the development of concentration gradients within the liquid body. The introduction of turbulence within the liquid increases mixing, thus replenishing the liquid's surface concentration. Moreover, the interfacial area provided by the liquid's surface is increased by turbulence, consequently increasing the mass transfer as well. The simultaneous introduction of bubbles and turbulence for the degasification of a liquid enhances the process by preventing bubble coalescence and providing a more homogeneous bubble distribution (Maluta et al., 2023; Žák et al., 2023). Increased turbulence also increases the degasification of TDG supersaturated water, which has been both shown in laboratory experiments (Shen et al., 2014) and natural rivers (Pulg et al., 2016; Pulg et al., 2018). In addition, the turbulent kinetic energy at the liquid surface can be increased by external factors, such as wind. This will lead to a similar enhancement of the degasification process (Huang et al., 2016).

Mechanophysical techniques

The use of certain mechanical or physical techniques enhances the degasification within liquids. As with the degasification methods described earlier, these techniques are applied within several different fields. Especially ultrasonic degasification has a wide range of application, while centrifugal degasification is a rather seldom-used technique.

Centrifugal Centrifugal forces are used to decrease the TDG saturation value of a liquid. During the centrifugation of a liquid, gas nuclei as well as gas bubbles will be removed from it by increased buoyancy (Harvey et al., 1945). This method is applicable for removing macronuclei, which take up dissolved gas species and

transport them out of the liquid bulk, while micronuclei are resistant to the treatment. In addition, a pressure decrease within the centrifuge will lead to an increase in the diameter of gas bubbles within the liquid, thus leading to an increase in the interfacial area. Centrifugal degasification is used for high-viscous fluids, e.g. in metallurgy or polymer science (Kiljański and Dziubiński, 2001), or during natural oil and gas extraction ('Chapter 11 - Equipment and Equipment Integration' 2012).

Ultrasound If an acoustic field is applied to a liquid volume, a time-varying, generally sinusoidal, pressure (i.e. acoustic pressure waves) is superimposed on the ambient pressure (Leong et al., 2011; Neppiras, 1980). Acoustic pressure waves with a frequency above 18 kHz to 20 kHz, i.e. higher than the audible range of humans, are referred to as ultrasound (Ellens and Hynynen, 2015; Gallego-Juárez and Graff, 2015; Nomura and Koda, 2015). The ultrasonic frequency range is divided into two different areas based on the applications: high-frequency low-intensity ultrasound and low-frequency high-intensity ultrasound. The former is referred to as diagnostic ultrasound and covers the range of 1 MHz to 10 MHz, using power within the milliwatt region. The latter is operating in the range of 20 kHz to 1 MHz and can be operated with powers ranging in the kilowatt region. Therefore, it is known as power ultrasound (Gallego-Juárez and Graff, 2015; Mason, 1999; Pollet and Ashokkumar, 2019). With regard to the acoustic intensity, the field of power ultrasound is divided into high intensity (10 $\mathrm{W\,cm^{-2}}$ to 1000 $\mathrm{W\,cm^{-2}}$) and low intensity ($< 1\,\mathrm{W\,cm^{-2}}$) ultrasonication (Theerthagiri et al., 2020).

Already one century ago, the formation of bubbles within an acoustic field due to the exceedance of the ambient pressure was discovered (Boyle, 1922). This bubble formation was later attributed to cavitation within the antinodes of the standing sound wave, where a pressure below the atmospheric pressure causes the gas dissolution, and that the expulsed gas bubbles do not re-dissolve during their rise through the liquid (Richards and Loomis, 1927). The origin of these gas bubbles was identified as small cavities within the liquid. Due to the radiation pressure, they are transported to the pressure nodes where they accumulate (Goldman and Ringo, 1949; Lindström, 1955). Early studies showed that

- the energy needed for the degasification increases with the frequency (Sörensen, 1936),
- the concentration is halved practically independent of the intensity,
- the rate of degasification is proportional to the degree of supersaturation, and
- there is a linear relationship between the sonication time and the amount of hydrogen peroxide formed during ultrasonic cavitation (Lindström, 1955).

Several books (or book chapters) give detailed overviews of the dynamics involved with single or multiple bubbles within the ultrasonic fields, e.g. Lauterborn and Mettin (2015), Mettin and Cairós (2016) and Yasui (2018). The bubbles are formed in three different ways (Mettin and Cairós, 2016):

1. spontaneous single-bubble creation at a nucleus apparent in the liquid,
2. continuous bubble appearance from specific sources in the liquid or at walls, and
3. fragmentation of already existing bubbles.

The appearance of nuclei within the liquid is here based on the phenomenon of acoustic cavitation. The threshold describing the tension needed to form an observable cavity in the liquid is referred to as the cavitation threshold and depends on cavitation nuclei and parameters such as the frequency of sound field, the static pressure, the temperature of the liquid, or the liquid itself (Yasui, 2011). Bubble fragmentation comes into effect due to bubble deformation and splitting, which is to be expected in any application of acoustic cavitation (Lauterborn and Mettin, 2015).

After nucleation, different mechanisms lead to bubble growth. The classic approach is that below a physical limit, called Blake threshold, gas bubbles and nuclei dissolve in the liquid due to the liquid's ambient pressure. The threshold describes the acoustic pressure from which on a bubble will grow under the influence of an acoustic field in dependence of the bubble radius (Yasui, 2015). Above this threshold, bubble growth takes place due to coalescence, i.e. the combination of two or more bubbles to a larger bubble, or rectified mass diffusion, a term describing the growth of individual bubbles over several acoustic cycles (Crum, 1984). More recent research points out that this theory is based on linear models, while non-linear theory states that micro-bubbles cannot grow due to rectified diffusion. Therefore, a threshold for the rectified diffusion pressure is introduced, which, at high acoustic pressures, merges with the Blake threshold (Louisnard and Gomez, 2003). Following the non-linear theory, the bubble growth is divided into three steps (Louisnard, 2017):

1. bubble nuclei grow by mechanisms like coalescence or accumulation at the acoustic field's antinodes until they reach the Blake or rectified diffusion threshold[11],
2. once above the threshold, bubbles start oscillating inertially and grow due to rectified diffusion, and
3. bubbles hit the fragmentation threshold, where they break up and multiplicate.

The first step here is decisive, as a dynamical competition between nuclei dissolution and coalescence exists. While dissolution leads to the destruction of the bubble

[11]This is speculative and remains yet to be proven (Louisnard, 2023).

population, coalescence leads to restoration of the bubble sizes above the Blake or rectified diffusion threshold (Louisnard, 2017).

Growth by rectified diffusion takes place due to an uneven mass transfer introduced by area and shell effects. Area effects describe the mass transfer occurring due to the bubble motion. During the compression phase of the bubble, the gas concentration inside increases, and the gas diffuses into the liquid. Due to a larger bubble surface during expansion, the diffusion rate is higher in the rarefaction stage of the oscillation, resulting in a gradual filling of the bubble with dissolved gas from the liquid. Shell effects refer to the thickness of the liquid-gas interface: during the compression phase, the shell thickens, while the shell thins during bubble expansion. This leads again to a lower concentration gradient for the compressed bubble, thus creating a lower driving force for the mass transfer (Eller and Flynn, 1965). Additionally, microscopic acoustic streams generated in the viscous boundary layer around the bubble take part in mass transfer by bringing fresh liquid phase to the bubble surface (Eskin, 2015). A schematic overview of the rectified diffusion process using an idealized spherical bubble is displayed in Figure 2.11.

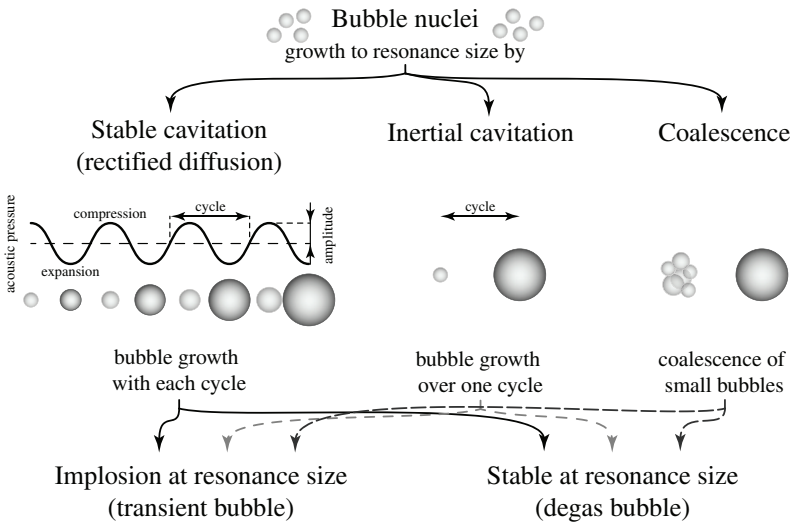

Figure 2.11: Schematic of the bubble growth mechanisms for idealized, spherical bubbles within an acoustic field.

Bubbles at resonance size become either transient, meaning that the bubble becomes unstable and collapses, or stable, where the bubble oscillates for many cycles at the linear resonance size (Leighton, 1994; Leong et al., 2011; Ye et al., 2019). During the transient bubble collapse, a microscopic implosion generates high local turbulence and releases heat energy. The local temperature and pressure increase is estimated to be in the range of up to 5000 K and 150 MPa, depending

on various conditions of the oscillating bubble (Pollet and Ashokkumar, 2019). Kuttruff's hot spot theory states that a sufficiently fast bubble collapse results in its contents being compressed so strongly that the adiabatic temperature rise leads to high enough temperatures for light emission (Kuttruff, 1962), an effect called sonoluminescence. An additional attribute of the bubble collapse is the disturbance of the pressure due to the shockwave, generating mechanical effects such as mixing and shearing (Leong et al., 2011). Moreover, energy is carried away from the bubble. Thus, the shockwave introduces dampening effects (Lauterborn and Mettin, 2015). Due to the high pressure and temperature during the transient bubble collapse, a thermal dissociation of water vapor takes place, resulting in radical formation inside the gas bubble (Merouani et al., 2015).

The effects of transient bubble collapses within a liquid are used within the field of sonochemistry. Sonochemical applications in liquids are used to permanently change the physical, chemical, or biological properties of materials applied to. Beneficial for these changes are also wave distortion, acoustic saturation, radiation pressure, and acoustic streaming (Gallego-Juárez and Graff, 2015). Multiple areas make use of sonochemical effects, e.g. electrochemistry (Hihn et al., 2018; Nevers et al., 2018; Theerthagiri et al., 2020; Touyeras et al., 2005), food industry (Chen et al., 2020; Yu et al., 2022; Yuan et al., 2021), waste water treatment industry (Bampouli et al., 2023; Bhat and Gogate, 2020; Mahamuni and Adewuyi, 2010) or metallurgy (Komarov et al., 2005; Santos et al., 2013).

Shape-stable bubbles at resonance size contribute to the degasification process by moving to the liquid surface due to the radiation force. They are therefore called degas bubbles (Yasui, 2002). This process is referred to as ultrasonic degasification and consists of three steps (Kapustina, 1973):

1. the growth of small air bubbles present in the liquid due to an ultrasonically accelerated mass transfer of dissolved gas into the bubbles, i.e. rectified diffusion,
2. coalescence of two or more bubbles caused by the action of acoustic streaming, acoustic radiation pressure and Bjerknes and Bernoulli forces, and
3. the rise of growing bubbles to the surface due to greater buoyancy and escape from the liquid.

The role of cavitation is described as an acceleration of the degasification process due to the multiplication of bubbles and more active diffusion of the dissolved gas into small bubbles oscillating in a nonlinear manner. The presence of ultrasound increases the mass transfer coefficient. This is directly related to the ultrasonic power, due to an increase in the number of cavitation bubbles within the liquid caused by higher cavitational activity, and higher rates of liquid circulation (Gondrexon et al., 1997; Kumar et al., 2004; Yasui et al., 2008).

The liquid circulation takes place due to the effect of acoustic streaming, which is generally described as a steady flow created by the acoustic waves passing through the liquid (Lighthill, 1978; Nyborg, 1953; Trujillo and Knoerzer, 2011), as well as due to the emergence and subsequent movement of gas bubbles (Mandroyan et al., 2009b). It is directly linked to the distribution of the acoustic energy within a reactor, which in turn influences the cavitation activity. This activity is, in case of no-flow conditions, uniformly distributed in the transducer's direction of radiation, with a maximum close to the transducer surface (Viennet et al., 2004). Above a transducer with a flat, circular surface, a conical bubble structure develops in direction of the wave propagation axis. The structure is connected to the cavitational run-off, and growths in height with the transducer power (Mandroyan et al., 2009b). The corresponding velocity field of such a setup has a helical shape, with velocities being directly proportional to the acoustic power. The acoustic streaming depends largely on the ultrasonic transducer's shape, power, and frequency, as well as on the boundary conditions for the wave propagation within the system, and is highest at lower ultrasonic frequencies (Mandroyan et al., 2009a). The energy dissipated by acoustic cavitation into the liquids corresponds to at least 90 % of the fluid convection (Hihn et al., 2011).

An increase in the sonicated volume will lead to a decrease in the mass transfer coefficient (Gondrexon et al., 1997). The existence of larger bubbles disturbs the acoustic wave propagation due to wave diffraction and dampening (Hihn et al., 2011), thus hindering the cavitation bubble function and decreasing the mass transfer as well. Furthermore, a high TDG saturation level in the water increases the inside pressure and by that weakens the cavitation intensity (Liu et al., 2014). Nevertheless, ultrasonic degasification is stated to be the fastest way to remove TDG supersaturation within a liquid, as the improvement of the liquid-gas mass transfer even at high pressure and temperature is larger than the aforementioned decreases (Laugier et al., 2008).

Ultrasonic degasification is mostly applied for the degasification of melts, especially liquid metals (Eskin, 2015). Other than that, the method is used by the chemical industry, e.g. degasification of resin solutions or transformer oil, the food industry, e.g. degasification of beverages or food oils, or in the electrochemistry, e.g. deposition of coatings (Kapustina, 1973). Advantages of the use are fast and thorough degasification, and the application is described as an environmentally friendly, economical, and efficient technology (Eskin, 2017).

Degasification in Hydropower

Within the hydropower sector, different measures are currently in use to avoid or mitigate TDG supersaturation introduced by hydropower plants into the downstream waterways. This is dependent on the type of hydropower plant. At hydropower plants with high dams, the regulation of spill operations can lead to a reduction

or avoidance of TDG superaturation. Besides that, mainly constructive methods have been developed, e.g. control structures for flood reliefs at dams to avoid gas solvation (Pulg et al., 2020), or methods leading to aeration due to splashing (Kamal et al., 2020). In case of a need for retrofitting, these methods are time-consuming interferences into the hydropower plant's operation and economically substantial.

For reservoir-type hydropower plants, methods to avoid air intrusion through Brook intakes have been developed, e.g. vacuum gates (Berg, 1992) or automatic detection of intake rist blockage Pulg et al., 2018. These again pose a civil-engineering challenge, coming with similar disadvantages as the aforementioned methods at high dams. In the waterways downstream the hydropower plant, degasification from TDG supersaturated water is substantially increased by aeration using special deflectors at weirs (Pulg et al., 2018). This method is dependent on the local topography and therefore not universally applicable.

Summary

The overview of methods available to enhance the liquid-gas mass transfer of liquids with the aim of reducing the gas saturation is summarized in Table 2.6. As described in Section 2.3.2, the only way to mitigate TDG supersaturation generated by hydropower plants is the aeration method. The versatility of ultrasonic degasification makes its application in multiple fields possible. As presented, the current focus is on reducing the gas saturation of static or slow-moving, small to medium-sized volumes of water. The possibility of applicability for the degasification of large volumes of flowing water has not yet been researched. This Thesis aims on contributing towards answering this scientific question.

Table 2.6: Overview of methods to enhance degasification of liquids and examples of the respective fields of application.

Method	Application examples
Chemical	
	• Metallurgy • Natural gas processing
Increased surface contact or specific interface	
• Aeration	• Aquaculture • Water treatment • Metallurgy
• Spraying	• Hydropower
• Membranes	• Metallurgy • Aquaculture • Water treatment
Modifying thermodynamic conditions	
• Temperature • Pressure	• Industrial steam systems • Nuclear power generation
• Freeze-pump-thaw cycling • Turbulence	• Metallurgy
Mechanophysical techniques	
• Centrifugal	• Metallurgy • Polymer industry
• Ultrasound	• Metallurgy • Food industry • Coating industry

CHAPTER

THREE

Natural degasification in a river

The process of natural degasification due to total dissolved gas (TDG) supersaturation in a Norwegian river downstream a hydropower plant is described by use of the volumetric liquid-gas mass transfer coefficient, $k_L a$. Measurement data of the TDG saturation level in the Otra river is used to evaluate the efficiency of this process. A methodology is developed to determine $k_L a$ in certain stretches of the river, using data deconvolution and certain assumptions on the river's morphology and characteristics. Using this, the $k_L a$ is calculated for multiple TDG supersaturation events. The natural degasification process is dependent on the degree of TDG supersaturation in the water, with higher saturation levels increasing the drive to equilibrium and thus the liquid-gas mass transfer. Following this, the flow of gas is highest between the outlet of Brokke power plant, which generates the TDG supersaturation, and the first measurement station downstream. The volumetric liquid-gas mass transfer coefficient, $k_L a$, shows a similar behaviour, with the highest values being apparent within this stretch of the river. The methodology and assumptions made for the calculation are discussed with regard to the validity of the results.

3.1 TDG supersaturation in the Otra river

The Otra river is a large river in the Agder county in southern Norway. Along its 245 km, a total of 22 hydropower plants with an installed rated capacity of 1078 MW generate electricity (Heggstad and Thorsnæs, 2023). The largest of them is Brokke power plant with an installed rated capacity of 330 MW and an average annual production of 1970 GWh. Build in two steps in 1964 and 1976, the power plant has a total head of 303 m and a discharge of 136 $m^3 s^{-1}$, which is spread between 4 Francis turbines. The main reservoir is Bossvatn, but the power plant features also a large number of Brook intakes (Otra Kraft DA, 2019).

Due to fish mortality and milky-looking water, the Brokke power plant was suspected to generate TDG supersaturation in the Otra river downstream. Since 2011, the Norwegian Research Centre (NORCE) was tasked to implement a surveillance system to monitor the TDG saturation level (Pulg et al., 2016). The TDG sensors used for this were provided by Fisch- und Wassertechnik, and the first sensor was installed at the outlet of the power plant in February 2011. The TDG saturation level was recorded constantly, with measurement values being stored every hour and automatically uploaded to a cloud-based system. The time between storage of data points was decreased to 30 min from October 4th, 2012. In July 2012, additional 3 TDG sensors were installed at 1.2 km, 1.5 km and 8.0 km downstream the power plant outlet. Here, values of the TDG saturation level were stored every 30 min[12]. The positioning of these sensors within the Otra river is displayed in Figure 3.1. The sensor at 1.2 km was moved further downstream in August 2013, and a total of 10 measurement positions up to 30 km downstream the outlet of Brokke power plant were at least partially equipped during the measurement period. The cause of the TDG supersaturation was found in underdimensioned Brook intakes leading to air entrainment and subsequent dissolution in the water within the power plant's waterways. During the measurement campaign, multiple TDG supersaturation events with values of up to 172 %TDG were observed at the outlet of Brokke power plant and in the Otra river downstream. In addition, measurements of the volumetric flow rate in the river at some of the measurement stations are available (Pulg et al., 2016).

The data of this measurement period opens for a unique possibility to evaluate the liquid-gas mass transfer during the natural degasification of TDG supersaturated water in a river between several positions. Even though parameters like the river cross-sectional area or the nature of the river bed are unknown, the volumetric liquid-gas mass transfer coefficient can be determined using assumptions. This is used as a baseline for the comparison with degasification methods. The natural degasification process in the river is represented by dynamic phenomena, e.g. the flow of gas, as well as steady state conditions. It is triggered by the increase in the TDG saturation level due to air dissolution within the power plant. Since the entrainment of air into the power plant is dependent on certain operational modes and boundary conditions, it will only take place in defined situations. Thus, the TDG supersaturation events will in most cases appear as a sudden increase in the TDG saturation, a peak or plateau, and a slower decrease to normal saturation, giving them a wave shape. In addition, the volumetric flow rate transporting the TDG supersaturated water downstream the river is dependent on the normal-saturated environmental flow and the supersaturated discharge of the power plant. Even

[12]Due to a defect on the probe placed 1.5 km downstream, all measurement data until October 4th, 2012 was disregarded.

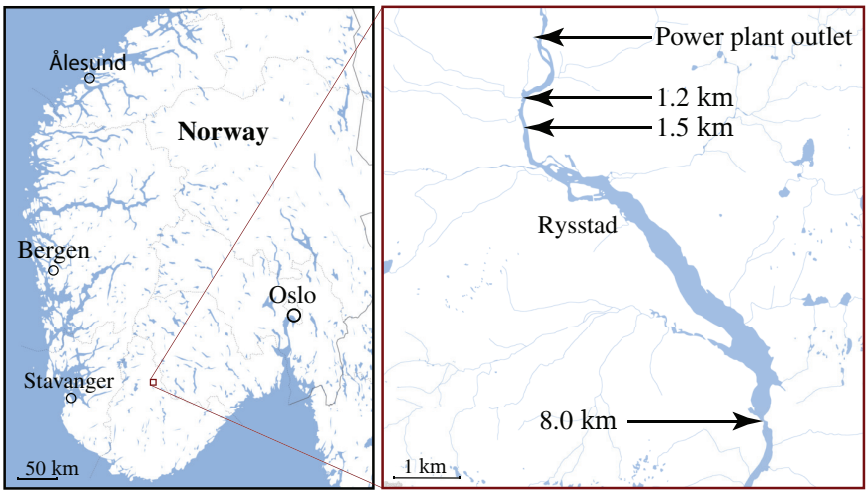

Figure 3.1: Position of Brokke power plant in southern Norway (left) and placement of TDG sensors in the Otra river downstream the hydropower plant in the period of July 2012 to July 2013 (right, adapted from Pulg et al. (2016)). Map material from Snazzy Maps (Krogh, 2023).

though it fluctuates as well, it will correspond to a certain mean value. Knowing this, a calculation method to determine the volumetric liquid-gas mass transfer coefficient is developed and used to evaluate the measurement data. The resulting $k_L a$ then characterizes each river section, as certain features like the riverbed's nature, the water depth, or turbulence are taken into account by the parameter.

3.2 Methodology for calculation of mass transfer due to natural degasification

A methodology for the calculation of the liquid-gas mass transfer coefficient, $k_L a$, during natural degasification of TDG supersaturated water in a river is developed. The theoretical derivation of the equation needed is presented. An example shows the approach during the calculation using measurement data provided by NORCE.

3.2.1 Derivation of a calculation method for the volumetric liquid-gas mass transfer coefficient in a river

As discussed in Section 2.2.1, the volumetric liquid-gas mass transfer coefficient, $k_L a$, is the product of the partial transfer conductance, i.e. the rate of molecular diffusion of the liquid, k_L, and the interfacial area, a. The process at hand is characterized by mass transfer out of solution and dispersion within the river due to turbulence. The river is approximated as an open channel with an in- and outflow,

with the two aforementioned phenomena taking place within the channel segment. A representation of the processes taking place within such a simplified flow is displayed in Figure 3.2.

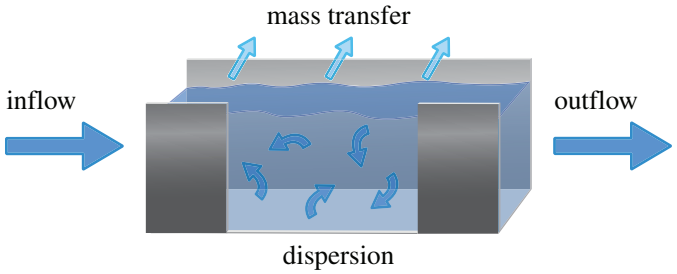

Figure 3.2: Schematic of the natural degasification process in the river, approximated as an open channel flow. Liquid-gas mass transfer takes place at the water surface (light blue arrows), while dissolved gases are dispersed within the volume (curved, blue arrows). Inflow and outflow represent measurement stations with TDG sensors.

A mathematical expression is found in Equation 2.12, which describes the mass transfer between a liquid and a gaseous phase within a volume. In this case, the concentration difference is switched, as the mass transfer takes place from the liquid to the gas phase. In addition, the bulk concentration, C_{bulk}, is replaced by the average gas concentration, $C_{gas,avg}$:

$$\Phi = V\, k_L a \left(C_{gas,avg} - C^*\right). \tag{3.1}$$

In the present case, the data available represents TDG saturation measurements. Therefore, the concentration is replaced by the saturation:

$$\Phi = V\, k_L a \left(S_{\mathrm{TDG},avg} - S^*_{\mathrm{TDG}}\right). \tag{3.2}$$

Here, Φ describes the flow of gas out of the solution, i.e. the loss of TDG, between two measurement points due to degasification, V is the volume of the section, and S^*_{TDG} is the baseline saturation, i.e. the normal TDG saturation level of 100 %TDG. Rearranging the equation leads to an expression for the volumetric liquid-gas mass transfer coefficient:

$$k_L a = \frac{\Phi}{V\left(S_{\mathrm{TDG},avg} - S^*_{\mathrm{TDG}}\right)}. \tag{3.3}$$

As apparent from this equation, the calculation of $k_L a$ is dependent on both Φ and $S_{\mathrm{TDG},avg}$, which consequently need to be determined, first. In addition, the TDG

saturation curves of each wave of supersaturated water detected at the individual measurement stations are changing over time. At the downstream positions, the curves are lengthened in time in comparison to the measured values at the power plant outlet. Therefore, a deconvolution of the curves is needed to calculate the average concentration during the saturation event in between the measurement points. During the deconvolution, a polynomial fit is used on the measurement data, which is then shifted both in x- and y-direction to correct for the time-shift between the measurements. The deconvolution process is explained in detail in Section 3.2.2.

Given two measurement locations A and B, Φ is calculated from the saturation difference multiplied by the volumetric flow rate Q:

$$\Phi = Q\left(S_{\mathrm{TDG},A} - S_{\mathrm{TDG},B}\right). \tag{3.4}$$

Following the aforementioned process, the average TDG saturation for each point is calculated by integrating the polynomial fits of the TDG saturation curves over the occurrence time at the respective position, and subsequently dividing by the occurrence time:

$$\Phi = Q\left(\frac{\int_{t_{As}}^{t_{Ae}} S_{\mathrm{TDG},A}\mathrm{d}t}{t_{Ae} - t_{As}} - \frac{\int_{t_{Bs}}^{t_{Be}} S_{\mathrm{TDG},B}\mathrm{d}t}{t_{Be} - t_{Bs}}\right), \tag{3.5}$$

where t_{As}, t_{Bs}, t_{Ae}, and t_{Be} are the start and end times of the TDG supersaturation waves at measurement point A and B, respectively. During the integration, it is only accounted for the excess TDG saturation, i.e. only values above the baseline concentration. The same applies during the calculation of $S_{\mathrm{TDG},avg}$, which is calculated by averaging the initial concentration at point A and the concentration of the deconvoluted measurement curve from point B:

$$S_{\mathrm{TDG},avg} = \frac{1}{2}\left(\frac{\int_{t_{As}}^{t_{Ae}} S_{\mathrm{TDG},A}\mathrm{d}t + \int_{t_{B's}}^{t_{B'e}} S_{\mathrm{TDG},B'}\mathrm{d}t}{t_{Ae} - t_{As}}\right). \tag{3.6}$$

The $'$ denotes deconvoluted values. Inserting Equations 3.5 and 3.6 into Equation 3.3, the final expression for $k_L a$ during the natural degasification process in the river is derived:

$$k_L a = \frac{Q\left(\frac{\int_{t_{As}}^{t_{Ae}} S_{\mathrm{TDG},A}\mathrm{d}t}{t_{Ae}-t_{As}} - \frac{\int_{t_{Bs}}^{t_{Be}} S_{\mathrm{TDG},B}\mathrm{d}t}{t_{Be}-t_{Bs}}\right)}{V\left(\frac{1}{2}\left(\frac{\int_{t_{As}}^{t_{Ae}} S_{\mathrm{TDG},A}\mathrm{d}t + \int_{t_{B's}}^{t_{B'e}} S_{\mathrm{TDG},B'}\mathrm{d}t}{t_{Ae}-t_{As}}\right) - S^{*}_{\mathrm{TDG}}\right)}. \tag{3.7}$$

3.2.2 Example calculation of the volumetric liquid-gas mass transfer coefficient in a river using measurement data

The determination of the volumetric liquid-gas mass transfer coefficient between two measurement stations during the natural degasification process in a river is explained using measurement data from a TDG supersaturation wave occurring on August 3rd, 2012. It is possible to directly take the measured saturation values for the calculation instead of calculating the corresponding (mass or molar) concentration, as this is canceled on the right-hand side of Equation 3.7. This is of advantage, as it also removes the need to take the water temperature into account during the calculation. The TDG saturation measured at the outlet of Brokke power plant and the measurement station 8.0 km downstream is displayed in Figure 3.3. From the two measurement curves, both the decrease in TDG saturation level as well as a lengthening of the duration of occurrence are apparent. The decrease is primarily due to natural degasification, while some of it takes place due to mixing effects in the river. These are also responsible for the change in the distribution of the TDG saturation level.

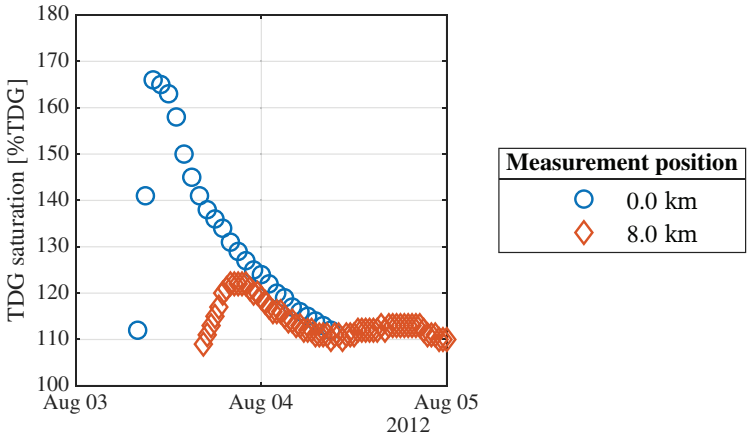

Figure 3.3: Measurement data during one TDG supersaturation wave at the outlet of Brokke power plant and 8.0 km downstream.

The measurement data curves are fitted using the polyfit-function in MATLAB R2022b. This function fits data points to a polynomial with a degree n and returns the coefficients representing a polynomial equation in the shape of:

$$p(x) = p_1 x^i + p_2 x^{i-1} + \ldots + p_i x + p_{i+1}. \tag{3.8}$$

As the shape of the individual TDG supersaturation curves is varying, the degree of the polynomial equation is set to nine to get the best possible fit. This leads in some cases to polynomial coefficients being very small, especially in case of higher-order

coefficients. The resulting polynomials for this example are presented by Equations 3.9 and 3.10, and the measurement data including the fitted curves is displayed in Figure 3.4.

$$p_{0.0\,\mathrm{km}}(x) = -3.39 \cdot 10^{-8}x^9 + 3.91 \cdot 10^{-6}x^8 - 1.88 \cdot 10^{-4}x^7 + 0.48 \cdot 10^{-2}x^6 - 0.07x^5 + 0.53x^4 - 1.44x^3 - 5.92x^2 + 39.45x + 111.36 \tag{3.9}$$

$$p_{8.0\,\mathrm{km}}(x) = -0.11 \cdot 10^{-8}x^9 + 0.25 \cdot 10^{-6}x^8 - 0.25 \cdot 10^{-4}x^7 + 0.14 \cdot 10^{-2}x^6 - 0.05x^5 + 1.12x^4 - 16.23x^3 + 143.71x^2 - 696.89x + 1506.51 \tag{3.10}$$

The coefficients of determination for the two polynomial fits are $R^2_{0.0\,\mathrm{km}} = 0.9950$ and $R^2_{8.0\,\mathrm{km}} = 0.9592$, respectively.

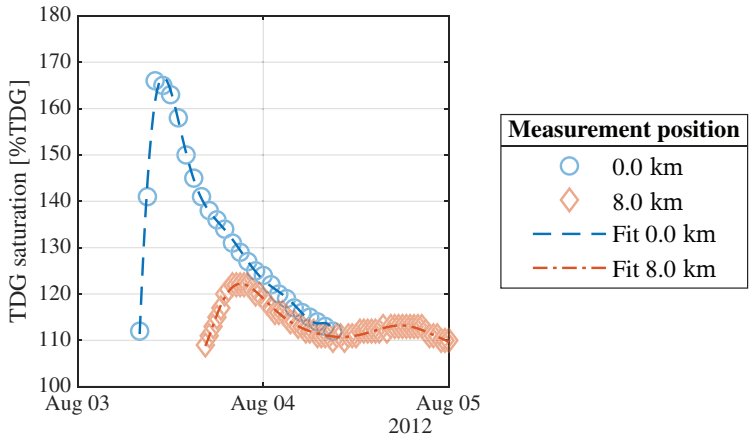

Figure 3.4: Measurement data during one TDG supersaturation wave at the outlet of Brokke power plant and 8.0 km downstream, including the respective polynomial fit.

In the next step, the polynomials are integrated from the start to the end time of the occurrence in order to retain the area underneath the graphs. As mentioned earlier, only the excess TDG content is of interest, meaning that the integration takes place from the baseline, i.e. 100 %TDG. The resulting values are 825.14 %TDG s and 446.15 %TDG s at the 0.0 km and 8.0 km measurement stations, respectively. Following Equation 3.5, these values are divided by the occurrence time of the respective curve ($t_{0.0\,\mathrm{km}} = 25$ h and $t_{8.0\,\mathrm{km}} = 32$ h). The difference of the resulting average TDG saturations is then multiplied by the volumetric flow rate, for which the

annual average of 93.87 $m^3\,s^{-1}$ for the measurement period is used[13]. The resulting loss of TDG between the outlet of Brokke power plant and the measurement station 8.0 km downstream is $\Phi = 1789.51\,\%\mathrm{TDG}\,m^3\,s^{-1}$. Converting the saturation to mass concentration using the value $C_{air} = 31.37\,g\,m^{-3}$ at $T = 10\,°C$ gives a more understandable representation of the loss, resulting in $\Phi = 561.37\,g\,s^{-1}$.

Now, the deconvolution of the polynomial fit of the measurement values at the 8.0 km measurement station takes place to make the calculation of the average gas concentration during the TDG supersaturation event possible. The need for deconvolution arises due to the lengthening of the occurrence time in comparison to the one at the power plant outlet. The time correction is made by multiplying the time since the start of the TDG supersaturation wave at the 8.0 km measurement station, $t_{Bi} - t_{Bs}$, with a factor derived from the ratio of the respective total time of occurrence of the TDG supersaturation wave at the outlet and the downstream measurement station:

$$t_{corr,i} = \left(t_{B,i} - t_{Bs}\right) \frac{t_{Ae} - t_{As}}{t_{Be} - t_{Bs}}. \tag{3.11}$$

This results in a shortened total time of occurrence which is in line with the time of occurrence at the outlet of Brokke power plant. The measurement values of the TDG saturation level need to be deconvoluted to agree with the new time values. For this, each measurement value is corrected by adding the residence time of the water in the river between the power plant outlet and the measurement station, τ, multiplied by the slope of the initial concentration increase:

$$S_{\mathrm{TDG},B'}(t) = S_{\mathrm{TDG},B}(t_{corr}) + \tau \frac{\mathrm{d}S_{\mathrm{TDG},B}(t_{corr})}{\mathrm{d}t_{corr}}. \tag{3.12}$$

The residence time in this example represents the time a fluid element needs to travel from the outlet of Brokke power plant to the measurement station 8.0 km downstream. It is determined by dividing the volume of the river between the respective measurement stations by the volumetric flow rate:

$$\tau_i = \frac{V_i}{Q}. \tag{3.13}$$

To calculate the volume, a simplification is made by assuming conic sections. The cross-sectional areas at the measurement stations are determined from topological models made available by NORCE. From those, the rough width of the river at the position was determined and multiplied by the respective average depth. The resulting cross-sections are 145 m^2, 185 m^2, 135 m^2 and 75 m^2 for the outlet of

[13]The volumetric flow rate was measured at the hydrological measurement station Hovet, 0.5 km downstream the outlet of Brokke power plant.

Brokke power plant and the 1.2 km, 1.5 km and 8.0 km downstream measurement stations, respectively. Thus, the residence time for the example is calculated to $\tau_B = 3.30\,\text{h}$. The resulting, deconvoluted TDG saturation curve is displayed in Figure 3.5.

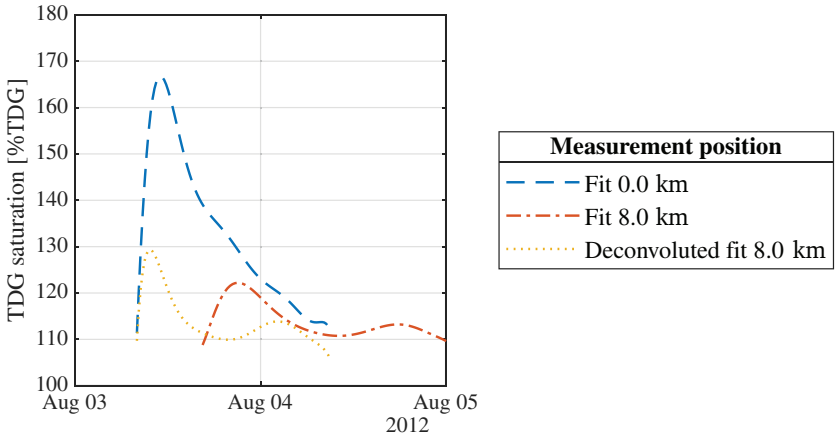

Figure 3.5: Polynomial fits of measurement data and deconvoluted polynomial fit of the measurement data at the 8.0 km downstream measurement station, showing both the correction in time to fit the occurrence time at the power plant outlet and the subsequent correction of the values.

The final step to calculate the average TDG concentration is averaging the polynomial fit of the measurement data at the outlet of Brokke power plant and the deconvoluted polynomial fit of the 8.0 km downstream measurement station, as presented in Equation 3.6. A representation of the average TDG saturation is displayed in Figure 3.6. The average TDG saturation for this example is then calculated to 111.74 %TDG[14].

The volumetric liquid-gas mass transfer coefficient is now calculated using Equation 3.7, taking the results for the TDG loss and the average TDG saturation. The volume between the power plant outlet and the measurement station, $V_{8.0\,\text{km}}$, is calculated by summation of the frustum-volumes between the four conical sections presented earlier.

$$\begin{aligned} k_L a &= \frac{1789.51\,\%\text{TDG}\,\text{m}^3\,\text{s}^{-1}}{1.12 \cdot 10^6\,\text{m}^3\,(111.74\,\%\text{TDG} - 100\,\%\text{TDG})} \\ &= 0.68 \cdot 10^{-4}\,\text{s}^{-1}. \end{aligned} \tag{3.14}$$

[14]As the integration is only made with regard to supersaturation values, the actual result is 11.74 %TDG. This removes the need to subtract the baseline saturation of 100 %TDG in Equations 3.7 and 3.14.

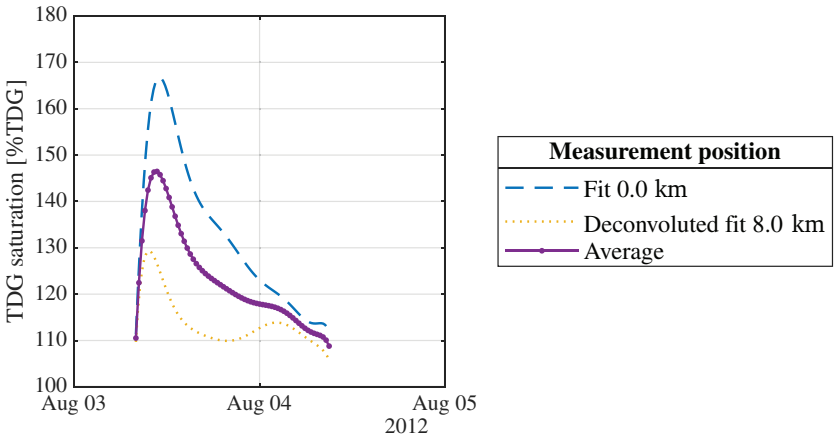

Figure 3.6: Step-by-step process of calculating the average concentration from measurement data by polynomial fitting and deconvolution.

The method presented above is applied to measurement data provided by NORCE. This data contains TDG saturation levels in the Otra river at the outlet of Brokke power plant and the measurement positions 1.2 km, 1.5 km and 8.0 km downstream. It was screened for TDG supersaturation waves in the period July 10th, 2012, to December 31st, 2013. A total of 14 events were evaluated for 2012, while only 6 were applicable in 2013. The calculation of the volumetric liquid-gas mass transfer coefficient is then conducted in the same manner as described in this section, taking the measurement values from the power plant outlet and the respective downstream position.

3.3 Results and discussion

With NORCE's measurement data and the method described in Section 3.2, the liquid-gas mass transfer coefficient, k_a, is calculated for a total of 18 TDG supersaturation events in the Otra river. The distribution of the maximum measured TDG saturation level at all measurement stations for the selected TDG supersaturation waves in 2012 and 2013 is displayed in Figure 3.7. The mean TDG saturation level is 160.00 %TDG, 135.10 %TDG, 130.75 %TDG and 119.22 %TDG, while the median of the data is 169.09 %TDG, 136.31 %TDG, 126.35 %TDG and 121.55 %TDG for the measurements taken at the power plant outlet and 1.2 km, 1.5 km and 8.0 km downstream, respectively. Thus, the natural degasification process is most efficient up to the first two measurement stations, as the decline in maximum measured TDG saturation is the highest there. This is in agreement with the findings of Pulg et al., 2016, and is explained by the main reason for the natural degasification, i.e. the drive to equilibrium. With the power plant outlet representing

the source for the TDG supersaturated water, no further increase takes place in the river downstream, meaning that the total gas pressure (TGP) is the highest at this position. As a high TGP leads to a higher drive to equilibrium, the flow of gas is increased, but both decrease with increasing distance due to the ongoing natural degasification.

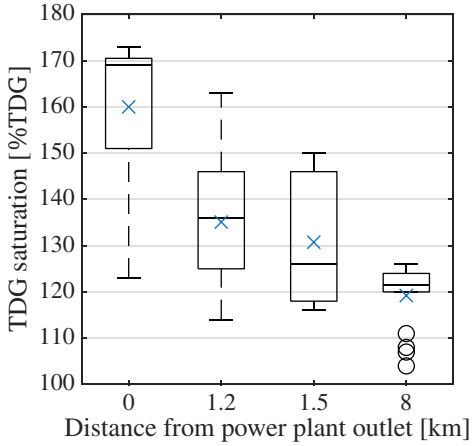

Figure 3.7: Distribution of maximum measured TDG saturation level at the outlet of Brokke power plant and downstream measurement stations. Boxes showing the interquartile range including median. Top and bottom line showing maximum and minimum. Outliers shown by ○, mean values indicated by ×.

Similar results are found for the calculation of the volumetric liquid-gas mass transfer coefficient from the selected TDG supersaturation waves in 2012 and 2013. The distribution of $k_L a$ values is displayed in Figure 3.8. While the spread in values is distinct for the values calculated between Brokke power plant outlet and the first two measurement stations, the values at 8.0 km downstream are close together, which is due to the high natural degasification and the long distance to the other measurement stations.

All values for the maximum measured TDG saturation level and the respective calculated $k_L a$ values for the selected TDG supersaturation events are listed in Table A.1. From this, the mean volumetric liquid-gas mass transfer coefficient for natural degasification of TDG supersaturated water in the Otra river downstream Brokke power plant is calculated to $2.54 \cdot 10^{-4}\,\mathrm{s}^{-1}$, $2.38 \cdot 10^{-4}\,\mathrm{s}^{-1}$ and $0.82 \cdot 10^{-4}\,\mathrm{s}^{-1}$ for the river stretches between the power plant outlet and the measurement stations 1.2 km, 1.5 km and 8.0 km downstream, respectively. The corresponding median values are $2.22 \cdot 10^{-4}\,\mathrm{s}^{-1}$, $2.27 \cdot 10^{-4}\,\mathrm{s}^{-1}$ and $0.77 \cdot 10^{-4}\,\mathrm{s}^{-1}$.

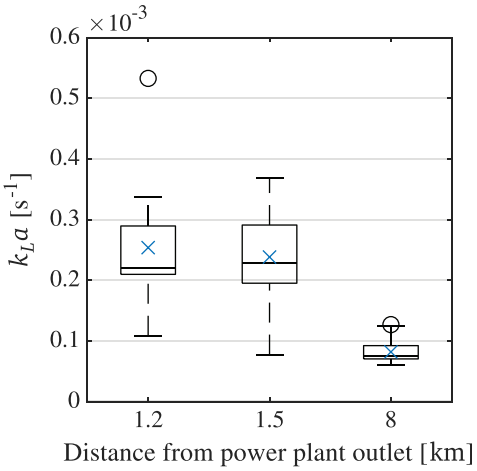

Figure 3.8: Distribution of the volumetric liquid-gas mass transfer coefficient, $k_L a$, at the outlet of Brokke power plant and downstream measurement stations. Boxes showing the interquartile range including median. Top and bottom line showing maximum and minimum. Outliers shown by ○, mean values indicated by ×.

Comparing Figures 3.7 and 3.8, the trends of the mean values are similar, even though the difference between the TDG saturation at the 1.2 km and 1.5 km measurement stations is larger than the difference between the calculated volumetric liquid-gas mass transfer coefficient at these positions. While the drive to equilibrium is highest in the first river sections downstream the power plant outlet due to the higher TDG saturation values, the $k_L a$ is large due to the river's morphology and characteristics in these stretches. This reveals an issue of the model, as the results are achieved using certain assumptions and simplifications. First, the river geometry is very simplified by calculating conic sections using the cross-sectional areas at the respective measurement positions. As apparent in Figure 3.1, the river is narrow directly downstream the outlet of Brokke power plant, before widening significantly at about 2.5 km downstream. The flow velocity is therefore potentially much higher in the narrow section of the river compared to the wider part. On the other hand, no information is available about the river depth, even though the wide section of river is assumed to develop due to a higher depth. Within the first river section, there are also some turns visible. Those can in combination with higher velocities contribute to higher turbulence intensity within this part, which increases the mass transfer and thus the natural degasification. Accordingly, the low velocities in the wider section and the limited changes in flow direction assumable lead to lower turbulence and therefore slower natural degasification. Another disregarded factor influencing turbulence in the river is the nature of the river bed, for which no information is available. Despite those assumptions, the calculated $k_L a$ values are

in agreement with observations related to the river's morphology, even though no thorough knowledge about the river's morphology and characteristics is available. Thus, the results show the possibility to determine the volumetric liquid-gas mass transfer coefficient using the presented model.

The second major simplification regards the volumetric flow rate of the river, which is taken into account as the average volumetric flow rate within the Otra river measured shortly downstream the power plant outlet, and which is assumed to be constant for all calculations. This is somewhat contradicting the fact that TDG supersaturation events at Brokke power plant occur in connection with flooding. As the flow rate cannot be separated into the power plant's discharge and the environmental flow, the error is assumed to be neglectable.

The final assumption stems from the polynomial fit, which is introducing errors due to the limited capability to give an exact representation. Nevertheless, the coefficients of determination obtained for the example calculation in Section 3.2.2 imply a good agreement. Thus, the error introduced by this assumption is assumed to be small in comparison to the aforementioned assumptions and simplifications.

An additional potential source of errors are the long measurement intervals of the TDG sensors. This leads to uncertainties in the actual shape (e.g. size and length) of the TDG supersaturation events and makes an exact determination of the maximum TDG difficult. Nevertheless, the general trends are assumed to be captured by the available data, thus giving a good indication of the volumetric liquid-gas mass transfer coefficient during the natural degasification process in a river.

The comparison with $k_L a$ values reported by literature is difficult, as mass transfer usually is evaluated in relation to certain methods having an enhancing effect on it. Yet, these values will provide an idea of the plausibility of the results achieved using the calculation method. Ho et al. (2020) review methods to enhance the volumetric liquid-gas mass transfer within gas diffusion systems. They report maximum $k_L a$ values for different methods in the range of $3.5 \cdot 10^{-3}\ \mathrm{s}^{-1}$ to $0.4\ \mathrm{s}^{-1}$. The oxygen transfer in microbial processes was studied by Garcia-Ochoa and Gomez (2009). A review of different mass transfer coefficient evaluation methods is given, showing a maximum range distribution of $1 \cdot 10^{-3}\ \mathrm{s}^{-1}$ to $5 \cdot 10^{-3}\ \mathrm{s}^{-1}$. Similarly, Tribe et al. (1995) provide a range of oxygen mass transfer for a dynamic method of $0.01\ \mathrm{s}^{-1}$ to $0.15\ \mathrm{s}^{-1}$. Alvarez et al. (2002) show mass transfer coefficients in batch regime of $1.5 \cdot 10^{-3}\ \mathrm{s}^{-1}$ to $2.75 \cdot 10^{-3}\ \mathrm{s}^{-1}$. Compared to these values, the $k_L a$ range determined using the presented method is at least one range of magnitude lower. However, this comparison falls short, as the studies aim on optimizing the liquid-gas mass transfer in controlled, laboratory conditions. The range of magnitude of the river's $k_L a$ values is therefore plausible. Altogether, the natural degasification process has

to be seen as a very slow process, which also is reported by Pulg et al. (2016), who calculate an average TDG decrease in the river of 2.8 %TDG km^{-1}.

The results for the volumetric liquid-gas mass transfer coefficient during natural degasification of TDG supersaturation in a river obtained using the method presented in Section 3.2 are unique. No other report in the literature is found to attempt this calculation. Therefore, the results cannot be properly verified by comparison, and have to be seen as an indication of the actual mass transfer taking place. Also, the data available is restricted to one river with its specific geometry and nature. In the future, more data from other rivers or numerical simulations of the natural degasification process in a river may be available to confirm and improve the method.

3.4 Conclusion

The mass transfer during natural degasification due to TDG supersaturation in the Otra river downstream Brokke power plant has been determined. A method was developed to calculate the volumetric liquid-gas mass transfer coefficient from TDG saturation measurement data. Multiple assumptions and simplifications are made and have been discussed with regard to the validity of the final results. The mean $k_L a$ between the power plant outlet and the first measurement station 1.2 km downstream is $2.54 \cdot 10^{-4}$ s^{-1}. The values between the power plant outlet and the measurement stations further downstream are lower due to the decrease in TGP and thus less drive to equilibrium. The natural degasification process is slow compared to processes found in the literature, even though those are mostly indicating mass transfer enhancement processes.

To prevent the aquatic ecology in a river from the consequences of artificial TDG supersaturation, the mass transfer needs to be increased substantially. The estimation of required $k_L a$ values to efficiently decrease TDG saturation values to ecologically tolerable values made in Section 2.2.2 shows values of one to two orders of magnitude higher than the values found within this chapter. Therefore, degasification applications are needed to provide such a large enhancement of mass transfer.

Nevertheless, the values calculated provide a first idea of the efficiency of the natural degasification process in a river. Even though the results are for the moment only applicable to the Otra river downstream Brokke power plant, they indicate the range of magnitude of the natural degasification capacity of a natural flow, as well as the limits of mass transfer taking place in natural conditions. They will serve further as a baseline for comparison with degasification enhancement methods to evaluate their potential to mitigate TDG supersaturation effects.

CHAPTER
FOUR

Dependence of liquid-gas mass transfer on selected operating parameters

Liquid-gas mass transfer is dependent on multiple parameters, as introduced and discussed in Section 2.2.1. Different studies on the enhancement of mass transfer for singular gases exist, but the case of the total dissolved gas (TDG) saturation level, especially during supersaturation, is understudied. Several parameters for the mass transfer in TDG supersaturated water are presented, studied, and discussed in this chapter. The target is to estimate the change in the volumetric liquid-gas mass transfer coefficient, $k_L a$, for selected operating parameters by measuring the TDG saturation level within the water.

An experimental setup is prepared that is capable of generating a supersaturation of different gases in water. This is used for a study of operating parameter and their effect on the liquid-gas mass transfer in a batch reactor. A focus is put on combining selected parameters with sonication using power ultrasound. The results give an insight into the efficiency of different methods to enhance the degasification of TDG supersaturated water and lead to the development of an empirical model.

4.1 Methods

The study of liquid-gas mass transfer enhancement within TDG supersaturated water requires an experimental setup with multiple steps: first, the TDG saturation level in water needs to be increased to a desired degree of supersaturation. The resulting TDG supersaturated water is then in a second step transferred to a batch reactor, with a need of limiting losses, i.e. the amount of natural degasification taking place. Within the reactor, the parameters affecting the mass transfer are tested in a controlled environment. A simplified representation of the experimental procedure during the batch reactor tests is displayed in Figure 4.1. The different methods to achieve these steps are described in this section, together with the

equipment needed to conduct the parameter study. In addition, the calculation of the liquid-gas mass transfer coefficient from the measurement data is described. All experiments are conducted in the Hydrogen Energy and Sonochemistry Laboratory at NTNU.

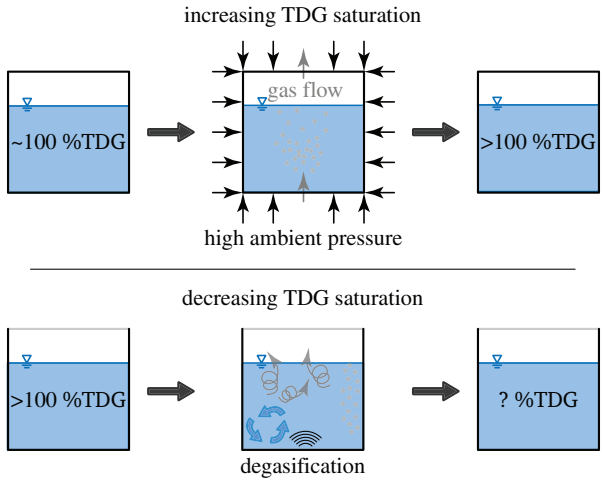

Figure 4.1: Schematic of the experimental procedure for the batch reactor experiments.

4.1.1 Increasing the TDG saturation level

To increase the TDG saturation level, the ambient pressure of the system needs to be increased, as discussed in Section 2.2.1. This is achieved by designing and building a pressure vessel with an air inlet at the bottom and an adjustable Brewtools pressure relief valve with a pressure range of 0 bar to 2.2 bar at the top. Flushing in gas at a pressure higher than atmospheric pressure increases the ambient pressure, thus leading to increased solubility and, over time, higher gas concentration. The vessel is a stainless steel cylinder with an inner diameter of 147 mm and a height of 147 mm, which is closed with cylindrical, stainless steel plates on both the top and the bottom. The resulting volume is $V_{pv} \approx 2.5\,\mathrm{dm}^3$. Besides the gas inlet and the pressure relief valve, there is an inlet pipe for filling the vessel on top and an outlet pipe for draining it at the bottom. In addition, a pressure sensor is installed on the top to record the ambient pressure, and a valve to evacuate the pressure after finishing the saturation process. The pressure vessel is displayed both by a schematic and a picture in Figure 4.2.

In order to increase the mass transfer during dissolution of the gas, the liquid-gas interfacial area is increased by using a gas diffuser (or sparger) to create bubbles that are distributed from the bottom of the vessel. The diffuser is a cylindrical, porous media with a diameter of 12.7 mm, a height of 25 mm, and a pore size of 0.5 µm.

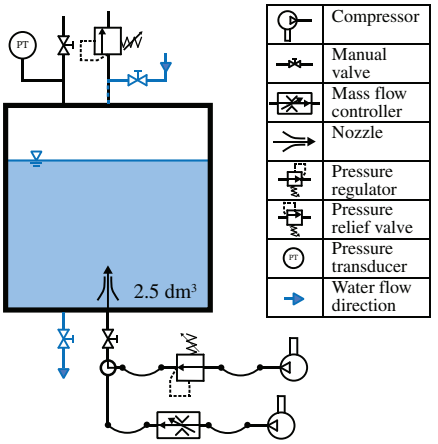

(a) Schematic of the pressure vessel.

(b) The pressure vessel inside the Hydrogen Energy and Sonochemistry Laboratory at NTNU.

Figure 4.2: Schematic and picture of the pressure vessel used for increasing the TDG saturation in water.

To ensure gas flow through the system, the gas pressure is set to a value higher than the relief pressure of the valve. For this, a Festo MS6-LRP pressure regulator with a range of 0.05 bar to 2.5 bar is used in case of air, while Alicat Scientific MC-Series mass flow controllers are used for single air-content gases. During the experiments, water is supersaturated with the main air-content gases Nitrogen, N_2, and Oxygen, O_2, as well as with air.

The maximum mass flow available is 20 SLPM, which is used as a set-point for N_2 and O_2. The gases are supplied from a pressurized in-house storage. For air, the maximum air pressure delivered by an in-house compression system is 7 bar. This is regulated down to 1.5 bar to match the pressure induced by the mass flow of the single air-content gases. The pressure inside the pressure vessel is monitored using a GE UNIK 5000 pressure sensor (PTX 5072) with a range of 0 bar absolute to 3 bar absolute, and the data is recorded using a National Instruments (NI) data acquisition (DAQ) module and NI LabVIEW with a sampling frequency of 1 Hz. This sensor is calibrated in-house using a GE P3223-1 hydraulic deadweight tester. With constant pressure and continuous gas bubbling, the mass transfer of gas into the liquid is increased, and thus the gas concentration changes over time.

A volume of 1.6 dm^3 of pure water is taken during one supersaturation procedure. The water is supplied by a Stakpure OmniaTap II, which provides water with an electroconductivity of ≤ 0.1 $\mu S\ cm^{-1}$ (at 25 °C water temperature). The water is filled into the pressure vessel from the top, and all valves are closed. The

pressure relief valve is set to 1.7 bar. Then, the gas pressure is regulated using the pressure regulator in case of air, or the mass flow controllers in case of N_2 and O_2. Opening the bottom valve leads to inflow of gas and subsequently to a system pressure increase up to the point where the pressure relief valve opens and slips out excess gas. The waiting time is 2 h to allow for a sufficient increase in the gas concentration.

After the supersaturation process, the gas supply is stopped and the pressure is slowly evacuated from the top air valve. Then, the water is released from the bottom water valve through a 1 m long hose into a 1 dm^3 graduated cylinder. The hose allows for a more smooth transition of the water leaving the pressure vessel, as pressure losses decrease the pressure step at the outlet, and thus prevents natural degasification (this will be further elaborated upon in Section 5.1.2). A TDG measurement within the pressure vessel is not conducted due to operational restrictions, e.g. the pressure-tightness of the vessel, which prevents quick access to the liquid bulk.

4.1.2 The batch reactor for static mass transfer experiments

The reactor used for the investigations of parameters influencing the liquid-gas mass transfer is a Meinhardt Ultrasonics 1 dm^3 glass reactor featuring double-walls for cooling. It has two inlets on the top and the bottom of one side to give access to the cooling water circulation, and two inlets on the top and the bottom on the other side to have access to the batch. The cooled batch section has an outer diameter of 90 mm, an inner diameter of 70 mm, and a height of 250 mm. The total height of the reactor is 380 mm. At the bottom, a circular opening with a diameter of 56.5 mm is used for mounting the ultrasonic transducer in use. In case of transducers provided by Meinhardt Ultrasonics, the mounting is done directly onto the reactor, with a rubber ring in between for sealing purposes. A gland on both reactor and transducer allows for connecting the parts using a wooden screw clamp. For the SinapTec transducer used, a synthetic ring on the horn provides the sealing surface. The connection is done using 3D-printed platforms and screws. Pictures taken from the three different ultrasonic transducers mounted to the reactor are displayed in Figure 4.3.

Cooling water is provided by a Neslab RTE-221 refrigerated bath, and the circulation is implemented using an external Marco Fluidtech UP3/E electronic gear pump controlled by an Agilent E3633A DC power supply set to 12 V. The cooling temperature is set with regard to the ultrasonic transducer in use and the respective ultrasonic power, as those define the rise in temperature during sonication. Throughout all experiments, the TDG saturation level is monitored using an InWater Technologies PT4 TDG sensor, and the temperature is measured using a PT100 resistance thermometer. A calibration of the TDG sensor is achieved using a pressure chamber method, as described by Pleizier et al. (2021a). Tests

(a) Reactor with mounted Sinaptec 20 kHz transducer.

(b) Reactor with mounted Meinhard Ultrasonics 40 kHz transducer.

(c) Reactor with mounted Meinhard Ultrasonics multi-frequency transducer.

Figure 4.3: Batch reactor used during the experiments, with the different transducers mounted.

show that there is no difference between calibrating the sensor with the attached membrane cartridge and without, which is why the sensor is calibrated without the membrane due to faster response times of built-in pressure sensor. The atmospheric pressure is measured by a GE UNIK 5000 pressure sensor (PTX 5072) with a range of 0 bar absolute to 3 bar absolute, which is calibrated in-house using a GE P3223-1 hydraulic deadweight tester. Both TDG sensor and thermometer are centered within the upper part of the batch reactor, while the pressure sensor is kept next to it. In addition, a Sensorex pH3400 is monitoring the pH within the reactor. The data is collected using NI DAQ modules and NI LabVIEW, using a sampling frequency of 5 Hz. A schematic overview of the batch reactor, including the experimental equipment described in the following sections, is depicted in Figure 4.4.

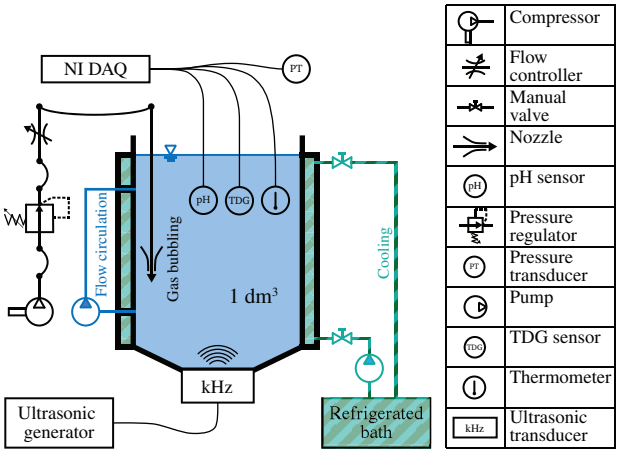

Figure 4.4: Schematic of the experimental setup of the batch reactor. All devices needed for the parameter tests are included, and the position of the gas bubbling and the flow circulation loop are marked separately. The circulation pump can be turned to change the flow direction, and the ultrasonic transducer's shape differs among the different units used. The data acquisition from the sensors is performed by NI DAQ modules.

Ultrasonic equipment

In total, three different ultrasonic transducers are used to evaluate the enhancement of the liquid-gas mass transfer within the batch reactor. The first two are provided by Meinhard Ultrasonics, while the third one is made by SinapTec. The lowest frequency tested is provided by a 20 kHz SinapTec horn transducer, which is powered by a NexTgen Lab500 generator. The horn tip has a diameter of 25 mm, and the maximum set-power of the generator to the transducer is 400 W. All settings are given externally to the generator using the NexTgen software, and feedback mechanisms allow for a real-time evaluation of the transducer's operating parameters. These are used to calculate the mean power transmitted to the transducer during the sonication.

In contrast, the Meinhard Ultrasonics transducers are both flat transducers. The first operates at 40 kHz and has a simple generator that allows for setting the amplitude to 20 %, 40 %, 60 %, 80 % and 100 % of the maximum amplitude, 50 W. Its plate has a diameter of 60 mm. The second flat transducer is an E/805/T, which has the operating frequencies of 570 kHz, 850 kHz and 1140 kHz, and a plate diameter of 52.5 mm. It is supplied by a Meinhard Ultrasonics multifrequency system, which generates frequencies of 0.2 MHz to 10 MHz with a maximum amplitude of 250 W. This system is controlled via a built-in touch display, and both frequency and amplitude are adjustable within the respective ranges. During

the experiments, the only frequency used is 580 kHz. Due to lacking feedback data, the power transmitted from the generator to the transducer is calculated using the amplitude setting, i.e. a percentage of the maximum power. The ultrasonic transducers are displayed in a mounted state in Figure 4.3 as well as in a top and side view in Figure 4.5, and a summary of their properties is given in Table 4.1.

(a) SinapTec 20 kHz transducer

(b) Meinhardt Ultrasonics 40 kHz transducer

(c) Meinhardt Ultrasonics multi-frequency transducer

Figure 4.5: Top and side view of the transducers used during the batch experiments. Transducers in (a), (b) and (c) are not to scale among each other.

Table 4.1: Properties of the three ultrasonic transducers used during the batch degasification experiments.

Manufacturer	Transducer type	Frequency [kHz]	Max. acoustic power [W]
SinapTec	horn	20	400
Meinhardt Ultrasonics	flat	40	50
Meinhardt Ultrasonics	flat	580, 850, and 1140	250

The acoustic power transmitted by the respective ultrasonic transducer to the liquid bulk is determined using the calorimetric method, as described by e.g. Margulis and Margulis (2003). This method relies on the measurement of the heat being dissipated by the transducer into the water, assuming that all the acoustic energy absorbed by the water is transformed into heat (Hansen et al., 2021). The acoustic

power is then calculated by taking the volume and the specific heat capacity of the water into account:

$$P_{ac} = mC_p \left(\frac{\mathrm{d}T}{\mathrm{d}t} \right)_{t=0}, \tag{4.1}$$

where m is the mass of the volume, C_p is the specific heat capacity of water, which is 4186 J kg^{-1} K^{-1} at 20 °C, and T is the temperature in K. The measurements take place inside the batch reactor without cooling. The thermometer is centered within 1 dm^3 of water, and the batch is subsequently sonicated for 5 min. By changing the respective generator's amplitude setting, different acoustic powers are achieved. Thus, all transducers are tested for 20 %, 40 %, 60 %, 80 % and 100 % amplitude (in case of the SinapTec transducer, the lowest amplitude setting tested is 33 %). Each data point was recorded twice. From the measured temperature slope, the acoustic power for the respective amplitude setting is calculated using Equation 4.1. The resulting, averaged data points for the three transducers are displayed in Figure 4.6. Both the SinapTec 20 kHz transducer and the Meinhardt Ultrasonics 40 kHz transducer fit with the same linear trends and have the same proportionality, while the Meinhardt Ultrasonics 580 kHz transducer, working at a higher frequency range, shows a slight deviation and rather follows a squared fit. To get the regression curves, the polyfit-function in MATLAB R2022b is used. The equations of the regression curves and the respective coefficients of determination are listed in Table 4.2.

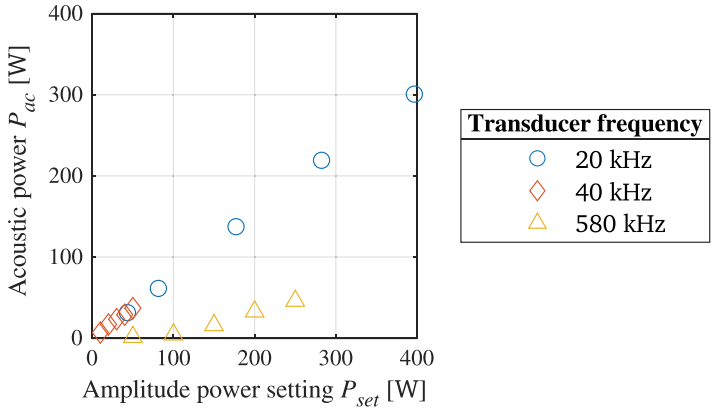

Figure 4.6: Acoustic power, P_{ac}, transmitted by the different ultrasonic transducers over the amplitude power setting. The data is available in Table A.2.

The ultrasonic equipment is used for multiple, different experiments. First, the effect of ultrasonication on the liquid-gas mass transfer in liquids supersaturated with air, N_2, and O_2 is investigated. Here, the SinapTec, with a low (10 %) and a full amplitude setting, and the Meinhard Ultrasonics 40 kHz transducer at full

Table 4.2: Regression curve equations for the acoustic power of the three transducers and respective coefficient of determination, R^2, determined using data points from calorimetric acoustic power determination.

Manufacturer	Frequency [kHz]	Regression curve	R^2
SinapTec	20	$0.77P_{set} - 0.18$	0.9997
Meinhardt Ultrasonics	40	$0.72P_{set} + 1.03$	0.9948
Meinhardt Ultrasonics	580	$7.36 \cdot 10^{-4} P_{set}^2 + 1.39 \cdot 10^{-2} P_{set} - 2.20$	0.9994

amplitude are compared. 0.75 dm^3 of pure water with a saturation of 120 %TDG is sonicated for 10 min in the batch reactor (as the TDG sensor displaces too much liquid volume to allow for a full reactor). To allow the TDG sensor to adjust to the increased TDG saturation, a waiting time of 10 min is set between the filling of the reactor and the start of the sonication. Cooling is applied to keep the temperature within the liquid at 20 °C. The experiment is conducted twice for each measurement point.

In a second experiment, a comparison of the liquid-gas mass transfer coefficient between the three transducers and their respective frequencies is achieved. For this, the batch reactor is again filled with 0.75 dm^3 TDG supersaturated water at 120 %TDG and sonicated at the same transmitted acoustic power of about 37 W. After allowing the TDG sensor to adjust, the batch is sonicated for 10 min, keeping the temperature constant at 20 °C. Again, duplicates of each data point are recorded.

In addition to the frequency comparison study, the effect of the SinapTec 20 kHz transducer at higher acoustic amplitudes is studied to see the influence of the acoustic power. The experimental procedure is similar to the ones before, with the difference of changing the amplitude setting of the transducer to 50 %, 60 %, 80 % and 100 %. The first setting was tested once, the second and third twice, and four measurements were conducted at full power, as the transferred power of the transducer is varying at this point.

The SinapTec transducer is also used for researching the combining effect of sonication and other parameters to increase the liquid-gas mass transfer coefficient. Further details are given in the following sections.

Flow circulation equipment

To evaluate the effect of a flow being introduced to the batch reactor, pumps are used to circulate the TDG supersaturated water. The batch reactor's access points on the top at the bottom of the cooling section provide access to hoses being connected to the pump in- and outlet. A maximum flow circulation of 5 $dm^3\ min^{-1}$ is desired.

This is reached by using a Marco Fluidtech UP2/E electronic gear pump. It has a maximum flow rate of 10 $dm^3\ min^{-1}$ and is voltage-controlled using a Manson HCS-3604 power supply. For low circulation flow rates, a Shenchen M6-6L peristaltic pump with a maximum flow rate of 6 $dm^3\ min^{-1}$ is used. It is controlled by directly setting the flow rate using a built-in display. Due to space restrictions, this pump has to overcome a higher head than the electronic gear pump, resulting in higher losses.

Both pumps are calibrated with regard to their head losses. The outlet of the electronic gear pump is placed at the height of the lower access point of the batch reactor, while the peristaltic pump is placed about 30 cm below, thus representing a calibration in the same conditions as during the respective experiments. The flow rate is determined by measuring the pumped volume within 5 s for a setting of 3 V, 6 V, 9 V and 12 V for the electronic gear pump, and the time needed to pump a volume of 100 cm^3 at 500 $cm^3\ min^{-1}$, 800 $cm^3\ min^{-1}$, 1600 $cm^3\ min^{-1}$, 1700 $cm^3\ min^{-1}$, 2500 $cm^3\ min^{-1}$ and 2750 $cm^3\ min^{-1}$ in case of the peristaltic pump. In the first case, triplets of each point are recorded, while each point in case of the second pump is recorded only once. The resulting curves are displayed in Figures 4.7 and 4.8.

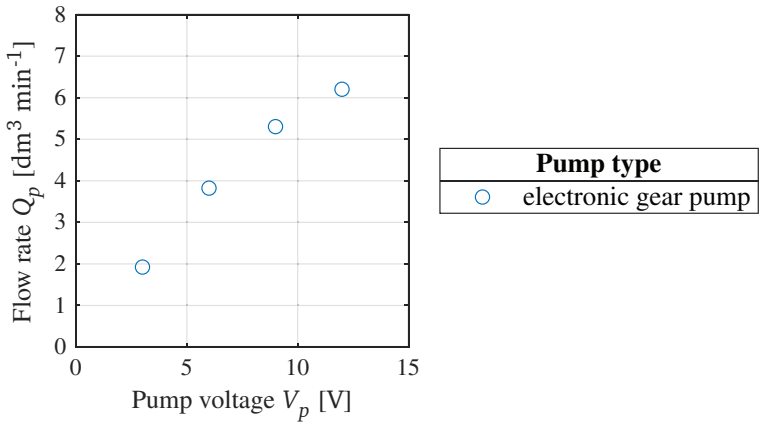

Figure 4.7: Calibration curve of the electronic gear pump used for circulating the water in the batch reactor, showing the averaged pump flow rate, Q_p, versus voltage setting, V_p. The data is available in Table A.3.

Experiments are conducted using the electronic gear pump with a flow rate of 1.92 $dm^3\ min^{-1}$, 3.82 $dm^3\ min^{-1}$ and 5.30 $dm^3\ min^{-1}$ in the countercurrent flow, i.e. the flow direction from the top to the bottom of the reactor. In the concurrent flow situation, a flow rate of 6.20 $dm^3\ min^{-1}$ is tested in addition to the aforementioned flow rates. With the peristaltic pump, flow rates of 0.5 $dm^3\ min^{-1}$, 1.0 $dm^3\ min^{-1}$ and 1.5 $dm^3\ min^{-1}$ are investigated in the countercurrent flow, while only a flow

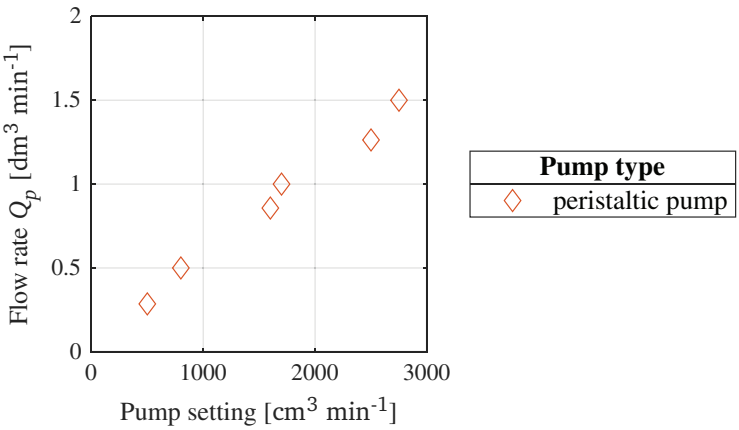

Figure 4.8: Calibration curve of the peristaltic pump used for circulating the water in the batch reactor, showing pump flow rate, Q_p, versus voltage setting, V_p. The data is available in Table A.3.

rate of 1.5 dm^3 min^{-1} is tested in the concurrent flow. During these experiments, 0.8 dm^3 of TDG supersaturated, pure water is used to compensate for the additional hose and pump volume.

The combined influence of both ultrasonication and flow circulation on the liquid-gas mass transfer is studied by using the SinapTec 20 kHz transducer. In the countercurrent flow situation, flow rates of 1.5 dm^3 min^{-1}, 1.92 dm^3 min^{-1}, 3.82 dm^3 min^{-1} and 6.20 dm^3 min^{-1} are used, respectively. For the concurrent flow, the respective flow rates of 1.5 dm^3 min^{-1}, 1.92 dm^3 min^{-1}, 3.82 dm^3 min^{-1} and 5.30 dm^3 min^{-1} are tested.

Throughout all experiments, a 10 min waiting time is used to allow the TDG sensor to adjust after filling the reactor. Then, flow circulation (and ultrasonication, where applicable) is applied for 10 min, while keeping the liquid temperature at 20 °C. Single data points are recorded.

Bubbling equipment

Gas bubbling is tested both in silent conditions, i.e. without ultrasound, and in combination with ultrasound, to see the effect on the liquid-gas mass transfer. The batch reactor was used with 0.75 dm^3 of TDG supersaturated, pure water. A variation in gas bubble sizes is achieved by using gas diffusers with different pore sizes. The first one is an oxygenation stone made of steel, with a tip diameter of 12.7 mm, a height of 25 mm, and a pore size of 0.5 µm. It is similar to the one used inside the pressure vessel described in Section 4.1.1. The second is an ace gas diffuser, which features a glass tube with glassy pores on the tip. The tip diameter is 7 mm, with a height of 10 mm. It features a pore size range of 145 µm to 174 µm.

The last diffuser used is a sealed, synthetic tube with an outer diameter of 6 mm. Along its circumference, 3 rows of 4 holes with a diameter of 2 mm are placed. An overview of the gas diffusers used during the experiments is displayed in Figure 4.9.

Figure 4.9: Gas diffusers used for air bubbling in the reactor. The pore size for the oxygenation stone, the ace gas diffuser and the synthetic tube with holes is 0.5 µm, 145 µm to 174 µm and 2 mm, respectively. The data is available in Table A.4.

In addition to the gas diffuser's pore size, gas bubble sizes are dependent on the gas flow rate. That is regulated using a Key Instruments FR2000 variable area flow meter with a gas flow rate of 1 $dm^3\ min^{-1}$ to 10 $dm^3\ min^{-1}$. The bubbling is conducted using air, which is supplied by an in-house air compression system. To reduce the pressure at the inlet of the flow meter, the pressure is regulated using the Festo MS6-RLP, which is set to 0.5 bar. The gas diffusers are placed near the wall at the bottom of the batch reactor. For both the oxygenation stone and the synthetic tube, gas flow rates of 1 $dm^3\ min^{-1}$, 4 $dm^3\ min^{-1}$, 7 $dm^3\ min^{-1}$ and 10 $dm^3\ min^{-1}$ are used. The ace gas diffuser has a limited maximum gas flow rate, due to the limited surface area. In this case, only gas flows of 1 $dm^3\ min^{-1}$ and 4 $dm^3\ min^{-1}$ are used. The combination of ultrasound and gas bubbling is tested using the SinapTec 20 kHz horn transducer at 100 % amplitude, and the oxygenation stone with a flow rate of 1 $dm^3\ min^{-1}$ and 10 $dm^3\ min^{-1}$, respectively.

Similar to the other experiments, the waiting time for sensor adjustment is 10 min, and the actual experiments are conducted for 10 min each. The temperature in the reactor is kept at 20 °C, and the data points are recorded once.

4.1.3 Summary of experimental methods

The input for the experiments is accomplished by increasing the TDG saturation level in 1.6 dm^3 of pure water. This volume is pressurized in an in-house build vessel, and gas is introduced through a gas diffuser, leading to bubbling within the liquid. Over time, this leads to an increase in TDG saturation due to the higher pressure and increased interfacial area.

The water is then used in a batch reactor to study the dependence of the liquid-gas mass transfer on operating parameters. Three different methods are investigated: ultrasonication, gas bubbling, and flow circulation. The most efficient parameters of these methods are combined to study eventual further enhancement. To determine the liquid-gas mass transfer, the TDG saturation level is monitored throughout each experiment, in addition to other parameters such as temperature and pH. In general, all experiments allow for adjustment of the TDG sensor after filling the reactor by waiting 10 min. The subsequent experiment is then conducted for 10 min at a constant temperature of 20 °C. A summary of the equipment, as well as the input, methods, and output needed for the experiments, is given in Table 4.3.

Table 4.3: Summary of experimental methods during degasification enhancement experiments, including the main equipment needed, input, applied methods, and output.

Supersaturation	
Equipment:	• Pressure vessel (custom build) • Pressure relief valve (Brewtools) • Gas diffuser (oxygenation stone) • Pressure regulator (Festo MS6-LRP) / mass flow controller (Alicat Scientific MC-Series) • Pressure transducer (GE UNIK 5000, $f = 1$ Hz)
Input:	• Pure water (Stakpure OmniaTap II)
Methods:	• Pressure increase • Aeration (gas bubbling)
Output:	• TDG supersaturated water
Degasification	
Equipment:	• Meinhardt Ultrasonics batch reactor • Cooling cycle ◦ Refrigerated bath (Neslab RTE-221)

Continued on next page

Table 4.3 – continued from previous page

	◦ Electric gear pump (Marco Fluidtech UP3/E) • Sensors ($f = 5\,\mathrm{Hz}$) ◦ TDG sensor (InWater Technologies PT4) ◦ Pressure transducer (GE UNIK 5000) ◦ pH sensor (Sensorex pH3400) ◦ Thermometer (PT100) • Ultrasound (see Table 4.1) • Flow circulation pumps ◦ Marco Fluidtech UP2/E ◦ Shenchen M6-6L • Gas diffuser ◦ Oxygenation stone ◦ Ace gas diffuser ◦ Synthetic tube
Input:	• TDG supersaturated water
Methods:	• Ultrasonication ◦ Acoustic power ◦ Frequency • Aeration (gas bubbling) ◦ Pore size ◦ Air flow rate • Turbulence (flow circulation) ◦ Direction ◦ Flow velocity
Output:	• Decrease in TDG saturation

4.1.4 Calculation of the liquid-gas mass transfer coefficient during batch reactor experiments

The liquid-gas mass transfer coefficient, $k_L a$, is determined from the measurement data of the TDG saturation during the experiments in the batch reactor. Both total gas pressure (TGP) and atmospheric pressure are measured using the aforementioned sensors. The TDG saturation level is then calculated using Equation 2.14.

As the mass transfer within the batch reactor represents a dynamic situation, the calculation of $k_L a$ cannot be accomplished by taking the difference between the initial TDG saturation and the final TDG saturation after exposure to one or multiple parameters influencing the mass transfer. Instead, the mass balance in the case of a static liquid is constructed to derive $k_L a$ from the measurement data:

$$\text{input} + \text{creation} = \text{output} + \text{loss} + \text{accumulation}. \tag{4.2}$$

In this case, the system experiences no mass input, creation, or output of mass. Using representations for both loss and accumulation of mass, Equation 4.2 changes to:

$$0 + 0 = V\, k_L a \left(S_{\text{TDG}}(t) - S^*_{\text{TDG}}\right) + V \frac{\mathrm{d}S_{\text{TDG}}(t)}{\mathrm{d}t}, \tag{4.3}$$

where S_{TDG} is the measured TDG saturation at time t, S^*_{TDG} is the baseline TDG saturation, i.e. 100 %TDG, and V is the volume of the static liquid batch. The loss term is positive under the assumption that the TDG saturation of the batch is decreased over time. Canceling the volume and rearranging leads to:

$$-k_L a \,\mathrm{d}t = \frac{\mathrm{d}S_{\text{TDG}}(t)}{S_{\text{TDG}}(t) - S^*_{\text{TDG}}}. \tag{4.4}$$

Here, we include the subtraction of the baseline TDG saturation into the derivation term:

$$-k_L a \,\mathrm{d}t = \frac{\mathrm{d}\left(S_{\text{TDG}}(t) - S^*_{\text{TDG}}\right)}{S_{\text{TDG}}(t) - S^*_{\text{TDG}}}. \tag{4.5}$$

The boundaries for this problem are known. At $t = 0$, the sensor reading is stable at the highest TDG saturation, $S_{\text{TDG},max}$. For a time $t > 0$, the TDG saturation is the measured value. Therefore, Equation 4.5 is integrated with regard to time and saturation on the left- and right-hand side, respectively:

$$\begin{aligned} -k_L a \int_0^t \mathrm{d}t &= \int_{S_{\text{TDG},max}}^{S_{\text{TDG}}(t)} \frac{\mathrm{d}\left(S_{\text{TDG}}(t) - S^*_{\text{TDG}}\right)}{S_{\text{TDG}}(t) - S^*_{\text{TDG}}}, \\ -k_L a\, t &= \ln\left(\frac{S_{\text{TDG}}(t) - S^*_{\text{TDG}}}{S_{\text{TDG},max} - S^*_{\text{TDG}}}\right). \end{aligned} \tag{4.6}$$

As apparent from this equation, the liquid-gas mass transfer coefficient is the negative slope of the logarithmic difference on the right-hand side, and depends only on the TDG saturation at time t.

TDG sensor time constant

The TDG sensor has a slow response time when exposed to large gradients, as discussed in Section 2.3.1. Therefore, a time constant, δ, is determined to compensate for the time lag. It is determined by introducing a sudden change in saturation, e.g. by putting the TDG sensor from air, i.e. 100 %TDG, into water

with a higher (or lower) TDG saturation level. The measurement data is recorded until the reading is stable. This procedure is possible to be conducted for saturation steps representing both increases and decreases. The latter is achieved by e.g. taking a sensor out of a solution with a TDG supersaturation, hence exposing it to 100 %TDG.

To calculate the sensor's time constant, the difference between the stable values before and after the saturation change, ΔS_δ is determined. The time constant is then obtained following a definition by Carr (1993):

$$\Delta S_\delta \left(1 - \exp\left(-\frac{t}{\delta}\right)\right)_{t=\delta} = 63.21\,\% \cdot \Delta S_\delta. \tag{4.7}$$

In other words, the time constant is the time the sensor needs to measure up to 63.21 % of the total step difference. A total of eight steps are investigated, with half of them showing an upward step and the other half showing a downward step. The determined time constants are averaged, resulting in a TDG sensor time constant of $\delta_{\mathrm{TDG}} = 63.8\,\mathrm{s}$.

Calculation procedure

Following the aforementioned equations, the liquid-gas mass transfer coefficient is calculated from the measured TDG saturation. To do so, the data needs to be treated prior to the liquid-gas mass transfer coefficient calculation. The initial measurement data is considered from the beginning of the change in measured TDG saturation, i.e. after the adjusting time to get stable readings from the TDG sensor at the beginning of the experiment.

First, the measurement values are rebuilt by deconvolution using the sensor time constant, δ_{TDG}. To do so, each value is recalculated as follows:

$$S'_{\mathrm{TDG}} = S_{\mathrm{TDG},0} + \Delta S_{\mathrm{TDG}} \left(1 - \exp\left(-\frac{t}{\delta}\right)\right). \tag{4.8}$$

Here, S'_{TDG} is the deconvoluted TDG saturation value, $S_{\mathrm{TDG},0}$ is the initial TDG saturation, and ΔS_{TDG} is the difference between the initial TDG saturation and the measured TDG saturation at time t. Then, the data is smoothened to remove outliers using the movmean-function in MATLAB R2022b with a sliding window of 40 elements. The resulting data points are plugged into Equation 4.6. In the final step, the linear slope of the real part of the resulting logarithmic difference values is determined using the polyfit-function in MATLAB R2022b, to determine the negative liquid-gas mass transfer coefficient, $k_L a$.

4.2 Results

To evaluate the influence of different operating parameters on the liquid-gas mass transfer coefficient, experiments are conducted within a 1 dm^3 batch reactor. The TDG saturation level is monitored, and the volumetric liquid-gas mass transfer coefficient, $k_L a$, is calculated using the method described in Section 4.1.4. Two different types of experiments are conducted. First, the differences in the mass transfer during ultrasonication of water supersaturated with air, N_2 and O_2 are studied. Then, air-supersaturated water is exposed to different operating parameters:

- transducer frequency and acoustic power,
- flow circulation within the batch reactor at multiple flow velocities, and
- gas bubbling with different bubble sizes and gas flow rates.

In addition, 20 kHz ultrasound at 100 % amplitude is combined with selected flow circulation speeds and gas bubbling, respectively. Throughout all experiments, no significant changes in the pH within the reactor are observed.

4.2.1 Variation of $k_L a$ as a function of the gas used for supersaturation in pure water

Using the methods described in Section 4.1.2, the effect of TDG supersaturation using different gas species on the liquid-gas mass transfer is studied. The resulting averaged $k_L a$ values are listed in Table 4.4. The full data obtained during experiments is displayed in Figures A.1 and A.2.

Table 4.4: $k_L a$ values during ultrasonication of pure water supersaturated with different gases, using different ultrasonic frequencies and amplitudes.

Gas type	Frequency [kHz]	Amplitude [%]	$k_L a$ [s^{-1}]
N_2	20	10	$1.52 \cdot 10^{-3}$
		100	$46.43 \cdot 10^{-3}$
	40	100	$0.68 \cdot 10^{-3}$
O_2	20	10	$1.88 \cdot 10^{-3}$
		100	$76.09 \cdot 10^{-3}$
	40	100	$1.40 \cdot 10^{-3}$
air	20	10	$1.06 \cdot 10^{-3}$
		100	$45.83 \cdot 10^{-3}$
	40	100	$0.78 \cdot 10^{-3}$

From the results, different parameters influencing the liquid-gas mass transfer are apparent. At the same transmitted acoustic power (10 % amplitude for the

SinapTec 20 kHz transducer and 100 % amplitude for the Meinhard Ultrasonics 40 kHz transducer), the $k_L a$ is in all cases lower during ultrasonication with 40 kHz. Moreover, increasing the acoustic power leads to a substantial increase in the liquid-gas mass transfer, as apparent from the values obtained from the experiments using 20 kHz at 10 % and 100 % amplitude. This is in agreement with findings by Asakura and Yasuda (2022). Yet, the difference between the $k_L a$ values obtained for the two frequencies at the same transmitted acoustic power is larger than expected, as the difference in frequency is not large. Literature concerning the influence of the ultrasonic frequency on the liquid-gas mass transfer, e.g. Asakura and Yasuda (2022) and Zhang et al. (2021), does not provide a clear delineation of the typical magnitude of variation for these differences in classical reactors. A reason for the differences occurring in the case at hand is found in the different transducer designs, which allows for a much higher power per surface area of the SinapTec horn transducer compared to the Meinhardt Ultrasonics flat transducer. This creates a more concentrated acoustic field within the liquid bulk, which increases the liquid-gas mass transfer. In addition, acoustic streaming within the liquid bulk increases, as reported by Mandroyan et al. (2009a), who see both an increase in the axial average velocity of the liquid above the transducer with an increasing transmitted power density, as well as a decrease of that velocity for increasing transducer diameters. The beneficial effects of acoustic streaming are discussed in Section 2.3.2.

Furthermore, the results show increased $k_L a$ values when having an O_2-supersaturation compared to both N_2- and air-supersaturation cases for all respective frequencies and amplitudes. Between the values obtained during sonication of N_2- and air-supersaturated water, the differences are in general not large. With regard to the discussion of gas solubility in Section 2.2.1, this is to be expected if the assumption is valid that a higher gas solubility implies a higher capability for degasification. The liquid-gas mass transfer during sonication of air-supersaturated water is expected to be higher than in the case of N_2-supersaturation, due to the occurrence of O_2 in the gas mixture. However, this is only the case during sonication using 40 kHz ultrasound. A reason for this is the better ability for mass transfer in case of O_2 in comparison with N_2 in solution.

4.2.2 Dependency on frequency and acoustic power

The three ultrasonic transducers described in Section 4.1.2 are used to evaluate the effect of the frequency and the acoustic power on the liquid-gas mass transfer. The $k_L a$ values calculated from the experiments are displayed in Figure 4.10. Several different amplitudes of the 20 kHz transducer are investigated with regard to their influence on the liquid-gas mass transfer. The trend is close to cubic, with the highest acoustic powers resulting in the highest liquid-gas mass transfer rates, reaching a mean $k_L a$ of $42.13 \cdot 10^{-3}\ s^{-1}$. This is in agreement with the findings of Asakura and Yasuda (2022), even though the peak power used here is one order of

magnitude higher. In addition, Agarkoti and Gogate (2022) state that the cavitation intensity is higher at higher acoustic powers, consequently leading to increased emergence of degasification bubbles. The development of a plateau of the $k_L a$ towards higher acoustic powers is not apparent.

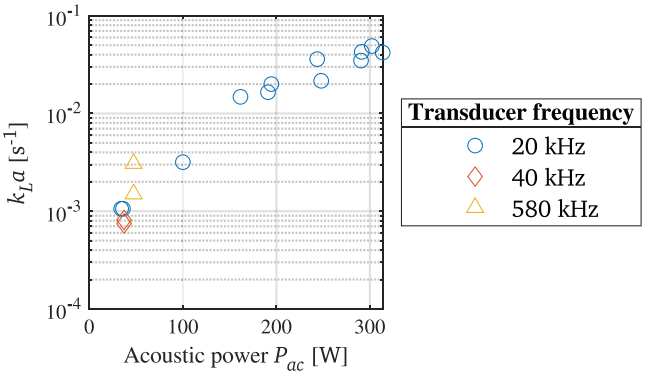

Figure 4.10: Volumetric liquid-gas mass transfer coefficient, $k_L a$, in dependence of frequency and acoustic power, P_{US}. The data is available in Table A.4.

As the different ultrasonic transducers are powered by different generators, the acoustic power transmitted to the liquid differs. To achieve comparability between them, the respective amplitude settings necessary to achieve the same transmitted acoustic power of about 37 W among the transducers are determined using the regression curves discussed in Section 4.1.2. For this setting, the liquid-gas mass transfer coefficient during ultrasonication with the respective frequency of 20 kHz, 40 kHz and 580 kHz is small in comparison to the findings for higher transmitted powers and 20 kHz. Yet, differences between the frequencies used are apparent, with the 580 kHz transducer showing the highest mean $k_L a$ values of $2.29 \cdot 10^{-3}$ s^{-1}, the 40 kHz transducers the lowest mean $k_L a$ values of $0.78 \cdot 10^{-3}$ s^{-1}, and the 20 kHz transducer lying in between with mean $k_L a$ values of $1.06 \cdot 10^{-3}$ s^{-1}. Comparing these findings with results presented by Asakura and Yasuda (2022), a general agreement in the influence of the frequency is found. As discussed in the previous section, the differences between the frequencies are small, which again is presumably due to the higher transmitted power per area of the emitting surface achieved with the 20 kHz transducer.

4.2.3 Dependency on the flow velocity

Air-supersaturated, pure water is circulated within the batch reactor. External pumps are used to create different flow velocities in both concurrent, i.e. bottom-top, and countercurrent, i.e. top-bottom, direction. From the calibrated circulation pump flow rate, Q_p, the cross-sectional flow velocity is calculated by dividing Q_p by the cross-sectional area of the batch reactor.

In Figure 4.11, the calculated $k_L a$ values are displayed over the cross-sectional flow velocity, U_{cs}. The general trend during countercurrent flow is constant, and the mean $k_L a$ is $3.09 \cdot 10^{-3}$ s^{-1}. The values for the highest velocity during concurrent flow are larger in comparison to the other values, which, with a mean $k_L a$ value of $1.50 \cdot 10^{-3}$ s^{-1}, show a rather constant trend as well[15]. The mean $k_L a$ values for countercurrent flow are thus twice as high in comparison to the ones in countercurrent flow (except the aforementioned outlier). Comparing the results to the volumetric liquid-gas mass transfer values obtained for natural degasification, which have been discussed in Section 3.3, shows that values one order of magnitude higher are obtained in the batch reactor. The results are furthermore in good agreement with the values described by literature for optimized mass-transfer experiments, as discussed in the aforementioned section.

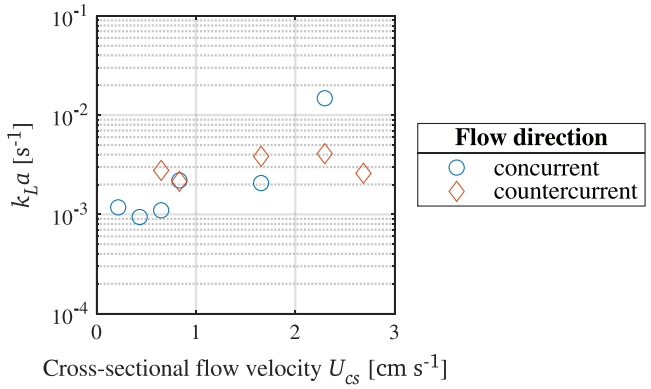

Figure 4.11: Volumetric liquid-gas mass transfer coefficient, $k_L a$, in dependence of cross-sectional flow velocity, U_{cs}, in the reactor. The data is available in Table A.5.

The reason for the outlier is found to be the experimental setup, which induces low pressures at high velocities during concurrent flow, as the water is pumped from a higher elevation than the pump placed at the lower access point of the batch reactor. Thus, natural degasification takes place within the pump, leading to drastically increased liquid-gas mass transfer and subsequently a dramatic overestimation of the $k_L a$ values within the reactor. The difference between concurrent and countercurrent flow is explained by the increased residence time of gas bubbles within the liquid batch, as the water has a flow in the opposite direction of the bubbles rising to the surface due to buoyancy.

4.2.4 Dependency on gas bubbling

The effect of gas bubbling on the liquids-gas mass transfer coefficient is investigated using different gas diffusers to introduce gas bubbles of different sizes in the

[15]Including the outlier leads to a mean $k_L a$ value of $3.71 \cdot 10^{-3}$ s^{-1} for the concurrent flow case.

batch reactor. Three gas diffusers with different pore sizes are available, and the gas flow rate is adjusted. Air is used for the bubbling during the experiments.

Data points from the calculated $k_L a$ values during the use of the three gas diffusers over the air flow rate, Q_a, are displayed in Figure 4.12. Here, the pore sizes 0.5 µm, 145 µm to 174 µm, and 2 mm represent the gas diffusers oxygenation stone, ace gas diffuser, and synthetic tube, respectively. The $k_L a$ values at an air flow rate of 3 $dm^3\ min^{-1}$ are $10.17 \cdot 10^{-3}\ s^{-1}$, $7.03 \cdot 10^{-3}\ s^{-1}$ and $4.75 \cdot 10^{-3}\ s^{-1}$ in the respective case of the oxygenation stone, ace gas diffuser and synthetic tube. At the highest air flow rate of 10 $dm^3\ min^{-1}$, the $k_L a$ values for the oxygenation stone and the synthetic tube are $12.62 \cdot 10^{-3}\ s^{-1}$ and $9.01 \cdot 10^{-3}\ s^{-1}$, respectively. Following this, a general trend towards higher liquid-gas mass transfer when reducing the pore size is apparent.

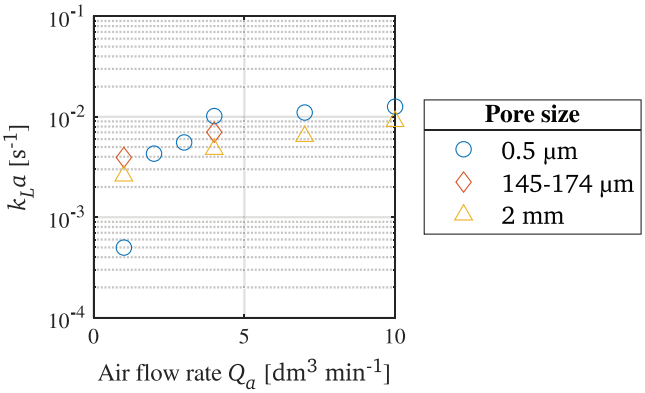

Figure 4.12: Volumetric liquid-gas mass transfer coefficient, $k_L a$, in dependence of gas diffuser pore size and air flow rate, Q_a, in the reactor. The data is available in Table A.6.

One outlier is found for the lowest flow velocity and the oxygenation stone, which shows a $k_L a$ value of one order of magnitude lower than the other two gas diffusers. This is due to the emergence of very few, large bubbles at these settings, presumably occurring due to preferred channels to the surface area of the gas diffuser, resulting in fewer, but larger air bubbles. In addition, a trend towards higher $k_L a$ values at higher velocities is found, and a plateau emerges at the highest velocities. The results are in agreement with the literature, which reports increases in the mass transfer in dependence of the bubble size and numbers. Decreasing the bubble size while increasing the number of bubbles leads to higher mass transfer rates due to the increased interfacial area (Motarjemi and Jameson, 1978; Wang et al., 2020). Moreover, a higher gas flow rate leads to both increased mixing and changes in the bubble sizes as well, thus leading to increased mass transfer.

4.2.5 Combination of parameters

For selected operating points, gas bubbling and flow circulation are separately combined with sonication of the liquid batch using 20 kHz ultrasound at 100 % amplitude. In case of gas bubbling, the oxygenation stone with a pore size of 0.5 µm at gas flow rates of 1 $dm^3\ min^{-1}$ and 10 $dm^3\ min^{-1}$ is used. For the flow circulation within the reactor, both concurrent and countercurrent flows with several flow velocities are combined with the sonication. The data obtained for all cases shows constant trends, independent of air flow rate in case of bubbling or flow velocity in case of the circulation flow[16]. Therefore, all results are plotted together in a boxplot to allow comparison between them. In addition, the maximum values obtained during the experiments of the respective operating parameter alone are displayed for comparing the effect of sonication. The plot is displayed in Figure 4.13.

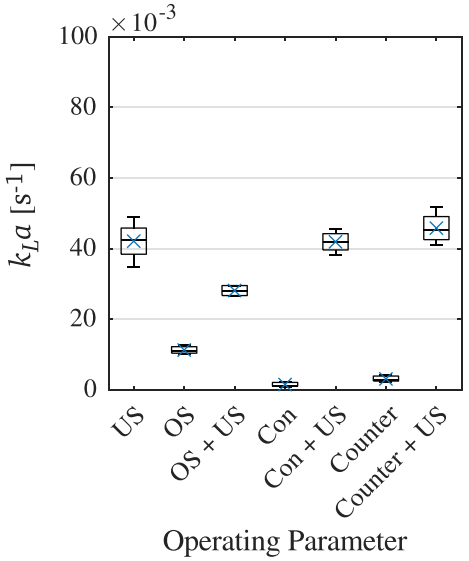

Figure 4.13: Boxplot of the resulting k_La values obtained from operating parameters alone and in combination with sonication using 20 kHz ultrasound at 100 % amplitude. "US" is sonication, "OS" is bubbling using the oxygenation stone, while "Con" and "Counter" are the con- and countercurrent flow within the batch reactor, respectively. Boxes showing the interquartile range including median. Top and bottom line showing maximum and minimum. Mean values indicated by ×. The data is available in Table A.7.

The highest overall volumetric liquid-gas mass transfer values in dependence of single operating parameters are found for sonication of the batch with 20 kHz ultrasound at an acoustic power of about 300 kW, leading to high k_La values with a

[16]The data obtained during the experiments is displayed in Figures A.3 and A.4.

mean of $42.13 \cdot 10^{-3}\ s^{-1}$. In general, a combination of sonication with any of the selected operating parameters is beneficial in a great manner. This is apparent from a large increase in the values of the volumetric liquid-gas mass transfer coefficient in comparison to the $k_L a$ values obtained during bubbling or introduction of flow. Yet, combined sonication and bubbling using the oxygenation stone leads to a decrease in the mass transfer compared to pure sonication, achieving mean $k_L a$ values of $28.13 \cdot 10^{-3}\ s^{-1}$. When sonication is combined with flow circulation, the mean $k_L a$ values are $41.94 \cdot 10^{-3}\ s^{-1}$ and $45.82 \cdot 10^{-3}\ s^{-1}$ in case of con- and countercurrent flow, respectively. Seeing this, countercurrent flow is the only option leading to an increase in the liquid-gas mass transfer, even though by only 8.76 % in comparison to sonication alone.

Literature reports on the phenomena taking place during introduction of a flow perpendicular to the ultrasonic field. While the acoustic waves are not influenced, the velocity field representing acoustic streaming above the transducer is largely deflected (Barthès et al., 2015; Mazue et al., 2015). This has a direct implication on the evolution of bubbles within the batch reactor, as the setup with the pump access point at the bottom of the reactor (in- or outlet, depending on the direction of the flow circulation) leads to such a perpendicular flow. Yet, the overall flow direction is assumed to be parallel to the radiation axis of the transducer.

4.3 Discussion

The data obtained from experiments on the liquid-gas mass transfer coefficient is used to evaluate the scalability of the process. The overall highest liquid-gas mass transfer coefficients for a single parameter during degasification of a batch are apparent during ultrasonication using 20 kHz ultrasound with a high acoustic power of about 300 kW. It cannot be ruled out that even higher values are possible with higher frequencies at the same acoustic power, but due to limitations of the equipment, this is not verified. On the other hand, higher frequencies will lead to an increase in the number of unstable acoustic cavitation taking place within the sonicated volume, thus possibly creating unwanted chemical reactions. The design of the three transducers influences the results as well, as the power per area of the emitting surfaces is not equal. Moreover, the different frequencies of the transducers influence their respective thicknesses, which in turn has consequences for their operational capability, e.g. heating problems. A comparison with results presented by Asakura and Yasuda, 2022 still shows good agreement with the general trends obtained during the experiments.

Having a circulation flow of the liquid within the batch reactor leads to an increase in the liquid-gas mass transfer as well, even though it is one order of magnitude smaller than the high values obtained with high-power ultrasound. In general, a flow in opposite direction of the acoustic wave propagation and the direction of

the bubble's buoyancy forces, i.e. a countercurrent flow, is more beneficial to the liquid-gas mass transfer than a flow in a concurrent direction. A better experimental design leading to avoidance of natural degasification during pumping of the water will be beneficial with regard to the results of concurrent flow at high flow rates.

The introduction of gas bubbles into the liquid batch also increases the liquid-gas mass transfer. Here, a plateau toward higher gas flow rates is apparent. The pore size is the critical parameter, with smaller pores leading to the creation of more bubbles with a smaller diameter, i.e. an increased interfacial area. Still, the $k_L a$ values are only one-quarter of the ones obtained using high-power ultrasound.

The question at hand is what a combination of those operating parameters leads to. Taking the parameter with the highest overall $k_L a$ values achieved, i.e. high-power sonication using 20 kHz ultrasound, a combination with air bubbling and flow circulation, respectively, is tested. The outcome shows that air bubbling leads during sonication to a drastic decrease in $k_L a$ values. A reason for this is the disrupted creation of degasification bubbles, as all bubble nuclei are taken away from the liquid due to coalescence with larger bubbles introduced into the liquid. Furthermore, the acoustic field within the batch reactor is rather small in comparison to the number of bubbles introduced by the gas diffuser. A larger liquid batch and acoustic field at the same acoustic power can lead to different results. Nevertheless, the values obtained are comparable to results reported by Sajjadi et al. (2017), who studied the liquid-gas mass transfer due to acoustic stirring in an aerated reactor.

In comparison to gas bubbling, a concurrent flow has a negligible effect on the liquid-gas mass transfer during sonication, while a countercurrent flow leads to an increase in $k_L a$ when combined with sonication. As discussed earlier, this is due to an increase in the residence time of gas bubbles both within the liquid batch and the acoustic field. Even though the effect is small, this is the only combination of the parameters under consideration leading to an increase in the liquid-gas mass transfer in comparison to pure sonication using high-power ultrasound.

A flaw of the experimental setup is the size of the TDG sensor in comparison to the reactor. As the measurement of the TDG saturation level has to be conducted in situ, it has to be placed within the liquid inside the reactor, as displayed in Figure 4.14. This leads to a reduction of the treated liquid volume of about 25 %. In addition, the sensor body leads a blockage of the flow within the reactor, thus having an effect on the ultrasonic streaming, gas bubbling, and flow circulation. As all the methods in question are affected in a similar way, the comparability of the results is nevertheless given.

To have a tool at hand that allows for the prediction of the volumetric liquid-gas mass transfer coefficient, a model is developed. It is built as an empirical model, using data from both acoustic power and flow velocity dependencies of $k_L a$. In addition, the sonicated volume, V, is included. The bubbling effect is not taken

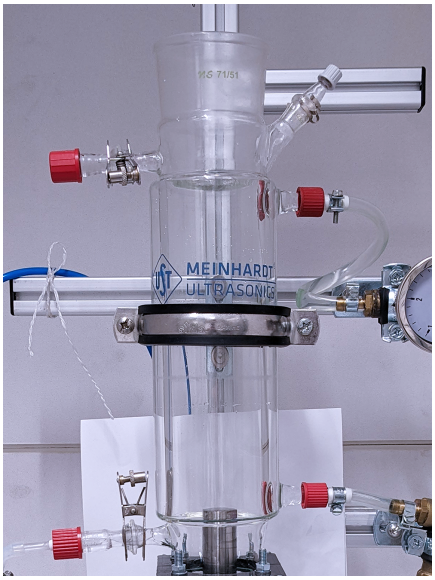

(a) Meinhardt Ultrasonics reactor without water and sensors.

(b) Meinhardt Ultrasonics reactor with water and the TDG sensor.

Figure 4.14: The Meinhardt Ultrasonics glass reactor without and with the TDG sensor used to measure the TDG saturation during parameter tests. During the experiments, only the cooled section of the reactor is filled.

into account, as the results do not show benefits of combining gas bubbling with ultrasound in this case. As a general start, these parameters are developed as follows:

$$\begin{aligned}(k_L a)_{\text{mdl}} &= f\,(P_{ac}, U_{cs}) \\ &= A_{\text{mdl}}\, P_{ac}^{\alpha}\, U_{cs}^{\beta},\end{aligned} \tag{4.9}$$

where $k_L a_m$ describes the modeled volumetric liquid-gas mass transfer coefficient, A_{mdl} is a general constant within the model, and α and β describe the influence of the acoustic power, P_{ac} (in [W dm^{-3}]), and the cross-sectional flow velocity, U_{cs} (in [cm s^{-1}]), respectively. A power law is derived using the fit-function in MATLAB R2022a to capture the trend of the $k_L a$ measurement data from the SinpaTec 20 kHz transducer in dependence of the acoustic power:

$$(k_L a)_{\text{mdl}}\,(P_{ac}) = 9.87 \cdot 10^{-7}\, P_{ac}^{1.87}. \tag{4.10}$$

A plot of the measurement data and the fitted curve is displayed in Figure 4.15.

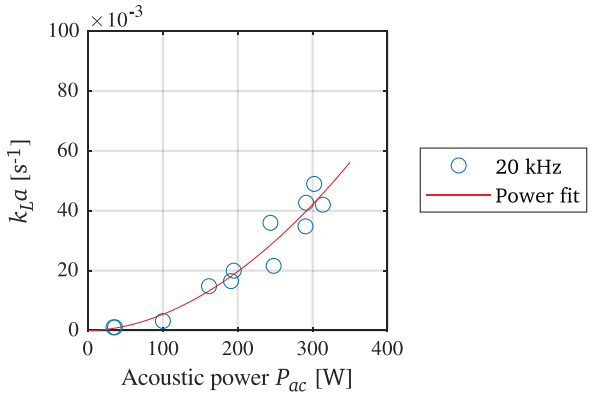

Figure 4.15: $k_L a$ values obtained from measurements using 20 kHz ultrasound at different acoustic powers, P_{ac}, to sonicate a batch of TDG supersaturated water, including a power fit curve.

To have the possibility to include the volume of the liquid bulk under sonication, the power is divided by the batch volume. This is equivalent to a compression of the fit, and is expressed by a change in A_{mdl}:

$$(k_L a)_{\mathrm{mdl}}(P_{ac}, V) = 5.77 \cdot 10^{-7} \left(\frac{P_{ac}}{V}\right)^{1.87}. \tag{4.11}$$

Now, β is matched to the results obtained during the combination of sonication and flow circulation within the batch. Only the results for countercurrent flow are taken into account, as those show an increase in the liquid-gas mass transfer coefficient. The cross-sectional flow velocities with their respective acoustic powers and $k_L a$ values are used to calculate mean β values. The resulting model is then:

$$(k_L a)_{\mathrm{mdl}} = 5.77 \cdot 10^{-7} \left(\frac{P_{ac}}{V}\right)^{1.87} U_{cs}^{0.03}. \tag{4.12}$$

Curves created using this model for four arbitrary acoustic powers are displayed in Figures 4.16 and 4.17. From these, the small influence of the flow velocity in comparison to the acoustic power per volume is apparent, as even several orders of magnitude do not change the $k_L a$ too much.

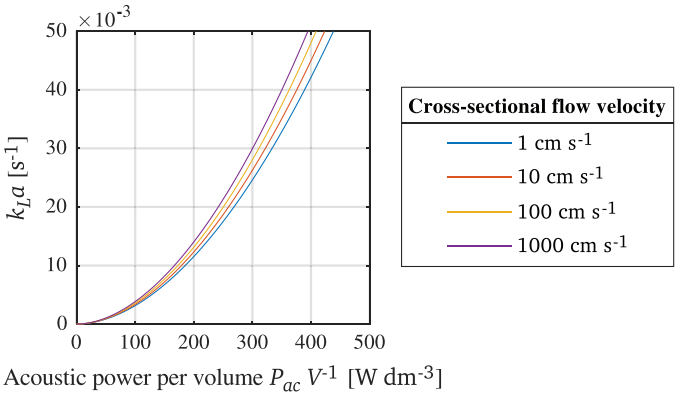

Figure 4.16: Curves obtained from the $k_L a$ model, showing the resulting $k_L a$ values for four acoustic powers, P_{ac}, over the cross-sectional flow velocity, U_{cs}.

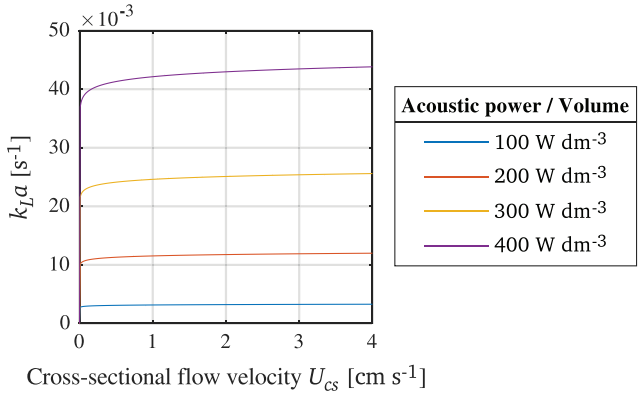

Figure 4.17: Curves obtained from the $k_L a$ model, showing the resulting $k_L a$ values for four cross-sectional flow velocities, U_{cs}, over the acoustic power per volume, $P_{ac}\,V^{-1}$.

4.4 Conclusion

The effect of different operating parameters on the liquid-gas mass transfer has been studied, both with regard to their respective influence and in combination of selected parameters. Experiments are conducted in a batch reactor filled with TDG supersaturated water. The acoustic power of the ultrasonic transducer is determined as the primary parameter to increase the liquid-gas mass transfer, resulting in the highest $k_L a$ values at high power. Sonication proves to be beneficial when combined with each of the respective selected operating parameters. Yet, only in case of countercurrent flow, a further, but small increase in the mass transfer compared to sonication alone is apparent. In comparison to the volumetric liquid-

gas transfer values determined from measurement data in the Otra river, as discussed in Section 3.3, a clear improvement of the mass transfer is found in the laboratory setting. While the introduction of a flow circulation within the reactor yields values of one order of magnitude higher than in the river, which are comparable to similar mass transfer studies found in literature, both gas bubbling and sonication raise the $k_L a$ by two orders of magnitude. Therefore, power ultrasound can be regarded as a superior tool for liquid-gas mass transfer in case of TDG supersaturation.

The results are used to create an empirical model for $k_L a$. This is a key point towards designing a solution to TDG supersaturation generated by hydropower plants, as it can serve as a starting point for scale-up studies and the design of a prototype. Nevertheless, this model creates a need for further data to increase its accuracy, as well as calibration in both experimental and natural conditions. An attempt on the experimental calibration is made on a larger experimental setup, as will be described in Chapter 5.

CHAPTER

FIVE

Testing ultrasonic degasification in medium-sized laboratory scale

The mitigation of total dissolved gas (TDG) supersaturation generated by hydropower is possible by technical methods. This requires knowledge of the degasification efficiency of different methods in situations similar to the natural case, as well as an idea of scale-up developments. The influence of operating parameters on the liquid-gas mass transfer during degasification of TDG supersaturated water has been presented in Chapter 4. Following the results, the most promising method of ultrasonic degasification is chosen to be studied further. A medium-sized test rig is designed and constructed to enable liquid-gas mass transfer studies of TDG supersaturated, flowing water, as well as scaling effects from the batch reactor. In addition, the test rig gives the opportunity to test further parameters and methods influencing the degasification process. In comparison to the batch reactor, it provides a simplified, initial idea of the processes and challenges that a degasification application in natural river faces. The design of the test rig and the procedures to create sufficiently large volumes of water with a TDG supersaturation using an in-house pressure system are explained. The results are discussed, and the $k_L a$ model derived in the previous chapter is evaluated for this setup.

5.1 Methods

Following the same procedure as developed in the case of experiments within the batch reactor (Chapter 4), the experimental process consists of 3 steps:

1. the TDG supersaturation of water,
2. the transfer to the test rig with limited losses, and
3. the degasification within the test rig.

This procedure is simplified in a schematic displayed in Figure 5.1. Since the size of the attempted experiments requires large volumes of water, the in-house facilities of the Waterpower Laboratory at NTNU are used for the entire campaign. The TDG saturation level is monitored throughout the experiments, and the measured data is used to determine the volumetric liquid-gas mass transfer coefficient, $k_L a$. A detailed description of the different parts of the experimental setup is presented in this section, along with the $k_L a$ calculation procedure.

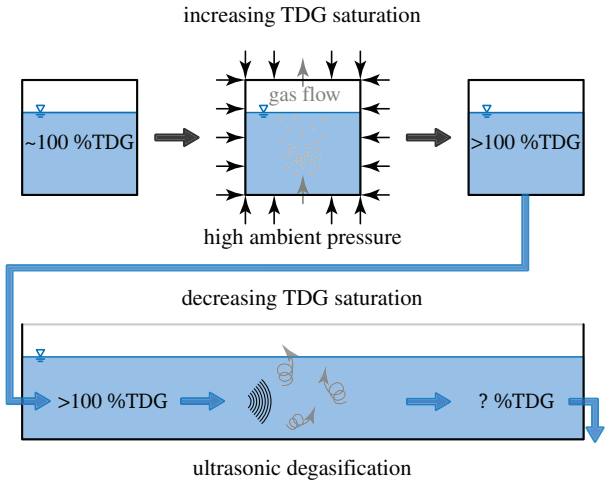

Figure 5.1: Schematic of the experimental procedure during degasification tests in the medium-sized test rig. The experimental steps are described in detail in Sections 5.1.1, 5.1.2, and 5.1.3.

5.1.1 TDG supersaturation of water

Remembering the background discussion in Section 2.2.1, the concentration or saturation level of a liquid depends primarily on the ambient pressure of the system (see also Figure 2.5). As the time to achieve a TDG supersaturation in a liquid is intended to be as small as possible, the liquid-gas mass transfer during the supersaturation process cannot rely on increased pressure only, but has to be increased further by other means. This is achieved by providing a larger liquid-gas interfacial area through introduction of gas bubbles into a pressurized system.

At the Waterpower Laboratory, a pressure vessel in form of a pressure tank with a total volume of 18 m^3 is available. It is used to pressurize 15 m^3 of water to 2 bar ambient pressure (measured at the top of the tank). The water is stored in-house in a 450 m^3 reservoir, and pumped into the pressure tank by a KSB RDLO axially split volute casing pump. A schematic of the pressure tank is displayed in Figure 5.2, and a computer-aided design (CAD) drawing of the system in Figure 5.3.

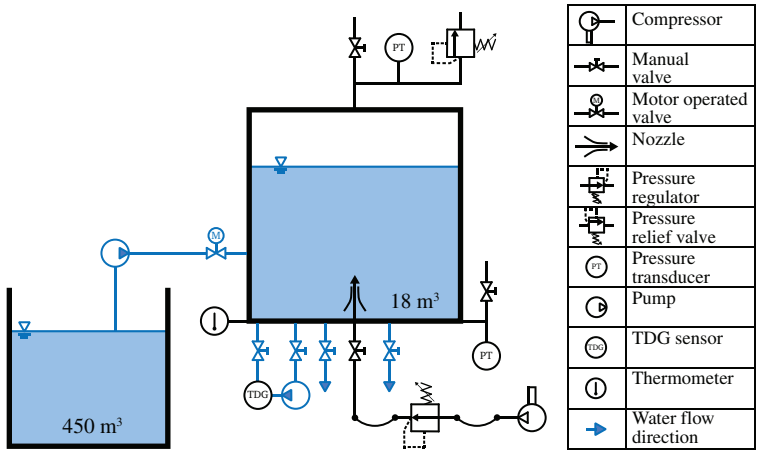

Figure 5.2: Schematic of the pressure tank in the Waterpower Laboratory at NTNU.

The pressure is monitored by a SITRANS P Z series and a GE PTX 610 pressure sensor, each with a range of 0 bar absolute to 10 bar absolute, which are installed at the top and the bottom of the tank, respectively. A GE P3223-1 hydraulic deadweight tester is used for the in-house calibration of both sensors. The temperature of the water is measured using a PT100 thermometer, while an InWaterTech PT4 TDG sensor monitors the TDG saturation level at the bottom of the tank. This sensor is calibrated using a pressure chamber, as described in Section 4.1.1. To achieve sufficient mixing of the water around the TDG sensor, a Grundfos TP 40-50/2 circulation pump is used to flush water past it. At the same time, it assures mixing of the entire water body, thus leading to a uniform distribution of the TDG saturation level within the tank. NI DAQ modules and NI LabVIEW are utilized for the data acquisition, using a sampling frequency of 1 Hz. From the resulting TDG saturation values, the slope is calculated using the polyfit-function in MATLAB R2022a.

Gas bubbles are introduced into the pressurized system using air supplied by an in-house compression system. It is regulated to a desired over-pressure using a Festo MS4-LR pressure regulator with a pressure range of 0.3 bar to 7 bar. To increase the number of bubbles while decreasing their size, an oxygenation stone is used as a gas diffuser. It is placed at the bottom of the pressure tank on a 30 cm extension pipe reaching into the pressure tank. The placement is chosen to avoid air bubble intrusion into the circulation pump loop. An adjustable Brewtools pressure relief valve with a pressure range of 0.2 bar to 2.2 bar is placed on top of the pressure tank. By this, a constant air flow through the system is achieved, while maintaining the ambient pressure.

The operating procedure is as follows: the pressure tank is separated from the hydraulic system of the Waterpower Laboratory, except for the pipes leading

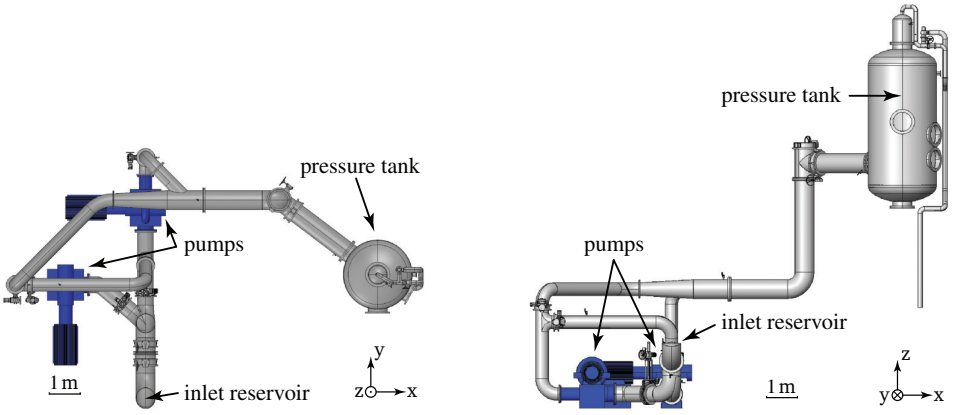

(a) Top view of the pressure tank, pumps, and pipes.

(b) Side view of the pressure tank, pumps, and pipes.

Figure 5.3: CAD drawing of the pressure tank, pumps, and piping system in the Waterpower Laboratory at NTNU.

through the pumps to the reservoir. A bleed valve on top is kept open to allow air to slip out during the filling. The pump is used at a rotational speed of 330 rpm to fill the pressure tank to a required level of about 80 %, leaving a head space filled with air. Afterwards, the bleed valve is closed, and the pump's rotational speed is further increased to 670 rpm to achieve the desired ambient pressure. Once reached, the pressure tank is isolated from the pump by closing a motor-operated valve, and the pump is shut down after gradually decreasing the rotational speed to avoid pressure surges. Now, air is flushed into the water at the bottom of the tank, at a pressure set using the pressure regulator. This pressure is required to be higher than the sum of ambient and hydrostatic pressure at the bottom of the tank, which is about 2.5 bar.

The system is left for at least 2 h to allow for sufficient dissolution of air in the water, with longer times resulting in higher TDG saturation values. After this, the gas bubbling is stopped, and the pressure is relieved gradually by opening the bleed valve. The resulting volume of TDG supersaturated water keeps its saturation level, as the only way of degasification is through the water surface, which is small in comparison to the volume. Yet, over time, a saturation gradient develops, which is why the subsequent degasification experiments are initiated immediately after the supersaturation process.

A study is conducted to evaluate the optimal combination of air overpressure and system pressure to achieve a high TDG saturation increase over time. In total, three different system pressures within the pressure tank are tested (with the pressure increase being measured at the top). First, the gas diffusion into the water is tested at atmospheric pressure, followed by a pressure increase of 1 bar and 2 bar,

respectively. The introduction of air bubbles through the gas diffuser is tested for each system pressure at 0.5 bar, 1.0 bar, 1.5 bar and 2.0 bar air overpressure[17], respectively. The TDG saturation level is monitored using the TDG sensor installed at the bottom of the pressure tank, as displayed in Figure 5.2. Air bubbling is conducted for 2 h per measurement point, and the slope of the resulting increase in TDG saturation is determined. For the atmospheric pressure and the 2 bar overpressure case, single data points are recorded, while the data for the 1 bar overpressure case is recorded twice. For the optimal parameter combination, more data points are available due to the subsequent measurements during regular experiments in the degasification test rig.

5.1.2 Water transfer

Having the large volume of water available for degasification experiments, the question of the water transfer to the test rig is at hand. Requirements are both a controlled inflow into the test rig and a minimized loss of gas due to natural degasification. Two pressure hoses are installed between valves at the bottom of the pressure tank and the inlet of the test rig. As the hydrostatic pressure from the water column drops to the ambient pressure during the release, a pressure step is created. This poses the threat of increased degasification.

A solution is found in friction losses of the hoses, which are smoothening the pressure drop over the length of the hoses. Following the Darcy-Weisbach equation, the pressure loss Δp per unit length L is dependent on the fluid density, ρ, the hose diameter, D, the mean flow velocity, v, and the Darcy friction factor, f_D (Schade et al., 2013):

$$\frac{\Delta p}{L} = f_\mathrm{D} \frac{\rho\, v^2}{2D}. \tag{5.1}$$

The velocity in the hose is determined using Bernoulli's equation between the water surface in the pressure tank and the hose at the outlet, i.e. the bottom of the pressure tank. Incompressibility of water is assumed, as well as a constant flow rate of $Q = 4\,\mathrm{dm^3\,s^{-1}}$. The Darcy friction factor is approximated using the Haaland equation (Massey, 1989):

$$\frac{1}{\sqrt{f_\mathrm{D}}} = -1.8 \log\left(\left(\frac{\frac{\varepsilon}{D}}{3.7}\right)^{1.11} + \frac{6.9}{\mathrm{Re}}\right), \tag{5.2}$$

where ε is the surface roughness and Re is the Reynolds number of the flow. The surface roughness of the hose material, EPDM, is 0.23 µm (Adam et al., 2019). The aforementioned equations allow for an estimation of a required hose length to

[17]The overpressure denotes the pressure difference to the system pressure at the bottom of the pressure tank.

smoothen out the pressure step resulting from the hydrostatic pressure at the bottom of the pressure tank, which is about 0.5 bar. With a hose diameter of 32 mm, the minimum length is 7.35 m. To compensate for uncertainties of the calculation, a safety factor of 2 is chosen, resulting in a total length of 15 m for each of the hoses.

5.1.3 The degasification test rig

The test rig for medium-scale degasification experiments has to fulfill several requirements:

1. the flow conditions need to be both monitored and controllable to achieve reliable and reproducible results,
2. the test rig needs to be adjustable to different degasification apparatus, and
3. access for sensors as well as visual access to the water flow is favorable to allow for visual measurements.

Its design is not intended to provide the possibility of studying a prototype, but to collect data in a setting (e.g. geometry or size) closer to the real-world situation at a hydropower plant. The test rig shall furthermore allow for measurements of efficiencies of various parameters influencing the liquid-gas mass transfer, as well as testing of different degasification methods. The final design consists of an open channel (or flume) with a length of 17.8 m and a cross-section of 300 mm by 400 mm. Its inlet is modular and is made up of two diffusers which are separated by a flow straightener. In addition, it gives the possibility to house a degasification application in an extra housing. The maximum length of the inlet is 2.42 m. A drawing of the degasification test rig is provided in Figure 5.4.

The channel enables the placement of degasification devices at multiple positions, e.g. in between the two diffusers or at any point within the channel. At the outlet of the channel, a V-notch weir with a maximum height of 360 mm is placed. In connection with a Vega Vegabar 14 pressure sensor with a measurement range of 0.0 bar to 0.1 bar, calibrated in-house using the GE P3223-1 hydraulic deadweight tester, the weir design is utilized to measure the volumetric flow rate in the channel, following ISO (2017). The design of the V-notch weir allows for a maximum flow rate of 4.5 $dm^3\ s^{-1}$ (Rognerud et al., 2020), and the whole test rig has a total volume of 1.98 m^3.

InWaterTech PT4 TDG sensors are placed within the first diffuser (close to the hose connection), at the channel inlet and at 4.25 m, 9.25 m, and 14.25 m downstream the channel inlet. They continuously monitor the TDG saturation level within the channel during the experiments. All sensors are calibrated using a pressure chamber, as described by Pleizier et al. (2021a). In contrast to the sensor used within the batch reactor (see Chapter 4), these sensors are equipped with a built-in atmospheric pressure sensor, thus directly giving the TDG saturation as output. All sensors are connected to NI DAQ modules, and the data is recorded using a state

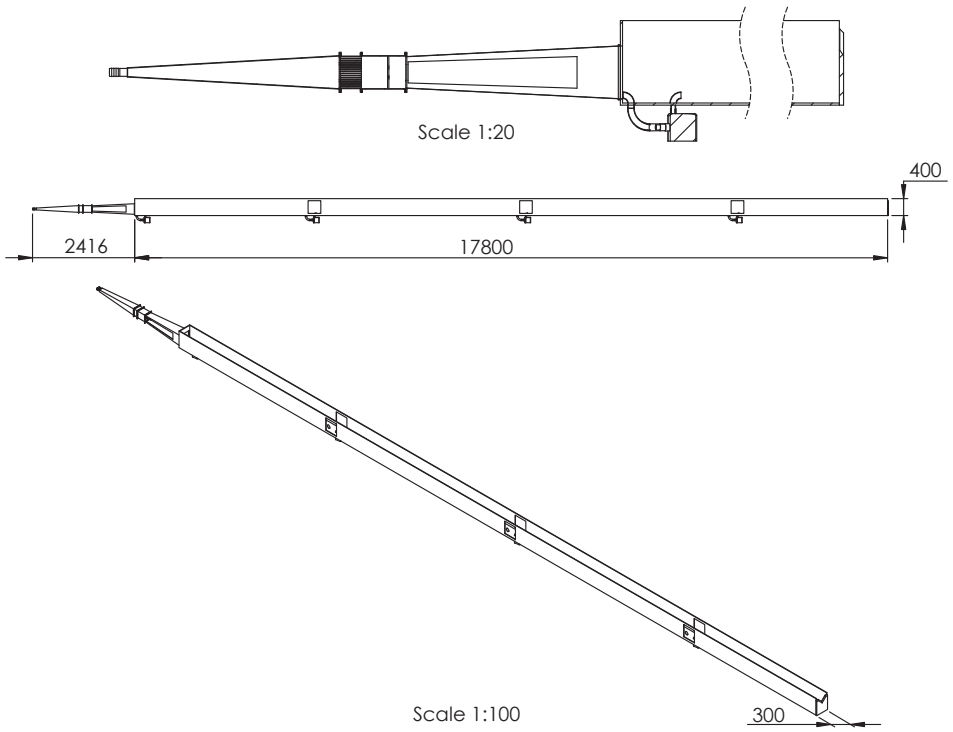

Figure 5.4: Drawing of the degasification test rig at the Waterpower Laboratory at NTNU. Detailed view of the modular inlet featuring two diffusers separated by a flow straightener and an application housing (top), side view (center), and isometric view of the full test rig (bottom). The flow direction is from left to right. The values are in mm.

machine made with NI LabVIEW. The sampling frequency used throughout the experiments is 1 Hz.

Visual access is granted from the top by the open design of the channel. In addition, sideways visual access is provided by three pairs of plexiglass windows, which are installed on both sides of the channel at the positions where the three TDG sensors furthest downstream are placed. Another pair of opposite plexiglass windows is placed within the second diffuser in the inlet section, downstream the flow straightener. They allow for observations of the degasification mechanism in case of placement of a degasification application within the inlet section.

Flushing the channel using the 15 m^3 of TDG supersaturated water from the pressure tank results in a maximum flow velocity of 4.17 $cm\,s^{-1}$ within the channel due to the V-notch weir. Due to the small water depth, i.e. small hydrostatic pressure, and the slow water current, a problem arises from gas bubbles forming up on

surfaces due to natural degasification (as discussed in Section 2.1.4). Once gas bubbles form up on the TDG sensor's silastic tubing, the readings become corrupted, as the sensor "sees" only the TGP of the gas bubble, i.e. 100 %TDG. As a result, a decrease in the TDG saturation measured from the TDG sensors during flushing with water at a constant TDG supersaturation level is observed. This is prevented by the implementation of a timed, local acceleration of the water over the sensors. Eheim compactON 5000 pumps are installed underneath the channel, having their inlet at the channel bottom, shortly upstream the respective sensor position, and the outlet right in front of them. The inlet and the outlet of the pumps are 100 mm apart, thus ensuring the same TDG saturation level of the water being flushed over the sensors. The method sufficiently flushes away all bubbles attached to the TDG sensor's cartridge, leading to stable sensor readings in case of constant TDG saturation[18]. All pumps are turned on synchronously for 2 s every 120 s using a digitally controlled power switch and a NI LabVIEW program.

The experimental procedure starts with flushing the channel with TDG supersaturated water from the pressure tank. Due to the volume of the channel and the low volumetric flow rate, the time to flush the entire channel is about 8 min. In addition, the slow response time of the TDG sensors (as discussed in Section 2.3.1) leads to a waiting time of 20 min before starting the degasification process. Again, the low volumetric flow rate in the channel and the slow sensor response time create the need for a sufficiently long degasification time, to allow for stable readings of the TDG sensors downstream the degasification application. The degasification process is therefore set to be active for 20 min. Afterwards, the procedure is repeated until the water storage is depleted.

As the emptying of the pressure tank leads to a decrease in the hydrostatic head, the flow velocity in the channel will decrease as well. This is used to evaluate the degasification efficiency in dependence of the flow. The average flow velocity during the degasification period is taken as a reference value. An additional way of influencing the flow velocity is the use of only one of the two hoses connecting the pressure tank with the channel, as the higher velocities will lead to larger pressure losses. This method is not used, as it also leads to a higher pressure step due to the decreased outflow area, thus presumably leading to more hydrodynamic degasification during the water transfer.

The only degasification method studied is ultrasonic degasification, as the results from Chapter 4 indicate that this process has the best efficiency. A SinapTec ultrasonic rod transducer with a frequency of 20 kHz and a maximum power of 1.20 kW_{RMS} (about 1.7 kW) is used. The transducer is displayed in Figure 5.5. It is driven by a SinapTec INSIDE generator with a maximum output power of

[18]Additional vibration of the TDG sensors by piezoelectric patches to shake off attached bubbles was implemented, but did not result in sufficient bubble removal.

6 kW, which is controlled using the NexTgen software, thus allowing for direct feedback on operating parameters of the transducer. The rod is 60 cm long and radiates the acoustic waves in radial direction, thus creating a cylindrical acoustic field. Placing the transducer in the center of the flow results in a maximum volume of water passing through this field, i.e. being exposed to ultrasonic degasification. The transducer is operated in continuous power mode by setting a constant power as a percentage of the maximum amplitude. The software feedback allows for an evaluation of the actual power being transferred from the generator to the transducer. It is determined by taking the average power during the sonication period. Due to the size of the transducer, an acoustic power determination, e.g. by the calorimetric method, is not possible. Therefore, the acoustic power is assumed to be equal to the transferred power given by the feedback, or, in other words, that the transducer has an efficiency of 100 %.

Figure 5.5: SinpaTec 20 kHz rod transducer used during degasification experiments in the medium-sized test rig (seen from the top), installed in the first section of the channel.

Two different positions are available for the transducer placement: in front of the second inlet diffuser (expanding into it), or in the center of the first section, i.e. between the channel inlet and the first window. At the second-mentioned

position, the ultrasonic degasification efficiency is tested in dependence of the transducer's amplitude for three different values (50 %, 75 % and 100 %), as well as in dependence of the flow velocity, where the average values are 1.5 $dm^3\ s^{-1}$, 2.5 $dm^3\ s^{-1}$ and 3.5 $dm^3\ s^{-1}$ (the combination of 1.5 $dm^3\ s^{-1}$ flow rate and 50 % amplitude is not tested). The three amplitudes at 2.5 $dm^3\ s^{-1}$ and 3.5 $dm^3\ s^{-1}$ are recorded once, while the data points for 50 % and 100 % amplitude at 1.5 $dm^3\ s^{-1}$ are measured twice. The fixation of the transducer is achieved using a steel plate on top of the channel, from which a steel bar is extruded vertically into the channel. A screw mechanism allows for changes in the vertical positioning of the transducer. The results are compared to data obtained at the first position, where the transducer is fixed in an extra inlet module using a cross made of steel bars welded to the inlet. This fixation provides a better limitation of the transducer's degrees of freedom than the fixation within the first channel section. Here, the transducer is tested at maximum amplitude and for a flow velocity of about 2.5 $dm^3\ s^{-1}$. The experiment is conducted twice.

A schematic of the degasification test rig is displayed in Figure 5.6. It depicts the entire experimental setup, with TDG supersaturated water flowing from the pressure tank through the channel, passing the installed degasification device (in this case, an ultrasonic transducer is acting as a placeholder for such a device).

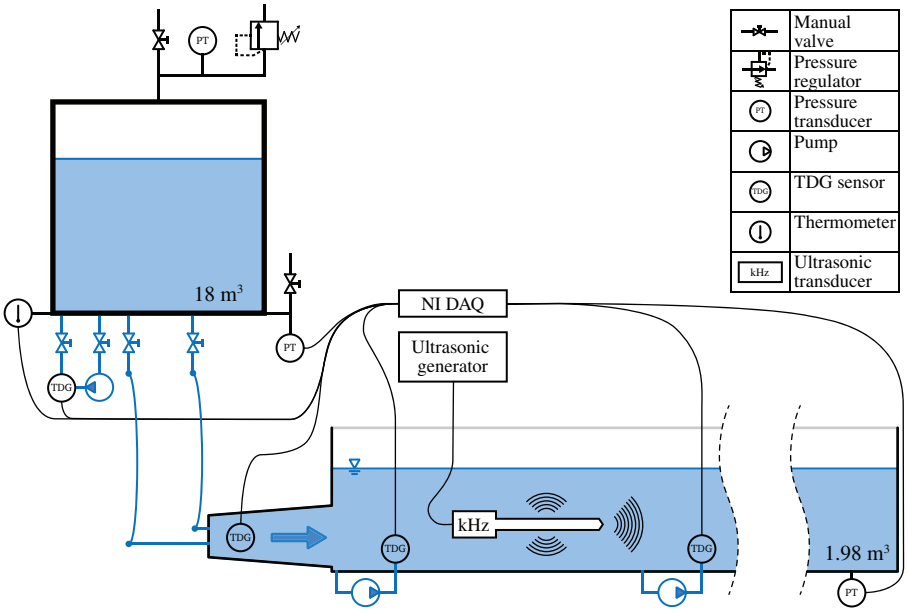

Figure 5.6: Schematic of the medium-scale test rig during degasification experiments. All relevant sensors are connected to NI DAQ modules which perform the data acquisition.

5.1.4 Summary

Similar to the experiments in small-scale, the input for the degasification experiments in the medium-sized test rig is provided by artificially increasing the TDG saturation level in water, using the 18 m^3 pressure tank within the Waterpower Laboratory at NTNU. The tank is filled with 15 m^3 of water from an in-house reservoir, which is subsequently pressurized. Then, gas is flushed in through a gas diffuser at the bottom, leading to small air bubbles rising to the top of the water column. Due to the increased pressure and interfacial area, the TDG saturation increases over time.

This water is then transferred into the degasification test rig, where it flows past a degasification device. In the case presented, this is a single ultrasonic rod transducer. The liquid-gas mass transfer is determined by monitoring the TDG saturation level both up- and downstream the transducer position. To test different scenarios, the volumetric flow rate and the transducer power are adjusted between the respective experiments. All equipment necessary to conduct the experiments, and the input, methods, and output of the tests are given in Table 5.1.

Table 5.1: Summary of experimental methods during degasification experiments in the medium-sized test rig, including the main equipment, input, applied methods, and output.

Supersaturation	

Equipment:	• Pressure tank (in-house system)
	• Pressure relief valve (Brewtools)
	• Gas diffuser (oxygenation stone)
	• Pressure regulator (Festo MS4-LR)
	• Circulation pump (Grundfos TP 40-50/2)
	• Sensors ($f = 1$ Hz)
	  ◦ TDG sensor (InWater Technologies PT4)
	  ◦ Thermometer (PT100)
	  ◦ Pressure transducer (GE PTX 610)

Input:	• Water (in-house reservoir)
Methods:	• Pressure increase • Gas bubbling
Output:	• TDG supersaturated water

Continued on next page

Table 5.1 – continued from previous page

Degasification	
Equipment:	• Open flume (custom build) • Sensors ($f = 1\,\mathrm{Hz}$) ◦ TDG sensors (InWater Technologies PT4) ◦ Pressure transducers (GE PTX 610 & Vega Vegabar 14) ◦ Thermometer (PT100) • Ultrasound (SinapTec INSIDE generator & 20 kHz rod transducer) • Flow acceleration pumps (Eheim compactON 5000)
Input:	• TDG supersaturated water
Methods:	• Ultrasonication ◦ Acoustic power ◦ Volumetric flow rate
Output:	• Decrease in TDG saturation

5.1.5 Calculation of the volumetric liquid-gas mass transfer coefficient

In contrast to the degasification process within the batch reactor discussed in Chapter 4, which results in a continuous mass transfer until a saturation plateau is reached, the process apparent in the medium-sized test rig represents a step in the saturation level. This is due to the continuous flushing of the test rig with water at a constant TDG supersaturation level. The degasification application is therefore only exposing a limited volume of water for a certain residence time, which is dependent both on the volume under degasification and the flow velocity. Measuring the TDG saturation upstream the degasification application will show a constant value, while the downstream sensors will record a step between the non-degasification and the degasification case. Due to the TDG sensor's adjustment time, the average values of the plateau emerging from the measurement data at the respective positions are taken for the calculation of the volumetric liquid-gas mass transfer coefficient. Taking the sensor readings after waiting for sufficient adjustment to the TDG saturation allows for neglection of the sensor's time constant (as discussed and determined in Section 4.1.4).

Following the description in Section 2.2.1, the $k_L a$ calculation starts from the equation for the mass transfer taking place within a volume (Equation 2.12). As in Chapter 3, the concentration difference is switched to represent mass transfer from the liquid to the gaseous phase, and the bulk concentration, C_{bulk}, is replaced by the average gas concentration, $C_{gas,avg}$. In addition, the TDG sensors use their

built-in atmospheric pressure sensor to output the TDG saturation, which is why in this case the concentration is replaced by the saturation:

$$\Phi = V\, k_L a \left(S_{\mathrm{TDG},avg} - S^*_{\mathrm{TDG}}\right). \tag{5.3}$$

As mentioned in the previous section, the degasification process will result in a saturation step between the measurements up- and downstream the degasification application. Therefore, the stable sensor readings, i.e. after the sensor responded to the saturation change, are averaged to detect the saturation difference. The flow of gas out of solution, Φ, is then calculated from the saturation difference between two sensors, A and B, multiplied by the volumetric flow rate, Q:

$$\Phi = Q\left(S_{\mathrm{TDG},A} - S_{\mathrm{TDG},B}\right). \tag{5.4}$$

The average TDG saturation, $S_{\mathrm{TDG},avg}$, is calculated using the logarithmic mean of the saturation measured at the locations A and B:

$$S_{\mathrm{TDG},avg} = \frac{S_{\mathrm{TDG},A} - S_{\mathrm{TDG},B}}{\ln S_{\mathrm{TDG},A} - \ln S_{\mathrm{TDG},B}}. \tag{5.5}$$

Inserting Equations 5.4 and 5.5 into Equation 5.3 and rearranging results in an expression for $k_L a$:

$$\begin{aligned} Q\left(S_{\mathrm{TDG},A} - S_{\mathrm{TDG},B}\right) &= V k_L a \left(\frac{S_{\mathrm{TDG},A} - S_{\mathrm{TDG},B}}{\ln S_{\mathrm{TDG},A} - \ln S_{\mathrm{TDG},B}} - S^*_{\mathrm{TDG}}\right) \\ \Rightarrow k_L a &= \frac{Q\left(S_{\mathrm{TDG},A} - S_{\mathrm{TDG},B}\right)}{V\left(\frac{S_{\mathrm{TDG},A} - S_{\mathrm{TDG},B}}{\ln S_{\mathrm{TDG},A} - \ln S_{\mathrm{TDG},B}} - S^*_{\mathrm{TDG}}\right)} \end{aligned} \tag{5.6}$$

The volume V describes here the volume of the test rig section in between the two measurement locations A and B, while the volumetric flow rate Q is the aforementioned average of the flow rate measured during the degasification process.

5.2 Results

Using the facilities at the Waterpower Laboratory at NTNU, water is TDG supersaturated and subsequently used to test the degasification efficiency of power ultrasound. Results are presented for the supersaturation process using the pressure tank, where different ambient pressures and air-flows are tested. Afterwards, the study of liquid-gas mass transfer during sonication of flowing water in dependence of operating parameters is presented.

5.2.1 Supersaturating water for laboratory experiments

The generation of a large enough volume of TDG supersaturated water to run degasification experiments within the medium-sized test rig is investigated using the methods descried in Section 5.1.1. The resulting data is displayed in Figure 5.7.

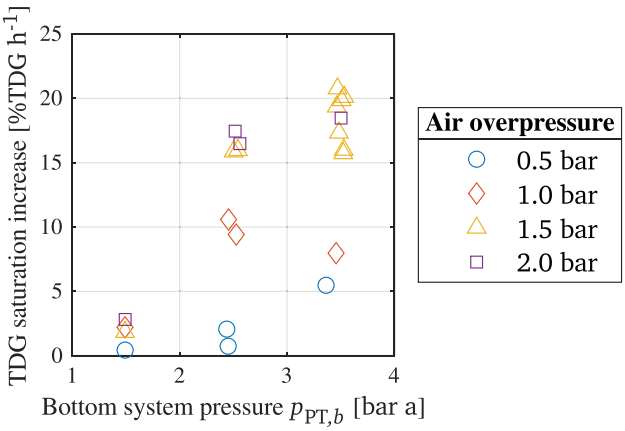

Figure 5.7: TDG increase in dependence of the pressure tank system pressure, $p_{PT,b}$ (measured at the bottom of the pressure tank), and air overpressure at which air is introduced into the system, p_{air}. Part of the data is taken from Gütle (2021). The data is available in Table A.8.

The data reveals a clear dependence on both system pressure and air pressure. Introducing air into the system at atmospheric pressure leads to a small TDG saturation increase over time, with almost no differences between the studied air overpressures. Those are far more pronounced when increasing the system pressure, with a plateau emerging for the 1.5 bar and 2.0 bar overpressure settings. One outlier is found for the 1.0 bar air overpressure at the highest system pressure, as the TDG saturation increase per hour is lower than the ones found at 1 bar system pressure increase. The system pressure is limited by the pressure relief valve with its maximum threshold pressure of 2.2 bar. Therefore, the optimal setting to create TDG supersaturated water is found at a system overpressure of 2 bar in combination with an air overpressure of 1.5 bar. The mean hourly increase in TDG saturation level for these settings is 18.45 %TDG h^{-1}.

5.2.2 Ultrasonic degasification in the medium-sized test rig

The medium-sized test rig at the Waterpower Laboratory at NTNU is used for the evaluation of the effect ultrasonic degasification has on TDG supersaturated, flowing water. As described in Section 5.1.3, the flow within the open channel is laminar and uniform. The SinapTec rod transducer is installed within the first channel section. Its mean frequency during the experiments is 20.34 kHz. In general,

the TDG sensors pick up the change in TDG saturation level at their respective position during flushing of the channel with TDG supersaturated water, as well as during sonication. The changes are detected with a time lag between the sensors due to the low flow velocity. From the TDG saturation measured within the channel, the natural degasification taking place between the different sections is determined by calculating the volumetric liquid-gas mass transfer coefficient, $k_L a$.

A boxplot of the TDG saturation values measured at the four channel positions in silent conditions, i.e. without any artificial degasification taking place, is displayed in Figure 5.8. The boxes show a spread in the saturation values measured at each position, especially at the channel inlet. The mean values are about equal, with 166.34 %TDG, 166.58 %TDG, 165.78 %TDG and 166.27 %TDG at the 0.00 m, 4.25 m, 9.25 m and 14.25 m channel position, respectively. A slight decrease in the TDG saturation level over the channel length is apparent from the median values, which are 169.11 %TDG, 166.93 %TDG, 165.59 %TDG and 165.06 %TDG at the respective channel position 0.00 m, 4.25 m, 9.25 m and 14.25 m.

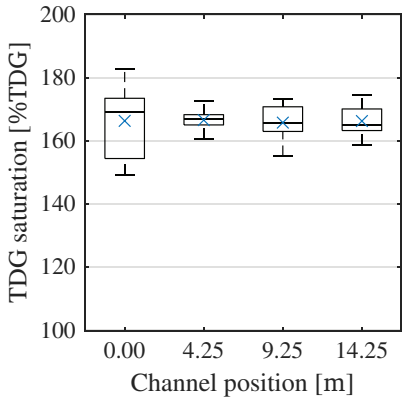

Figure 5.8: Boxplot of the TDG saturation level before degasification at four measurement positions within the medium-sized test rig. Boxes showing the interquartile range including median. Top and bottom line showing maximum and minimum. Mean values indicated by ×. The data is available in Table A.9.

Using Equation 5.6, the $k_L a$ for the three sections is calculated using the median values. For this calculation, the average flow rate taken from all experiments is used. The resulting values are $1.64 \cdot 10^{-4}\,\mathrm{s}^{-1}$, $1.23 \cdot 10^{-4}\,\mathrm{s}^{-1}$ and $0.92 \cdot 10^{-4}\,\mathrm{s}^{-1}$ for the respective sections, i.e. the same range of magnitude found for natural degasification in a river (see Section 3.3).

From the step in TDG saturation values between the channel inlet and the respective downstream measurement position during ultrasonic degasification, the

volumetric liquid-gas mass transfer coefficient is determined from measurement data at the inlet of the channel and the respective end-point of the channel section of the degasification test rig. A boxplot of all determined $k_L a$ values in dependence of the test rig section is displayed in Figure 5.9. The range of magnitude, if taking the irradiated volume retrospectively into account, is coherent with the values obtained in the batch reactor for sonication at about 37 W acoustic power (see Figure 4.10). Between the channel sections, the results show a decline in the liquid-gas mass transfer with the downstream distance. The trend is uniform, with the range of $k_L a$ values being smaller in the third section.

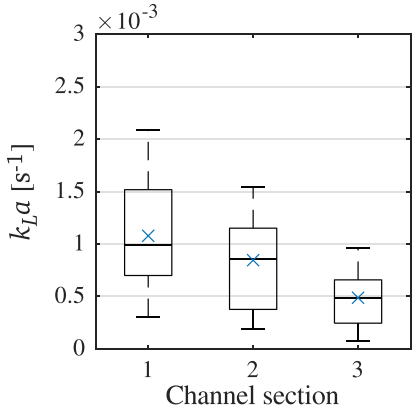

Figure 5.9: Boxplot of all $k_L a$ values obtained from the TDG saturation values measured at the channel inlet and the respective end-point of each section. Boxes showing the interquartile range including median. Top and bottom line showing maximum and minimum. Mean values indicated by ×. The data is available in Table A.9.

When doing the same calculation, but taking the measured TDG saturation values at the start- and end-point of each section instead of relating all end-points to the channel inlet, a similar pattern is observed. The resulting data is displayed as a boxplot in Figure 5.10. In comparison with Figure 5.9, the values in the third channel section are reduced. This shows that the third section does not contribute much to the degasification.

The values in the second section, on the other hand, are higher than expected, as the degasification supposedly takes place only in the first section. This reveals a continuation of the degasification effect, which is both attributed to a presumable extension of the acoustic field into the downstream section, and a cloud of degasification bubbles that emerges during sonication. The cloud of micro-bubbles appears directly downstream the transducer, filling up the channel and traveling both downstream and upwards within the water column, hence leading to a milky turbidity. The size of the micro-bubble cloud is directly dependent on the acoustic power and

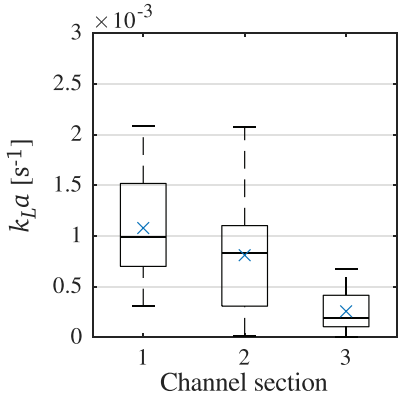

Figure 5.10: Boxplot of all $k_L a$ values calculated from the TDG saturation values between the respective start- and end-point of each section. Boxes showing the interquartile range including median. Top and bottom line showing maximum and minimum. Mean values indicated by ×. The data is available in Table A.9.

the flow velocity, with a gradient in bubble density towards the water surface being apparent from optical observation through the channel windows. Pictures of the first window, i.e. the end of the first channel section, for silent condition as well as during sonication using power ultrasound, are displayed in Figure 5.11. They show the see-through state of TDG supersaturated water during silent conditions (left), and the micro-bubble cloud appearing during sonication using 20 kHz ultrasound (right).

Figure 5.11: Window at the end of the first channel section (4.25 m downstream the channel inlet) during silent conditions and low flow (left) and sonication using 20 kHz ultrasound, leading to the creation of a micro-bubble cloud, and high flow (right).

An additional optical observation is acoustic Lichtenberg figures, as described by Mettin et al. (1999), which appear in the vicinity of the rod of the ultrasonic transducer. These are a sign of gas bubbles being forced out of solution by the acoustic field. The gas bubbles partly accumulate and rise to the water surface above the rod transducer in form of large bubbles. This behaviour is similar to observations made in literature, e.g. Li et al. (2022a).

To show the dependence of the liquid-gas mass transfer on the volumetric flow rate and the transducer's power is apparent in Figure 5.12. Here, all data points obtained during the parameter study are plotted. As in Figure 5.9, the highest values are obtained within the first section of the test rig, with a consecutive decline in the following two sections. From the markers' color scale, the direct dependence on the $k_L a$ on the volumetric flow rate and thus the flow velocity is apparent, with the highest values being reached at the highest flow. Moreover, a strong effect of the transducer's power is visible, similar to the one discovered during sonication in the batch reactor discussed in Section 4.2.2. A combination of high flow and high transducer powers therefore yields the highest $k_L a$ values. The data obtained for each individual test rig section is displayed in Figures A.5, A.6, and A.7.

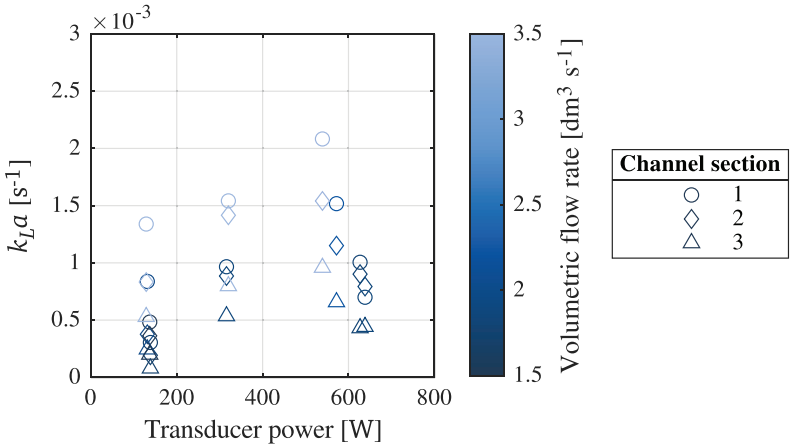

Figure 5.12: $k_L a$ values obtained during sonication using 20 kHz ultrasound, in dependence of flow rate and transducer power, for the three channel sections. Plots depicting values for each individual section are displayed in Appendix A.3, and the data is available in Table A.9.

To test the inlet section of the test rig as placement for a degasification application, the SinapTec rod transducer is moved towards this position. Here, the maximum amplitude setting of the transducer is tested at a high flow rate. The mean volumetric flow rate in this case is 2.48 $\mathrm{dm^3\,s^{-1}}$, and a power of 1.44 kW was transmitted by the transducer. As a result, a $k_L a$ value $28.48 \cdot 10^{-3}\ \mathrm{s^{-1}}$ within the inlet and $4.75 \cdot 10^{-3}\ \mathrm{s^{-1}}$ in the first channel section is obtained (The data is available

in Table A.10). This confirms the dependency of the liquid-gas mass transfer on the acoustic power, as discussed in Section 4.2.2.

5.3 Discussion

The efficiency of ultrasonic degasification to reduce the TDG saturation level from TDG supersaturated, flowing water is studied. Do to so, a method is developed to increase the TDG saturation level in a large amount of water. This water is subsequently channeled through the degasification test rig, where the efficiency of the ultrasonic degasification process is investigated.

As shown, the method to produce a large volume of TDG supersaturated water by increasing the ambient pressure of a vessel while introducing air bubbles is efficient. The decrease in time to reach the desired TDG saturation level is achieved due to the increase in interfacial area between the injected air and the water. The TDG saturation increase over time has a peak at an air overpressure of 1.5 bar at the bottom of the pressure tank, independent of the ambient pressure. Below this pressure, the influx of air into the water is too little to obtain a sufficiently fast increase in the TDG saturation. A higher air pressure results in too much coalescence of bubbles before separating from the oxygenation stone, thus decreasing the interfacial area and consequently the mass transfer. The increase in TDG saturation over time is linearly dependent on the ambient pressure, as is apparent from Henry's law (see Equation 2.5). This is well captured by the recorded data. The mean increase in TDG saturation of 18.45 %TDG h^{-1} at the optimum settings allows for reaching saturation values similar to the once recorded in nature, as described in Section 3.3, in a reasonable amount of time (see also Figure 3.7 for the range of maximum TDG saturation levels measured in the Otra river downstream Brokke power plant).

The $k_L a$ values calculated from the median TDG saturation values at each measurement position during silent conditions in the test rig show that mass transfer takes place within the test rig as well, even though the channel's length is comparably short. The values are in the same range of magnitude as the $k_L a$ values obtained from the measurements in the Otra river. Looking at the average TDG saturation in the channel, almost no difference between the measurement stations is apparent, thus indicating that the actual degasification taking place is smaller. This is as expected, as the laminar flow in the test rig compared to the moderately agitated flow in the river presumably leads to a much smaller liquid-gas mass transfer. Similarly, smaller $k_L a$ values further downstream in the test rig are expected when looking at the calculation method. The volume between the measurement positions used for the calculation increases, while the decrease in TDG saturation level between the downstream measurement stations is rather constant. Following Equation 5.6, the volumetric liquid-gas mass transfer coefficient therefore has to

decrease with an increasing volume, assuming that all other variables change in a minor fashion.

The use of power ultrasound to sonicate the water flowing past the transducer increases the liquid-gas mass transfer. Comparing the $k_L a$ values obtained in the first section with ones calculated from the natural degasification process in the Otra river shows a difference of one order of magnitude. This shows again the efficiency of the ultrasonic degasification process, as discussed in Section 4.2.2. An additional effect on the mass transfer is introduced by the micro-bubble cloud, which takes up dissolved gas species on its way upwards in the water column and downstream in the channel. This is observed by increased volumetric liquid-gas mass transfer coefficient values in both the first and second section of the channel. When power ultrasound is applied within the inlet of the test rig, the volumetric liquid-gas mass transfer coefficient is even higher, due to the higher power transferred by the transducer at that position. Yet, the values do not reach the maximum values obtained during sonication in the batch reactor, even though the absolute transducer power is much higher. A reason for this is found in the differences in the sonicated volume, which is about 8 dm^3 within the medium-sized test rig compared to the 0.75 dm^3 in the batch reactor[19]. From this, the maximum power per sonicated volume is calculated to be 215 $\mathrm{W\,dm^{-3}}$ in case of the rod transducer and 530 $\mathrm{W\,dm^{-3}}$ for the horn transducer. At the lower end of the horn transducer's transmitted power per sonicated volume, the resulting $k_L a$ values fit with the ones obtained for similar parameters of the rod transducer. It is therefore concluded that the transmitted power in the degasification test rig has a similar effect on the liquid-gas mass transfer as described in the batch reactor, and that high acoustic powers would result in higher $k_L a$ values.

The introduction of small bubbles into the flow may prove beneficial for the degasification in the medium-sized test rig, even though the results from the batch reactor do not imply it. The reason for this would be the increased liquid volume, which decreases bubble coalescence directly after their introduction. The application of bubbles into the water would lead to a bubble curtain, which can be tested both up- and downstream the ultrasonic transducer, as well as stand-alone.

5.3.1 Calibration of the $k_L a$ model

The model to predict the volumetric liquid-gas mass transfer coefficient in dependence of the acoustic power per volume and flow velocity, which was developed in Section 4.3, is applied using the transducer's experimental settings in the medium-sized test rig. The resulting values are compared to the actually determined values from the first channel section. A direct comparison is possible from Figure 5.13. The range of magnitude of the model is in good agreement with the data. Yet, it

[19]The sonicated volume in the medium-sized test rig is assumed to be a cylinder extending 5 cm from the transducer's rod surface.

is apparent that the transducer power is underrated at lower powers, and that the influence of the volumetric flow rate is not represented correctly. In fact, the flow appears to shift the results towards higher $k_L a$ values.

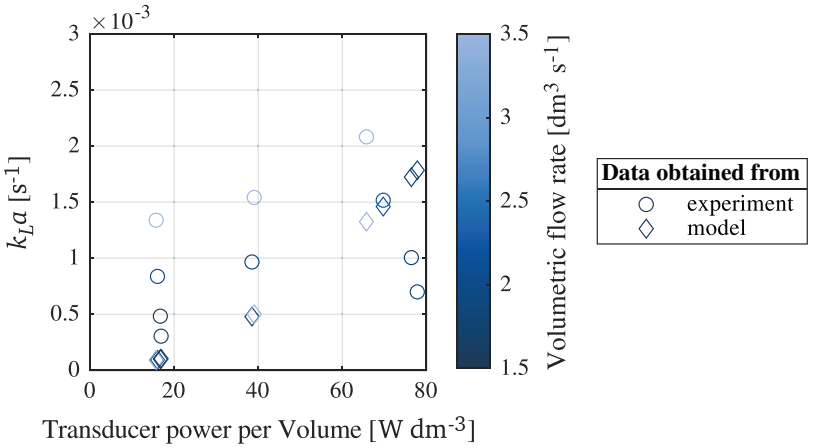

Figure 5.13: $k_L a$ values obtained during sonication using 20 kHz ultrasound, in dependence of flow rate and transducer power, for the first channel section, and the values obtained using the model applied for the same test rig settings.

Both data and model show the beneficial effect of increasing the acoustic power, even though the transducer shape influences the shape of the trend. A follow-up study of the flow and turbulences within the acoustic field is required to have a better understanding of the decisive effects. The difference in size of the acoustic fields has an influence on the degasification as well, as the number of pressure nodes within the liquid changes, subsequently increasing bubble accumulation points (as described in Section 2.3.2). Nevertheless, the effect of different acoustic fields on the degasification effect is to-date subject to presumptions.

To have a better representation of both acoustic power and volumetric flow rate for the case of the medium-sized test rig, the $k_L a$ model is adjusted. This also leads to a better fit to the geometrical and practical setup of the medium-sized test rig, hence shifting the model closer towards the natural application as well. Instead of the power fit, a second-order polynomial fit is used to include the shift introduced by the flow velocity:

$$(k_L a)_{\mathrm{mdl}} = A_{\mathrm{mdl},1} \left(\frac{P_{ac}}{V} \right)^2 + A_{\mathrm{mdl},2} \left(\frac{P_{ac}}{V} \right) + \beta \, U_{cs}. \tag{5.7}$$

While the coefficients $A_{\mathrm{mdl},1}$ and $A_{\mathrm{mdl},2}$ are determined by approximation of the original model, β is determined by fitting $k_L a$ data from the first section of the medium-sized test rig. Here, the data points representing the highest flow velocity

and the ones for an intermediate flow velocity are fitted, respectively. The final model is obtained by averaging all coefficients, including those from the original model. By doing so, the model increases its possibility of representing different transducer types. The adjusted model has the following form:

$$(k_L a)_{\mathrm{mdl}} = 1.71 \cdot 10^{-7} \left(\frac{P_{ac}}{V}\right)^2 + 9.36 \cdot 10^{-7} \left(\frac{P_{ac}}{V}\right) + 3.60 \cdot 10^{-4}\, U_{cs}. \quad (5.8)$$

Three lines of constant flow velocity, calculated using the model in Equation 5.8, are plotted in Figure 5.14, together with the $k_L a$ data obtained from the ultrasonic degasification experiments in the first section of the test rig. As apparent from this figure, the trend of the transducer is much better captured. In addition, the effect of the flow velocity, i.e. the shift towards higher $k_L a$ values, is implemented.

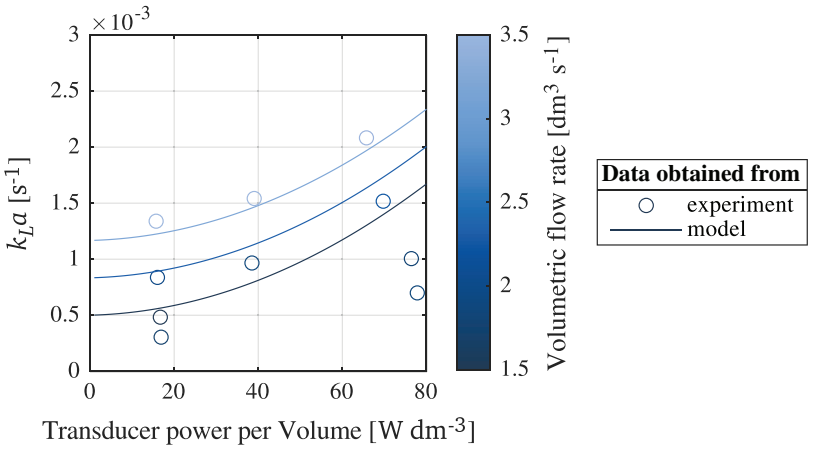

Figure 5.14: Three lines of constant flow velocity obtained using the $k_L a$ model, together with experimental data during sonication using 20 kHz ultrasound in the first section of the medium-sized test rig.

The model is built on data obtained from experiments using two different setups. This is both an advantage, as the fit includes a wider variety of cases, and a disadvantage, as the data of neither cases is having a perfect representation of the data. Nevertheless, the model gives a possibility to evaluate the required acoustic power per volume for a given flow and degree of TDG supersaturation. Therefore, it has the unique capability of predicting real-world scenarios, even though further calibration with data from higher flow cases is needed.

Using the model, an attempt is made to calculate the power requirement for mitigation of TDG supersaturation to ecologically tolerable levels, i.e. a TDG saturation of 110 %TDG. In Figure 5.15, measurement data during one experimental

run within the medium-sized test rig within the first section is displayed both before (silent) and during sonication. In this case, an average flow rate of 3.51 $dm^3\ s^{-1}$ is used, and the sonication with the 20 kHz rod transducer takes place with a transmitted power of 539 W. The data points during sonication are extrapolated to achieve a total reduction down to the desired saturation level. From the resulting, modeled values, the required transmitted power is determined by calculating the volumetric liquid-gas mass transfer and using it to reversely calculate the power from the $k_L a$ model. The result is a transmitted acoustic power of 1818 W. Again, this is only valid under the aforementioned assumptions, yet gives an idea of the range of magnitude of the requested power.

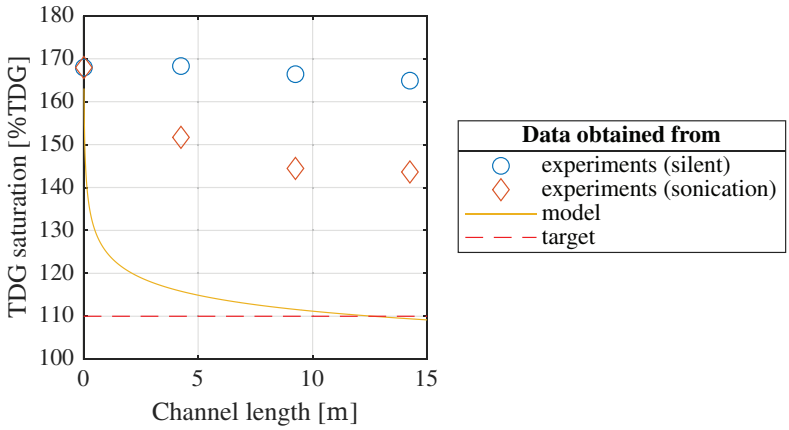

Figure 5.15: Measured TDG saturation values at several locations within the medium-sized test rig at an average volumetric flow rate of 3.51 $dm^3\ s^{-1}$ for silent conditions, during sonication with 20 kHz ultrasound with a transmitted power of 539.35 W, and for modeled values representing an ideal situation.

5.3.2 Critical contemplation of the test rig design

The medium-sized test rig gives the unique opportunity to test degasification mechanisms on TDG supersaturated, flowing water, in a geometry that provides a simplified representation of a real-world case. It is shown that the degasification using power ultrasound increases the liquid-gas mass transfer, thus helping mitigate TDG supersaturation. Differences to the results obtained from batch experiments show the problems a real-world scenario poses. Using the developed $k_L a$ model, important parameters can be identified that influence the degasification process. Yet, the test rig has some flaws in its design, which can be overcome due to adaptations.

As a first, the major dependency of the flow velocity in the test rig on the hydrostatic head in the pressure tank, and the subsequent decrease in flow over time makes it difficult to have a precise evaluation of its influence on the degasification.

In addition, the limited volumetric flow in the channel due to the limitation in available volume of the pressure tank makes further studies of the flow's effect on the degasification mechanism difficult. Comparing the maximum flow velocity in the test rig, 4.17 cm s^{-1}, to the arbitrary power plant discussed in Section 2.2.2, which has a flow velocity of 2.5 m s^{-1}, shows the need for further experiments to study scaling effects. Even though the data reveals an increase in the liquid-gas mass transfer with the flow rate, a possibility of an optimum or peak flow velocity exists. This can only be detected by increasing the flow rate within the channel. As a solution to both problems, a mechanism to control the pressure tank's outflow pressure by introduction of air into its head space is suggested. By that, the flow rate in the channel will be constant, and an increase in the system pressure yields higher flow rates as well. Yet, the final limit of the test rig is set by the V-notch. Thus, even higher flow rates create the need for either upgrading to a new test rig, or starting with field tests.

Another flaw is the different apparatus used to mount the ultrasonic transducer at the two positions within the test rig. A better fixation of the transducer at the inlet position is accomplished, while the one within the first channel section allows movement of the fixation during sonication, thus leading to a decrease in the transferred power. This shows the need of having proper fixations to limit the transducer movement during operation. The identification of these flaws gives the opportunity for future revisions, hence leading to a better representation of the degasification of TDG supersaturated water in a river.

The system at the Waterpower Laboratory comes with some drawbacks as well. First, the water temperature in the reservoir cannot be regulated and is therefore dependent on the ambient temperature. Its influence on the experiments is therefore disregarded, even though the water temperature differs by about 10 °C throughout the year. This has implications on the solubility of gases in water, as discussed in Section 2.2.1, therefore influencing the degree of TDG supersaturation achieved in the pressure tank as well as the degasification efficiency in the test rig. In addition, the water is neither treated mechanically nor chemically to clean or purify it. This, together with the fact that additional experiments are run in the Waterpower Laboratory using the same water as source, leads to an uncertainty regarding organic or inorganic suspended matter. A higher degree of such pollutants can influence the efficiency of the ultrasonic degasification process as well. Fortunately, this influence is presumably positive, as more nucleation points are available for bubbles. Also, the water within the river is not clean either, which shifts the results from the medium-sized test rig presumably closer to the ones obtained in the field.

5.4 Conclusion

The ultrasonic degasification of TDG supersaturated, flowing water is studied. At the Waterpower Laboratory at NTNU, a test rig is designed and built to allow for researching different degasification methods. A procedure is developed to create the amount of TDG supersaturated water needed to conduct the experiments, using an in-house pressure system. Ideal conditions are found in creating a high ambient pressure in combination with introduction of air bubbles at an overpressure of 1.5 bar at the bottom of the pressure vessel. Thus, both ambient pressure and interfacial area are increased, subsequently leading to an increase in gas dissolution.

The resulting TDG supersaturation level is stable for the duration of all subsequent experiments. A transfer to the test rig takes place without saturation losses due to natural degasification, as the pressure drop at the outlet of the pressure vessel is smoothened using friction losses in long hoses. The test rig itself gives a lot of opportunities for experiments. Different positions are available for mounting degasification applications, and the flow and TDG saturation level are adjustable. Yet, the flow velocity in the test rig is low in comparison to most natural cases. Despite this, the test rig gives a first idea of the parameters influencing the liquid-gas mass transfer during degasification of TDG supersaturated, flowing water, as well as the challenges and problems a real-world setup faces. Proposals for upgrades are discussed.

The use of continuous sonication with 20 kHz ultrasound leads to a step in the TDG saturation level. The volumetric liquid-gas mass transfer is found to be lower than the one obtained during sonication in the batch reactor. This is mostly attributed to the different transducers in use, and the differences in sonicated volume leading to a smaller transmitted power per volume in the medium-sized test rig compared to the batch reactor where the transmitted acoustic field is confined. Furthermore, the degasification using ultrasound leads to high $k_L a$ values not only in the section where the transducer is installed, but also in the downstream section. A reason for this is the formation of a micro-bubble cloud traveling downstream in the channel and contributing to the degasification by taking up more dissolved gas species. In contrast to the batch reactor experiments, increasing the flow has a beneficial effect on the liquid-gas mass transfer. The model developed in Chapter 4 yields values in the same range of magnitude as the measurement data, but is nevertheless adjusted to give a better representation of the ultrasonic degasification process in the medium-sized test rig.

To improve it further, more experimental data is required from the test rig. In addition, other degasification mechanisms can be tested using it, e.g. aeration by introduction of gas bubbles. Moreover, ultrasonic transducer can be operated in different modes as well, e.g. with pulsed sonication or frequency sweeps, thus possibly decreasing the energy used or increasing the liquid-gas mass transfer.

These opportunities are possible and easy to implement using the equipment studied in this chapter.

CHAPTER

SIX

Discussion

A study of the liquid-gas mass transfer in case of total dissolved gas (TDG) supersaturation of water within different situations and under varying conditions has been presented. In the first step, a method was developed to calculate the volumetric liquid-gas mass transfer coefficient, $k_L a$, from TDG saturation measurement data obtained from several points within the Otra river downstream Brokke power plant in southern Norway. Several TDG supersaturation events are detected in the period from July 2012, to December 2013, with the highest TDG saturation values measured being 173 %TDG at the power plant outlet. The resulting $k_L a$ values between the outlet and the first and second measurement station downstream the power plant were in the range of $10^{-4}\ \mathrm{s}^{-1}$, while the values between the outlet and the last measurement station had a range of $10^{-5}\ \mathrm{s}^{-1}$. This decrease in the $k_L a$ with the distance to the downstream measurement stations was attributed to the river's morphology and characteristics, which differ between the first two and the last station. This directly influences the agitation of the river in these parts. The method was concluded to yield plausible results also when compared to values reported by literature, even though it is based on several assumptions and simplifications regarding the mathematical approximation of the shape of the TDG saturation curves over time, as well as the river's morphology, flow, and characteristics. Due to a generally small range of magnitude, natural degasification is seen as a slow process unfit to lead to a sufficiently fast mitigation of TDG supersaturation. Consequently, it was concluded that technical methods to increase the liquid-gas mass transfer within a river downstream a hydropower plant, other than those coming from civil engineering, need to be studied.

The findings reveal the impact of environmental factors on the liquid-gas mass transfer during natural degasification. Both river morphology and characteristics have a significant effect on it, as shown by the gradient in the $k_L a$ values between

the different downstream measurement stations. This is of interest when studying the need for technical degasification at an actual hydropower power plant. The local environmental conditions will define the effort needed to mitigate TDG supersaturation in the river downstream. Parameters to think of during studies of specific cases are e.g. economical factors, mixing behaviour, and the need for decrease in TDG saturation level to achieve biological tolerance.

The second step is about the efficiency of selected operating parameters to increase the liquid-gas mass transfer. Experiments were conducted within a liquid batch reactor, where sonication using ultrasound, gas bubbling, and an induced flow circulation were tested both individually and in combination. For ultrasound, the dependency on the ultrasonic frequency and the transmitted acoustic power was determined. Gas bubbling was conducted using gas dispersers with different pore sizes, as well as different gas flows. The flow was circulated using multiple volumetric flow rates in both con- and countercurrent direction. Ultrasound at high transmitted acoustic powers was found to lead to the by far largest increase in the $k_L a$ when compared to the other methods, reaching values in the range of mid 10^{-2} s^{-1} in comparison to mid 10^{-3} s^{-1} for flow circulation and high 10^{-3} s^{-1} for gas bubbling. In combination with sonication, a flow circulation led to similar values of the volumetric liquid-gas mass transfer coefficient, while the combination with gas bubbling yielded lower $k_L a$ values. Yet, sonication using ultrasound in combination with the other methods increased the liquid-gas mass transfer in all cases, compared to single parameter operation. This shows that a synergetic effect between the individual degasification parameters in the batch reactor is missing, and that ultrasonication is the driving factor in mass transfer enhancement. Nevertheless, the choice of equipment might lead to one-sided views on the problem, and the combination of degasification methods may prove more beneficial in different setups. Compared to the values obtained from the natural degasification in a river, sonication leads to a substantial increase in the liquid-gas mass transfer, with up to two orders of magnitude. This proves the hypothesis of ultrasonic degasification being a plausible tool for mitigating TDG supersaturation, even though the study is confined to a static, small volume of pure water.

From the results, an empirical model was developed to have a tool at hand for predicting the volumetric liquid-gas mass transfer coefficient in dependence of the acoustic power and the flow velocity. While the acoustic power is the major factor within this model, the flow velocity has only a limited influence on it. It was concluded that the model serves as a starting point for scale-up studies, but is in need of further calibration and verification, as it is based on limited data and only represents a narrow range of parameters.

Finally, a medium-sized test rig for degasification experiments was designed and built at the Waterpower Laboratory at NTNU. It provides the possibility to

study different degasification mechanisms on TDG supersaturated, flowing water, hence giving insights into the challenges and constraints faced by a real-world application. An experimental procedure was developed to efficiently increase the TDG saturation of a sufficiently large volume of water, which is used to provide a continuous flow within the test rig during the experiments. On average, the TDG saturation increased by 18.45 %TDG h^{-1}. Within the test rig channel, TDG saturation values were on par with the highest values measured at the power plant outlet in the Otra river. Ultrasonic degasification was tested at different positions within the test rig, and the dependency of the liquid-gas mass transfer on transferred acoustic power and the flow velocity was determined. It was confirmed that an increase in acoustic power is beneficial to mass transfer. Yet, in contrast to the batch reactor experiments, the flow velocity proved to increase the $k_L a$ values. The results for higher flow rates ranged in the low 10^{-3} s^{-1}. These values were found to be lower than in the small-scale experiments, which is attributed mainly to differences in the transmitted acoustic power per sonicated volume. The volumetric liquid-gas mass transfer coefficients were still one order of magnitude higher compared to the natural degasification in a river, thus proving that power ultrasound is capable of mitigating TDG supersaturation in a river. Moreover, sonication did not only increase the mass transfer within the section the ultrasonic transducer was installed in, but also within the following downstream section. This was accompanied by the observation of a large micro-bubble cloud downstream the transducer, which is therefore suspected to lead to increased mass transfer during the traveling of the bubbles both up within the water column and downstream the channel. The micro-bubble behaviour provides insights into the mechanisms underlying the increase in liquid-gas mass transfer, and opens the door for a better understanding of the physical processes involved in it. In addition, it supports the findings of the batch reactor experiments, and shows the suitability of applying ultrasonic degasification within a river.

This establishes the need for further research in the direction of interaction of power ultrasound with the aquatic environment. Among others, the disturbance due to the introduction of sound or the danger of the ultrasonic field within the close vicinity of the transducer are things to be studied. The existence of suspended matter poses additional questions with regard to the efficiency of the degasification process. Such impurities in the water usually serve as nucleation points, by such creating a benefit to the liquid-gas mass transfer (Crum, 1982). Nevertheless, this remains to be proven in a real-world setting.

The $k_L a$ model developed empirically from the batch reactor data was found to predict values in the correct range of magnitude in case of the degasification test rig, but was adjusted to give a better representation of the flow velocity's influence. Using the adjusted model, the theoretical power needed to provide a

sufficient reduction in the TDG saturation to reach ecologically tolerable levels was determined for a certain set of parameters. Flaws and opportunities of the test rig were discussed, and recommendations for further work were made.

To conclude, the method of ultrasonic degasification using power ultrasound, particularly at high transmitted acoustic powers, was identified as a highly effective tool capable of mitigating TDG supersaturation from flowing water in a laboratory setting. In comparison with the natural degasification in a river, the liquid-gas mass transfer was substantially increased both in case of sonication of TDG supersaturated, static water in a batch reactor, and TDG supersaturated, flowing water in the degasification test rig. The acoustic power transferred to the liquid was the major factor influencing the liquid-gas mass transfers compared to other parameters tested within this study. Results from the batch reactor and the medium-sized test rig for the case of sonication using 20 kHz ultrasound were similar when taking the transferred acoustic power per volume into account. The influence of the water's flow velocity appeared to be beneficial, which could be due to limited flow velocities in the test rig. It therefore remains to be finally clarified by further laboratory experiments or field tests. The empirical model creates the possibility to estimate the power needed in a real-world scenario (in dependence of the flow velocity and the TDG saturation level), but is based on limited data, and should hence be further calibrated to increase its quality. When reaching the manufacturer's limit in acoustic power transferred by the ultrasonic transducer, alternative setups like having multiple transducers in a certain arrangement may prove beneficial. The optimal vertical placement of an application to mitigate TDG supersaturation at the outlet of a hydropower plant, as well as possible interactions in a multi-transducer setup remain to be studied further.

The study takes the field of liquid-gas mass transfer towards formerly unknown use. By addressing the issue of TDG supersaturation, it contributes to the broader theoretical framework for balancing energy production with environmental conservation, and underscores the importance of developing sustainable practices in hydropower generation. The determination of liquid-gas mass transfer coefficients to create comparability between different scenarios and setups is unique. In addition, the Waterpower Laboratory provides opportunities in space and equipment not easily found elsewhere, e.g. the in-house method to create large volumes of water with a high degree of TDG supersaturation. Consequently, the comparability with literature proves difficult. Nevertheless, the $k_L a$ values obtained from the experiments in both the batch reactor and the medium-sized test rig are in a coherent range of magnitude when compared to values reported by studies on optimization of the liquid-gas mass transfer. The effect of the introduced flow on degasification methods is increasing the knowledge beyond the scope of this project, and the test rig provides a large range of possibilities for further testing.

Besides identifying a possible tool, the findings provide insight into the general mechanisms working towards the mitigation of TDG supersaturation downstream hydropower plants. Challenges and constraints of a potential field application are easily identifiable, and the effects of different parameters can be studied. In case of ultrasonic degasification, it is possible to utilize the empirical model toward designing a prototype degasification application. By providing estimates of the required power, it also opens for economic assessments valuable to hydropower plant owners and operators. Moreover, the model opens for the possibility of conducting numerical studies to predict the efficiency of a degasification application by following the evolution of the saturation (or concentration) level within each numerical cell, using the $k_L a$ model as an input to basic equations. These theoretical foundations of both application design and efficiency create the possibility for scale-up from laboratory settings to real-world applications, even though questions remain to be answered along the way.

This has direct implications on the mitigation of TDG supersaturation downstream hydropower plants. Where its occurrence cannot be prevented, the TDG saturation level can be lowered by technical means. Therefore, an alternative to existing civil engineering approaches is established. The actual application will depend on the individual case, and it is far from certain that the solution offered is universally usable. Nonetheless, each successful application will help improve the aquatic environment, by such helping the hydropower sector on the way to an even more sustainable future.

CHAPTER

SEVEN

Conclusion

This Thesis converges topics from science, engineering, and environmental studies in order to increase the knowledge of a widely unknown topic, total dissolved gas (TDG) supersaturation in the river downstream a hydropower plant, and offers a possible mitigation tool: ultrasonic degasification. Using the volumetric liquid-gas mass transfer coefficient, $k_L a$, the efficiency of different parameters and methods is investigated. Based on certain assumptions and simplifications, the natural degasification of TDG supersaturation taking place in a river downstream a hydropower plant was evaluated and compared to degasification taking place in a small-scale batch reactor and a medium-sized degasification test rig. Ultrasonic degasification was found to be an outstanding method to decrease the TDG saturation both in static and flowing TDG supersaturated water, and the volumetric liquid-gas mass transfer was increased substantially in both cases. Differences occurring between the results were discussed thoroughly. Synergetic effects between different degasification techniques were evaluated, and may lead to the development of innovative degasification strategies. From the batch reactor's measurement data, an empirical model was developed, which was adjusted using the degasification test rig results. It gives the possibility to estimate the required transmitted acoustic power for real-world scenarios, but is in need of further calibration. Moreover, it opens the door toward numerical modeling of a degasification application's efficiency.

The outcome of this study provides a deeper understanding of the parameters leading to an increase in the liquid-gas mass transfer of TDG supersaturated, flowing water in case of degasification using power ultrasound. This is of importance for any mitigation effort approached by a real-world application. In addition, it adds depth to the comprehension of the mechanisms involved in degasification processes as well as mass transfer techniques, provides tools for industrial users, and creates opportunities for further studies. Nevertheless, open questions remain and new

problems have been identified. It is therefore of importance to continue research on the mitigation of TDG supersaturation by technical means. This has to be a joint effort of academia, industry, and the authorities, to create further knowledge, apply it, and put it into official frameworks. Only this will enable the change needed to improve the protection of the aquatic environment, hence making hydropower an even greener and more sustainable technology. May there be curious minds to pick up where the author left off.

CHAPTER
EIGHT

Outlook

The findings of the study open for further studies of the identified problems and challenges with mitigating total dissolved gas (TDG) supersaturation in a river downstream a hydropower plant. A lot of open questions regarding a real-world application of power ultrasound remain. While being required to provide an economically feasible frame both during construction and operation, the lifetime of the equipment within non-pure water is of relevance. In addition, no further alterations of that water shall be introduced, e.g. changes in the pH value. The noise level around the transducer as well as its destructive effects in the close vicinity need to be taken into account. Effects of suspended matter on the liquid-gas mass transfer are of interest and in need of being studied as well. Finally, the introduction of the application within the tailrace tunnel or at the outlet of a hydropower plant shall not interfere with the power plant's dynamics.

The unique setup at the Waterpower Laboratory at NTNU opens for tests of additional degasification methods and holds the capability to incorporate upgrades and modifications. Regarding ultrasonic degasification, different operational modes of the transducer can be studied. An additional method could be the application of a bubble curtain, both as stand-alone and in combination with ultrasound.

Field testing allows for evaluating both the efficiency of the ultrasonic degasification process during scale-up and the empirical model. Mitigating TDG supersaturation presumable opens for new habitat within river stretches previously uninhabited by certain aquatic species, which should be monitored as well. Calibration of the $k_L a$ model with field data makes it a tool that can be used during the design process of a degasification application, for economical estimations, and for prediction of the degasification efficiency such an application has, e.g. by using computational fluid dynamics (CFD). It therefore provides the bridge between laboratory experiments and real-world cases.

The author expresses his hope for additional testing, especially in the field, to provide a more definite understanding of the actual applicability of the studied concept within the field of hydropower.

Bibliography

Acreman, M. (2016). Environmental flows—basics for novices. *WIREs Water*, *3*(5), 622–628. https://doi.org/https://doi.org/10.1002/wat2.1160

Adam, A., Paulkowski, D., & Mayer, B. (2019). Friction and Deformation Behavior of Elastomers. *Materials Sciences and Applications*, *10*(08), 527–542. https://doi.org/10.4236/msa.2019.108038

Adam, B. (2003). *Fischereilich relevante Grenz- und Richtwerte - Ein Tabellenwerk zur Beurteilung chemisch/phhysikalischer Gewässeruntersuchungen*. Institut für angewandte Ökologie.

Agarkoti, C., & Gogate, P. R. (2022). Mapping of cavitation intensity in a novel dual-frequency ultrasonic reactor of capacity 10 L. *Chemical Engineering Science*, *259*. https://doi.org/10.1016/j.ces.2022.117833

Agostinho, A. A., Alves, D. C., Gomes, L. C., Dias, R. M., Petrere Jr, M., & Pelicice, F. M. (2021). Fish die-off in river and reservoir: A review on anoxia and gas supersaturation. *Neotropical Ichthyology*, *19*(3). https://doi.org/10.1590/1982-0224-2021-0037

Alfredsen, K., & Bruland, O. (2022). Hydropower in Cold Regions. In *Comprehensive Renewable Energy* (pp. 284–299). Elsevier. https://doi.org/10.1016/B978-0-12-819727-1.00064-9

Alp, A., Akyüz, A., & Kucukali, S. (2020). Ecological impact scorecard of small hydropower plants in operation: An integrated approach. *Renewable Energy*, *162*, 1605–1617. https://doi.org/10.1016/j.renene.2020.09.127

Alvarez, E., Cancela, M. A., Navaza, J. M., & Taboas, R. (2002). Mass transfer coefficients in batch and continuous regime in a bubble column.

Alvik, S., Berglund, F., Horschig, T., Koefoed, A. L., Selvakkumaran, S., & Zambon, A. (2022). *Energy Transition Norway 2022: A national forecast to 2050*. DNV AS. Høvik, Norway.

Arnell, N. W. (2004). Climate change and global water resources: SRES emissions and socio-economic scenarios. *Global Environmental Change*, *14*(1), 31–52. https://doi.org/10.1016/j.gloenvcha.2003.10.006

Asakura, Y., & Yasuda, K. (2022). Frequency and power dependence of ultrasonic degassing. *Ultrasonics Sonochemistry*, *82*. https://doi.org/10.1016/j.ultsonch.2021.105890

Bakken, T. H., Harby, A., Liersch, S., & Koch, H. (2022). Hydropower Reservoirs—Benefits and Challenges. In *Comprehensive Renewable Energy* (pp. 105–125). Elsevier. https://doi.org/10.1016/B978-0-12-819727-1.00078-9

Bakken, T. H., Sundt, H., Ruud, A., & Harby, A. (2012). Development of Small Versus Large Hydropower in Norway– Comparison of Environmental Impacts. *Energy Procedia*, *20*, 185–199. https://doi.org/10.1016/j.egypro.2012.03.019

Bampouli, A., Goris, Q., Van Olmen, J., Solmaz, S., Noorul Hussain, M., Stefanidis, G. D., & Van Gerven, T. (2023). Understanding the ultrasound field of high viscosity mixtures: Experimental and numerical investigation of a lab scale batch reactor. *Ultrasonics Sonochemistry*, *97*. https://doi.org/10.1016/j.ultsonch.2023.106444

Bandara, W. M. K. R. T. W., Ikeda, M., Satoh, H., Sasakawa, M., Nakahara, Y., Takahashi, M., & Okabe, S. (2013). Introduction of a Degassing Membrane Technology into Anaerobic Wastewater Treatment. *Water Environment Research*, *85*(5), 387–390. https://doi.org/10.2175/106143013X13596524516707

Barthès, M., Mazue, G., Bonnet, D., Viennet, R., Hihn, J.-Y., & Bailly, Y. (2015). Characterization of the activity of ultrasound emitted in a perpendicular liquid flow using Particle Image Velocimetry (PIV) and electrochemical mass transfer measurements. *Ultrasonics*, *59*, 72–78. https://doi.org/10.1016/j.ultras.2015.01.015

Basnet, C. B., & Panthi, K. K. (2018). Analysis of unlined pressure shafts and tunnels of selected Norwegian hydropower projects. *Journal of Rock Mechanics and Geotechnical Engineering*, *10*(3), 486–512. https://doi.org/10.1016/j.jrmge.2017.12.002

Battaglia, J., & Fleming, R. W. (1987). *Method of vacuum degassing and refilling a reactor coolant system* (US 4647425).

Battino, R., & Seybold, P. G. (2011). The O2/N2 Ratio Gas Solubility Mystery. *Journal of Chemical & Engineering Data*, *56*(12), 5036–5044. https://doi.org/10.1021/je200878w

Berg, A. (1987). Supersaturation of dissolved air in the waterways of hydroelectric power plants - review and examples, 745–756.

Berg, A. (1992). Air entrainment and supersaturation of dissolved air in a shaft under atmospherical and reduced pressure conditions. *Journal of Hydraulic Research*, *30*(3), 327–340. https://doi.org/10.1080/00221689209498922

Berg, A., McClimans, T., Rye, H., Tekle, T., & Wathne, M. (1984). Supersaturation of dissolved air in the waterways of hydroelectric power plants.

Berga, L. (2016). The Role of Hydropower in Climate Change Mitigation and Adaptation: A Review. *Engineering*, *2*(3), 313–318. https://doi.org/10.1016/J.ENG.2016.03.004

Bergh, H. (2012). Hydropower. In L. Bengtsson, R. W. Herschy & R. W. Fairbridge (Eds.), *Encyclopedia of lakes and reservoirs* (pp. 355–356). Springer Netherlands. https://doi.org/10.1007/978-1-4020-4410-6_206

Bhat, A. P., & Gogate, P. R. (2020). Cavitation-based pre-treatment of wastewater and waste sludge for improvement in the performance of biological processes: A review. *Journal of Environmental Chemical Engineering*. https://doi.org/10.1016/j.jece.2020.104743

Blanchard, R. (1924). Geographical Conditions of Water Power Development. *Geographical Review*, *14*(1), 88. https://doi.org/10.2307/208357

Botelho, A., Ferreira, P., Lima, F., Pinto, L. M. C., & Sousa, S. (2017). Assessment of the environmental impacts associated with hydropower. *Renewable and Sustainable Energy Reviews*, *70*, 896–904. https://doi.org/10.1016/j.rser.2016.11.271

Boyle, R. W. (1922). Cavitation in the Propagation of Sound. *Proceedings and transactions of the Royal Society of Canada*, *3*(16).

Brandt, M. J., Johnson, K. M., Elphinston, A. J., & Ratnayaka, D. D. (2017). Dams and Reservoirs. In *Twort's Water Supply* (pp. 159–204). Elsevier. https://doi.org/10.1016/B978-0-08-100025-0.00005-3

Breeze, P. (2018). *Hydropower*. Elsevier. https://doi.org/10.1016/C2016-0-03622-7

Brekke, H. (2015). *Hydraulic Turbines - Design, Erection and Operation*.

Campbell, J. (2015). Chapter 14 - melting. In J. Campbell (Ed.), *Complete casting handbook (second edition)* (Second Edition, pp. 769–796). Butterworth-Heinemann. https://doi.org/https://doi.org/10.1016/B978-0-444-63509-9.00014-5

Carr, J. J. (1993). *Sensors and circuits: Sensors, transducers, and supporting circuits for electronic instrumentation, measurement, and control*. PTR Prentice Hall.

CCME. (1999). *Canadian water quality guidelines for the protection of aquatic life: Dissolved gas supersaturation*. Canadian Council of Ministers of the Environment. Winnipeg, Canada.

Chapter 11 - equipment and equipment integration. (2012). In B. Rehm, A. Haghshenas, A. Paknejad, A. Al-Yami, J. Hughes & J. Schubert (Eds.), *Underbalanced drilling: Limits and extremes* (pp. 463–536). Gulf Publishing Company. https://doi.org/https://doi.org/10.1016/B978-1-933762-05-0.50018-8

Charmasson, J., Belsnes, M. M., Andersen, O., Eloranta, A., Graabak, I., Korpås, M., Helland, I., Sundt, H., & Wolfgang, O. (2018). *HydroBalance - Roadmap for large-scale balancing and energy storage from Norwegian hydropower*. SINTEF Energy Research. Trondheim, Norway.

Chatton, E., Labasque, T., de La Bernardie, J., Guihéneuf, N., Bour, O., & Aquilina, L. (2017). Field Continuous Measurement of Dissolved Gases with a CF-MIMS: Applications to the Physics and Biogeochemistry of Groundwater Flow [Publisher: American Chemical Society]. *Environmental Science & Technology*, *51*(2), 846–854. https://doi.org/10.1021/acs.est.6b03706

Chen, F., Zhang, M., & Yang, C.-h. (2020). Application of ultrasound technology in processing of ready-to-eat fresh food: A review. *Ultrasonics Sonochemistry*, *63*. https://doi.org/10.1016/j.ultsonch.2019.104953

Chen, Z., Feng, J., Li, R., Wang, Y., Peng, F., & Li, K. (2022). Field observation and numerical modelling of supersaturated dissolved gas at river confluence. *Ecological Modelling*, *471*. https://doi.org/10.1016/j.ecolmodel.2022.110017

Colt, J. (1984). Computation of dissolved gas concentrations in water as functions of temperature, salinity, and pressure.

Crawford, S., Korpiel, J., & Velastegui, O. (2017). Degasification by Absorption-Based Gas Stripping. *SPE Annual Technical Conference and Exhibition*. https://doi.org/10.2118/187389-MS

Crum, L. (1984). Rectified diffusion. *Ultrasonics*, *22*(5), 215–223. https://doi.org/10.1016/0041-624X(84)90016-7

Crum, L. A. (1982). Nucleation and stabilization of microbubbles in liquids. *Applied Scientific Research*, *38*(1), 101–115. https://doi.org/10.1007/BF00385941

CUP. (2023a). *Definition of catchment area from the Cambridge Advanced Learner's Dictionary & Thesaurus*. Cambridge University Press. Retrieved August 3, 2023, from https://dictionary.cambridge.org/dictionary/english/catchment-area

CUP. (2023b). *Definition of concentration from the Cambridge Advanced Learner's Dictionary & Thesaurus*. Cambridge University Press. Retrieved August 3, 2023, from https://dictionary.cambridge.org/dictionary/english/concentration

CUP. (2023c). *Definition of discharge from the Cambridge Advanced Learner's Dictionary & Thesaurus*. Cambridge University Press. Retrieved August 3, 2023, from https://dictionary.cambridge.org/dictionary/english/discharge

CUP. (2023d). *Definition of mean from the Cambridge Advanced Learner's Dictionary & Thesaurus*. Cambridge University Press. Retrieved August 11, 2023, from https://dictionary.cambridge.org/dictionary/english/mean

CUP. (2023e). *Definition of median from the Cambridge Academic Content Dictionary*. Cambridge University Press. Retrieved August 11, 2023, from https://dictionary.cambridge.org/dictionary/english/median

CUP. (2023f). *Definition of saturation from the Cambridge Advanced Learner's Dictionary & Thesaurus*. Cambridge University Press. Retrieved August 3, 2023, from https://dictionary.cambridge.org/dictionary/english/saturation

CUP. (2023g). *Definition of tidal power from the Cambridge Advanced Learner's Dictionary & Thesaurus*. Cambridge University Press. Retrieved August 3, 2023, from https://dictionary.cambridge.org/dictionary/english/tidal-power

D'Aoust, B. G. (2007). Technical Note: Total Dissolved Gas Pressure (TDGP) Sensing in the Laboratory. *Dissolution Technologies*, *14*(2), 38–41. https://doi.org/10.14227/DT140207P38

Davenport, M. T., Timmons, M. B., Vinci, B. J., & Crum, M. K. (2001). Experimental evaluation of low head oxygenators. *Aquacultural Engineering*, *24*(4), 245–256. https://doi.org/10.1016/S0144-8609(01)00065-6

De Faria, F. A., Davis, A., Severnini, E., & Jaramillo, P. (2017). The local socio-economic impacts of large hydropower plant development in a developing country. *Energy Economics*, *67*, 533–544. https://doi.org/10.1016/j.eneco.2017.08.025

Department of Water Affairs and Forestry. (1996). *South African Water Quality Guidelines* (S. Holmes, Ed.; 2nd ed, Vol. 7).

Dixon, S. L., & Hall, C. A. (2014). *Fluid mechanics and thermodynamics of turbomachinery* (Seventh edition). Butterworth-Heinemann is an imprint of Elsevier.

Dokulil, M. T., de Eyto, E., Maberly, S. C., May, L., Weyhenmeyer, G. A., & Woolway, R. I. (2021). Increasing maximum lake surface temperature under climate change. *Climatic Change*, *165*(3-4). https://doi.org/10.1007/s10584-021-03085-1

Ehsani, N., Vörösmarty, C. J., Fekete, B. M., & Stakhiv, E. Z. (2017). Reservoir operations under climate change: Storage capacity options to mitigate risk. *Journal of Hydrology*, *555*, 435–446. https://doi.org/10.1016/j.jhydrol.2017.09.008

EIB. (2019). *Environmental, Climate and Social Guidelines on Hydropower Development*. European Investment Bank. Luxembourg.

Ellefsrød, T., Kobro, E., & Glawing, H. Å. (2016). *Nordic Grid - FNR Frequency Containment*. Norconsult AS. Larvik.

Ellens, N., & Hynynen, K. (2015). High-intensity focused ultrasound for medical therapy. In *Power Ultrasonics* (pp. 661–693). Elsevier. https://doi.org/10.1016/B978-1-78242-028-6.00022-3

Eller, A., & Flynn, H. G. (1965). Rectified Diffusion during Nonlinear Pulsations of Cavitation Bubbles. *The Journal of the Acoustical Society of America*, *37*(493). https://doi.org/https://doi.org/10.1121/1.1909357

Elliot Company. (1923). *Conquering Corrosion*. Elliot Company. Pittsburgh PA.

Escudier, M., & Atkins, T. (2019). *A Dictionary of Mechanical Engineering* (2nd ed.). Oxford University Press. https://doi.org/10.1093/acref/9780198832102.001.0001

Eskin, D. (2015). Ultrasonic degassing of liquids. In *Power Ultrasonics* (pp. 611–631). Elsevier. https://doi.org/10.1016/B978-1-78242-028-6.00020-X

Eskin, D. G. (2017). Overview of Ultrasonic Degassing Development [Series Title: The Minerals, Metals & Materials Series]. In A. P. Ratvik (Ed.), *Light Metals 2017* (pp. 1437–1443). Springer International Publishing. https://doi.org/10.1007/978-3-319-51541-0_171

Fair, J. R., & Kister, H. Z. (2003). Absorption (Chemical Engineering). In *Encyclopedia of Physical Science and Technology* (pp. 1–25). Elsevier. https://doi.org/10.1016/B0-12-227410-5/00001-6

Fickeisen, D. H., M. J. Schneider, Schneider, M. J., J. C. Montgomery & Montgomery, J. C. (1975). A Comparative Evaluation of the Weiss Saturometer. *Transactions of The American Fisheries Society*, *104*(4), 816–820. https://doi.org/10.1577/1548-8659(1975)104<816:aceotw>2.0.co;2

Gallego-Juárez, J., & Graff, K. (2015). Introduction to power ultrasonics. In *Power Ultrasonics* (pp. 1–6). Elsevier. https://doi.org/10.1016/B978-1-78242-028-6.00001-6

Garcia-Ochoa, F., & Gomez, E. (2009). Bioreactor scale-up and oxygen transfer rate in microbial processes: An overview. *Biotechnology Advances*, *27*(2), 153–176. https://doi.org/10.1016/j.biotechadv.2008.10.006

Geist, D. R., Linley, T. J., Cullinan, V., & Deng, Z. (2013). The Effects of Total Dissolved Gas on Chum Salmon Fry Survival, Growth, Gas Bubble Disease, and Seawater Tolerance. *North American Journal of Fisheries Management*, *33*(1), 200–215. https://doi.org/10.1080/02755947.2012.750634

Goldman, D. E., & Ringo, G. R. (1949). Determination of Pressure Nodes in Liquids. *The Journal of the Acoustical Society of America*, *21*(3). https://doi.org/10.1121/1.1906507

Gondrexon, N., Renaudin, V., Boldo, P., Gonthier, Y., Bernis, A., & Pettier, C. (1997). Degassing effect and gas-liquid transfer in a high frequency sonochemical reactor. *Chemical Engineering Journal*, *66*(1), 21–26. https://doi.org/10.1016/S1385-8947(96)03124-5

Gorham, F. P. (1899). The Gas Bubble Disease of Fish and its Cause.

Görtz, J., Aouad, M., Wieprecht, S., & Terheiden, K. (2022). Assessment of pumped hydropower energy storage potential along rivers and shorelines. *Renewable and Sustainable Energy Reviews*, *165*, 112027. https://doi.org/10.1016/j.rser.2021.112027

Gøtske, E. K., & Victoria, M. (2021). Future operation of hydropower in Europe under high renewable penetration and climate change. *iScience*, *24*(9). https://doi.org/10.1016/j.isci.2021.102999

Graabak, I., Jaehnert, S., Korpås, M., & Mo, B. (2017). Norway as a Battery for the Future European Power System—Impacts on the Hydropower System. *Energies*, *10*(12). https://doi.org/10.3390/en10122054

Gramer, G., & Korn, R. (1974). *Thermal degassing of the primary coolant of nuclear reactors* (U.S. Patent No 3,789,577). Washington, DC.

Gullberg, A. T. (2013). The political feasibility of Norway as the 'green battery' of Europe. *Energy Policy*, *57*, 615–623. https://doi.org/10.1016/j.enpol.2013.02.037

Gütle, V. (2021). *How to avoid gas supersaturation in the river downstream a hydro power plant* [Master's thesis, Norwegian University of Science and Technology].

Hagemann, S., Chen, C., Clark, D. B., Folwell, S., Gosling, S. N., Haddeland, I., Hanasaki, N., Heinke, J., Ludwig, F., Voss, F., & Wiltshire, A. J. (2013).

Climate change impact on available water resources obtained using multiple global climate and hydrology models. *Earth System Dynamics*, *4*(1), 129–144. https://doi.org/10.5194/esd-4-129-2013

Hansen, B. K. T. (2018). *Flood dampening in hydropower systems* [Master's thesis, NTNU].

Hansen, B. B., Isaksen, K., Benestad, R. E., Kohler, J., Pedersen, Å. Ø., Loe, L. E., Coulson, S. J., Larsen, J. O., & Varpe, Ø. (2014). Warmer and wetter winters: Characteristics and implications of an extreme weather event in the High Arctic. *Environmental Research Letters*, *9*(11). https://doi.org/10.1088/1748-9326/9/11/114021

Hansen, H. E., Seland, F., Sunde, S., Burheim, O. S., & Pollet, B. G. (2021). Two routes for sonochemical synthesis of platinum nanoparticles with narrow size distribution. *Materials Advances*, *2*, 1962–1971. https://doi.org/10.1039/D0MA00909A

Hanssen-Bauer, I., Førland, E. J., Haddeland, I., Hisdal, H., Lawrence, D., Mayer, Nesje, A., Nilsen, J. E. Ø., Sandven, S., Sandø, A. B., Sorteberg, A., & Ådlandsvik, B. (2017). *Climate in Norway 2100 – a knowledge base for climate adaptation* (NCCS report No. 1/2017). Norwegian Environment Agency. Norway.

Harvey, E. N., Barnes, D. K., McElroy, W. D., Whiteley, A. H., & Pease, D. C. (1945). Removal of Gas Nuclei from Liquids and Surfaces. *Journal of the American Chemical Society*, *67*(1), 156–157. https://doi.org/10.1021/ja01217a505

Heggberget, T. G. (1984). Effect of supersaturated water on fish in the River Nidelva, southern Norway. *Journal of Fish Biology*, *24*(1), 65–74. https://doi.org/10.1111/j.1095-8649.1984.tb04777.x

Heggstad, R., & Thorsnæs, G. (2023). Otra. *Store norske leksikon*. Retrieved July 6, 2023, from https://snl.no/Otra

Henry, W. (1803). III. Experiments on the Quantity of Gases absorbed by Water, at different Temperatures, and under different Pressures. *Philosophical Transactions of the Royal Society*, *93*, 29–274. https://doi.org/http://doi.org/10.1098/rstl.1803.0004

Hihn, J.-Y. (1992). *Contribution a l'etude d'un lit fluidise triphasique inverse fonctionnant a contre-courant: Hydrodynamique et transfert de matiere gaz/liquide* [PhD]. Université de Savoie.

Hihn, J.-Y., Doche, M.-L., Hallez, L., Taouil, A. E., & Pollet, B. G. (2018). Sono-electrochemistry: Both a Tool for Investigating Mechanisms and for Accelerating Processes. *The Electrochemical Society Interface*, *27*(3), 47–51. https://doi.org/10.1149/2.F05183if

Hihn, J.-Y., Doche, M.-L., Mandroyan, A., Hallez, L., & Pollet, B. (2011). Respective contribution of cavitation and convective flow to local stirring in sonoreactors. *Ultrasonics Sonochemistry*, *18*(4), 881–887. https://doi.org/10.1016/j.ultsonch.2011.02.006

Ho, D., Kim, K., Earmme, T., & Kim, C. (2020). Enhancing gas–liquid volumetric mass transfer coefficient. *Journal of Industrial and Engineering Chemistry*, *87*, 1–17. https://doi.org/10.1016/j.jiec.2020.03.009

Huang, J., Li, R., Feng, J., Xu, W., & Wang, L. (2016). Relationship investigation between the dissipation process of supersaturated total dissolved gas and wind effect. *Ecological Engineering*, *95*, 430–437. https://doi.org/10.1016/j.ecoleng.2016.06.042

Huang, X., Li, K.-f., Du, J., & Li, R. (2010). Effects of gas supersaturation on lethality and avoidance responses in juvenile rock carp (Procypris rabaudi Tchang). *Journal of Zhejiang University SCIENCE B*, *11*(10), 806–811. https://doi.org/10.1631/jzus.B1000006

HydroGroup. (2018). *Processes for degassing - Feedwater treatment*. RWT GmbH.

IHA. (2022). *2022 Hydropower Status Report*. International Hydropower Association. United Kingdom. https://www.hydropower.org/publications/2022-hydropower-status-report

Innovation Norway. (2023). How Norway produces hydropower with a minimal carbon footprint. *Business Norway*. Retrieved October 4, 2023, from https://businessnorway.com/articles/how-norway-produces-hydropower-with-a-minimal-carbon-footprint

IPCC. (2013). *Climate Change 2013: The Physical Science Basis. Contribution of Working Group I to the Fifth Assessment Report of the Intergovernmental Panel on Climate Change* (T. Stocker, D. Qin, G.-K. Plattner, M. Tignor, S. Allen, J. Boschung, A. Nauels, Y. Xia, V. Bex & P. Midgley, Eds.). Cambridge University Press.

IPCC. (2023). Summary for Policymakers. In *Climate Change 2023: Synthesis Report. Contribution of Working Groups I, II and III to the Sixth Assessment Report of the Intergovernmental Panel on Climate Change [Core Writing Team, H. Lee and J. Romero (eds.)]* (pp. 1–34). Intergovernmental Panel on Climate Change. Geneva, Switzerland. https://doi.org/10.59327/IPCC/AR6-9789291691647

ISO. (2017). *Hydrometry — open channel flow measurement using thin-plate weirs* (ISO Standard No. No. 1438:2017). International Organization for Standardization.

J. Glover, B. (2022). Planning Run-of-the-River Hydropower in Mountain Regions. In *Comprehensive Renewable Energy* (pp. 65–83). Elsevier. https://doi.org/10.1016/B978-0-12-819727-1.00071-6

Jensen, T., Stensby, K. E., Thaulow, H., Knutsen, T., Gjermundsen, T., & Killingtveit, Å. (2022). Hydropower in Norway. In *Comprehensive Renewable Energy* (pp. 358–389). Elsevier. https://doi.org/10.1016/B978-0-12-819727-1.00165-5

Jiang, J., & Ma, G. (2021). Dissolved Gases Detection with Optical Methods [Conference Name: Optical Sensing in Power Transformers]. In *Optical Sensing in Power Transformers* (pp. 65–135). IEEE. https://doi.org/10.1002/9781119765325.ch4

Jie, L., Peng, L., Xiajie, L., Wei, Z., Yonghong, L., Qing, L., Zhan, L., Yanbin, Z., Yongzhi, L., Feng, L., Tengjiao, W., Yanwei, Z., Dongsheng, Z., Mingzhou, C., & Wenyuan, X. (2013). *Degasser for removing dissolved gases in reactor coolant of nuclear power station, and method thereof* (CN103405945A).

Jjunju, E., Killingtveit, Å., & Hamududu, B. (2022). Hydropower and Climate Change. In *Comprehensive Renewable Energy* (pp. 259–283). Elsevier. https://doi.org/10.1016/B978-0-12-819727-1.00111-4

Jones, S. F., Evans, G. M., & Galvin, K. P. (1999). Bubble nucleation from gas cavities - a review. *Advances in Colloid and Interface Science*, *80*(1), 27–50. https://doi.org/10.1016/S0001-8686(98)00074-8

Kamal, R., Zhu, D. Z., Crossman, J. A., & Leake, A. (2020). Case Study of Total Dissolved Gas Transfer and Degasification in a Prototype Ski-Jump Spillway. *Journal of Hydraulic Engineering*, *146*(9). https://doi.org/10.1061/(ASCE)HY.1943-7900.0001801

Kamal, R., Zhu, D. Z., Leake, A., & Crossman, J. A. (2019). Dissipation of Supersaturated Total Dissolved Gases in the Intermediate Mixing Zone of a Regulated River. *Journal of Environmental Engineering*, *145*(2). https://doi.org/10.1061/(ASCE)EE.1943-7870.0001477

Kamal, R., Zhu, D. Z., McArthur, M., & Leake, A. (2016). Field Study on the Dissipation of Supersaturated Total Dissolved Gases in a Cascade Reservoir System, 452–460. https://doi.org/10.1061/9780784479872.046

Kapit, J., & Michel, A. P. (2021). Measurement of Dissolved Gases Using a Hollow Core Optical Fiber and Capillary Membrane Inlet. *2021 Conference on Lasers and Electro-Optics (CLEO)*, 1–2.

Kapustina, O. (1973). Degassing of liquids. In *Physical Principles of Ultrasonic Technology* (pp. 378–509). Springer US. https://doi.org/10.1007/978-1-4684-8217-1

Kiljański, T., & Dziubiński, M. (2001). Centrifugal degassing of highly viscous newtonian liquids. *The Canadian Journal of Chemical Engineering*, *79*(3), 449–454. https://doi.org/10.1002/cjce.5450790319

Killingtveit, Å. (2019). Hydropower. In *Managing Global Warming* (pp. 265–315). Elsevier. https://doi.org/10.1016/B978-0-12-814104-5.00008-9

Komarov, S. V., Kuwabara, M., & Abramov, O. V. (2005). High Power Ultrasonics in Pyrometallurgy: Current Status and Recent Development. *ISIJ International*, *45*(12), 1765–1782. https://doi.org/10.2355/isijinternational.45.1765

Kreyling, J., Grant, K., Hammerl, V., Arfin-Khan, M. A. S., Malyshev, A. V., Peñuelas, J., Pritsch, K., Sardans, J., Schloter, M., Schuerings, J., Jentsch, A., & Beierkuhnlein, C. (2019). Winter warming is ecologically more relevant than summer warming in a cool-temperate grassland. *Scientific Reports*, *9*(1). https://doi.org/10.1038/s41598-019-51221-w

Krogh, A. (2023). *Snazzy Maps - Free Styles for Google Maps*. Retrieved July 7, 2023, from http://snazzymaps.com

Kumar, A., Gogate, P. R., Pandit, A. B., Delmas, H., & Wilhelm, A. M. (2004). Gas-Liquid Mass Transfer Studies in Sonochemical Reactors. *Industrial & Engineering Chemistry Research*, *43*(8), 1812–1819. https://doi.org/10.1021/ie0341146

Kumar, A. (2022). Small Hydro. In *Comprehensive Renewable Energy* (pp. 30–64). Elsevier. https://doi.org/10.1016/B978-0-12-819727-1.00070-4

Kuttruff, H. (1962). *Über den Zusammenhang zwischen der Sonolumineszenz und der Schwingungskavitation in Flüssigkeiten* [PhD]. Universitet Göttingen.

Laugier, F., Andriantsiferana, C., Wilhelm, A., & Delmas, H. (2008). Ultrasound in gas–liquid systems: Effects on solubility and mass transfer. *Ultrasonics Sonochemistry*, *15*(6), 965–972. https://doi.org/10.1016/j.ultsonch.2008.03.003

Lauterborn, W., & Mettin, R. (2015). Acoustic cavitation. In *Power Ultrasonics* (pp. 37–78). Elsevier. https://doi.org/10.1016/B978-1-78242-028-6.00003-X

Lehner, B., Czisch, G., & Vassolo, S. (2005). The impact of global change on the hydropower potential of Europe: A model-based analysis. *Energy Policy*, *33*(7), 839–855. https://doi.org/10.1016/j.enpol.2003.10.018

Leighton, T. G. (1994). *The acoustic bubble*. Acad. Press.

Lennox, R. J., Thiemer, K., Vollset, K. W., Pulg, U., Stranzl, S., Nilsen, C. I., Haugen, T. O., & Velle, G. (2022). Behavioural response of brown trout (*Salmo trutta*) to total dissolved gas supersaturation in a regulated river. *Ecohydrology*, *15*(1). https://doi.org/10.1002/eco.2363

Leong, T., Ashokkumar, M., & Kentish, S. (2011). The Fundamentals of Power Ultrasound – a Review. *Acoustics Australia*.

Li, F., Zhang, X., Tian, H., Hu, J., Chen, S., Mo, R., Wang, C., & Guo, J. (2022a). Interactions of bubbles in acoustic Lichtenberg figure. *Ultrasonics Sonochemistry*, *87*. https://doi.org/10.1016/j.ultsonch.2022.106057

Li, P., Zhu, D. Z., Li, R., Wang, Y., Crossman, J. A., & Kuhn, W. L. (2022b). Production of total dissolved gas supersaturation at hydropower facilities and its transport: A review. *Water Research*, *223*. https://doi.org/10.1016/j.watres.2022.119012

Lighthill, S. J. (1978). Acoustic streaming. *Journal of Sound and Vibration*, *61*(3), 391–418. https://doi.org/10.1016/0022-460X(78)90388-7

Lindström, O. (1955). Physico-Chemical Aspects of Chemically Active Ultrasonic Cavitation in Aqueous Solutions. *The Journal of the Acoustical Society of America*, *27*(4), 654–671. https://doi.org/10.1121/1.1907987

Liu, L., Yang, Y., Liu, P., & Tan, W. (2014). The influence of air content in water on ultrasonic cavitation field. *Ultrasonics Sonochemistry*, *21*(2), 566–571. https://doi.org/10.1016/j.ultsonch.2013.10.007

Louisnard, O. (2017). A viable method to predict acoustic streaming in presence of cavitation. *Ultrasonics Sonochemistry*, *35*, 518–524. https://doi.org/10.1016/j.ultsonch.2016.09.013

Louisnard, O. (2023). Bubble dynamics and cavitation. [Presentation at the International School in Sonochemistry]. *Institut de Chimie Séparative de Marcoule, France*.

Louisnard, O., & Gomez, F. (2003). Growth by rectified diffusion of strongly acoustically forced gas bubbles in nearly saturated liquids. *Physical Review E*, *67*(3). https://doi.org/10.1103/PhysRevE.67.036610

Lu, J. X., Tupper, C., & Murray, J. (2023). Biochemistry, Dissolution and Solubility. In *StatPearls*. StatPearls Publishing.

Lund, M., & Heggberget, T. G. (1985). Avoidance response of two-year-old rainbow trout, Salmo gairdneri Richardson, to air-supersaturated water: Hydrostatic compensation. *Journal of Fish Biology*, *26*(2), 193–200. https://doi.org/10.1111/j.1095-8649.1985.tb04256.x

Ma, Q., Li, R., Feng, J., & Wang, L. (2013). Relationships between Total Dissolved Gas and Dissolved Oxygen in Water. *Fresenius Environmental Bulletin*, *22*(11).

Mahamuni, N. N., & Adewuyi, Y. G. (2010). Advanced oxidation processes (AOPs) involving ultrasound for waste water treatment: A review with emphasis

on cost estimation. *Ultrasonics Sonochemistry*, *17*(6), 990–1003. https://doi.org/10.1016/j.ultsonch.2009.09.005

Maluta, F., Alberini, F., Paglianti, A., & Montante, G. (2023). Hydrodynamics, power consumption and bubble size distribution in gas-liquid stirred tanks. *Chemical Engineering Research and Design*, *194*, 582–596. https://doi.org/10.1016/j.cherd.2023.05.006

Mandroyan, A., Doche, M., Hihn, J., Viennet, R., Bailly, Y., & Simonin, L. (2009a). Modification of the ultrasound induced activity by the presence of an electrode in a sono-reactor working at two low frequencies (20 and 40 kHz). Part II: Mapping flow velocities by particle image velocimetry (PIV). *Ultrasonics Sonochemistry*, *16*(1), 97–104. https://doi.org/10.1016/j.ultsonch.2008.05.004

Mandroyan, A., Viennet, R., Bailly, Y., Doche, M.-L., & Hihn, J.-Y. (2009b). Modification of the ultrasound induced activity by the presence of an electrode in a sonoreactor working at two low frequencies (20 and 40 kHz). Part I: Active zone visualization by laser tomography. *Ultrasonics Sonochemistry*, *16*(1), 88–96. https://doi.org/10.1016/j.ultsonch.2008.05.003

Margulis, M., & Margulis, I. (2003). Calorimetric method for measurement of acoustic power absorbed in a volume of a liquid. *Ultrasonics Sonochemistry*, *10*(6), 343–345. https://doi.org/https://doi.org/10.1016/S1350-4177(03)00100-7

Marsh, M. C. (1908). Notes on the dissolved content of water in its effect on fish. *Bulletin of the Bureau of Fisheries*, *28*(2).

Marsh, M. C., & Gorham, F. P. (1905). *The gas disease in fish*. G.P.O. Washington, DC.

Mason, T. J. (1999). *Advances in sonochemistry. Vol. 5*. JAI Press.

Massey, B. (1989). *Mechanics of Fluids*. Springer US.

Mayer, S., Khasandi Kuya, E., Antonsen, K., Abegg, B., & Hanssen-Bauer, I. (2023). Warmer and wetter: Outlining climate services for snow-dependent tourism in Norway – The case of Lofoten. *Climate Services*, *32*. https://doi.org/10.1016/j.cliser.2023.100405

Mazue, G., Viennet, R., Hihn, J.-Y., Bonnet, D., Barthes, M., Bailly, Y., & Albaïna, I. (2015). Influence of a perpendicular liquid flow on a cleaning process using 20 kHz ultrasound: Characterization of the agitation at vicinity of the surface opposite to the transducer. *The Canadian Journal of Chemical Engineering*, *93*(2), 201–205. https://doi.org/10.1002/cjce.22079

McDermet, J. R. (1924). The Degasification of Water. *Journal - American Water Works Association*, *11*(1), 118–127. https://doi.org/10.1002/j.1551-8833.1924.tb14220.x

Merouani, S., Hamdaoui, O., Rezgui, Y., & Guemini, M. (2015). Modeling of ultrasonic cavitation as an advanced technique for water treatment. *Desalination and Water Treatment*, *56*(6), 1465–1475. https://doi.org/10.1080/19443994.2014.950994

Mettin, R., Luther, S., Ohl, C.-D., & Lauterborn, W. (1999). Acoustic cavitation structures and simulations by a particle model. *Ultrasonics Sonochemistry*, *6*(1-2), 25–29. https://doi.org/10.1016/S1350-4177(98)00025-X

Mettin, R., & Cairós, C. (2016). Bubble Dynamics and Observations. In *Handbook of Ultrasonics and Sonochemistry* (pp. 3–31). Springer Singapore. https://doi.org/10.1007/978-981-287-278-4_3

Mo, B., Helseth, A., & Warland, G. (2018). Modeling and Quantifying the Importance of Snow Storage Information for the Nordic Power System. *2018 15th International Conference on the European Energy Market (EEM)*, 1–5. https://doi.org/10.1109/EEM.2018.8469861

Motarjemi, M., & Jameson, G. (1978). Mass transfer from very small bubbles—the optimum bubble size for aeration. *Chemical Engineering Science*, *33*(11), 1415–1423. https://doi.org/10.1016/0009-2509(78)85190-2

Nebeker, A., Kenthauck, A., & Baker, F. (1979). Temperature and oxygen-nitrogen gas ratios affect fish survival in air-supersaturated water. *Water Research*, *13*(3), 299–303. https://doi.org/10.1016/0043-1354(79)90210-0

Neff, D. V. (2008). Degassing. In S. Viswanathan, D. Apelian, R. J. Donahue, B. DasGupta, M. Gywn, J. L. Jorstad, R. W. Monroe, M. Sahoo, T. E. Prucha & D. Twarog (Eds.), *Casting* (pp. 185–193, Vol. 15). ASM International. https://doi.org/10.31399/asm.hb.v15.a0005353

Neppiras, E. A. (1980). *Acoustic Cavitation* (Physics Report No. 3). North-Holland Publishing Company.

Nevers, A., Hallez, L., Touyeras, F., & Hihn, J.-Y. (2018). Effect of ultrasound on silver electrodeposition: Crystalline structure modification. *Ultrasonics Sonochemistry*, *40*, 60–71. https://doi.org/10.1016/j.ultsonch.2017.02.033

Nomura, H., & Koda, S. (2015). What Is Sonochemistry? In *Sonochemistry and the Acoustic Bubble* (pp. 1–9). Elsevier. https://doi.org/10.1016/B978-0-12-801530-8.00001-3

NVE. (2017). *Overview of Norway's Electricity History* (No. 15). Norges vassdrags- og energidirektorat. Oslo, Norway.

NVE. (2023). *Vannkraft* [Norges vassdrags- og energidirektorat]. Retrieved May 5, 2023, from https://www.nve.no/energi/energisystem/vannkraft/

Nyborg, W. L. (1953). Acoustic Streaming due to Attenuated Plane Waves. *The Journal of the Acoustical Society of America*, *25*(1), 68–75. https://doi.org/10.1121/1.1907010

OED. (2023). *Electricity production* [Olje- og energidepartementet]. Retrieved October 20, 2023, from https://energifaktanorge.no/en/norsk-energiforsyning/kraftproduksjon/

O'Haver, T. (2023). *Pragmatic Introduction to Signal Processing*.

Orlins, J., & Gulliver, J. S. (2000). Dissolved gas supersaturation downstream of a spillway II: Computational model. *Journal of Hydraulic Research*, *38*(2), 151–159. https://doi.org/10.1080/00221680009498350

Otra Kraft DA. (2019). *Brokke Kraftverk*. Retrieved July 6, 2023, from https://www.otrakraft.no/kraftstasjonar/brokke-kraftverk-article357-1060.html

Ou, Y., Li, R., Tuo, Y., Niu, J., Feng, J., & Pu, X. (2016). The promotion effect of aeration on the dissipation of supersaturated total dissolved gas. *Ecological Engineering*, *95*, 245–251. https://doi.org/10.1016/j.ecoleng.2016.06.041

Ovelar, C., Takenobu, M., Dettmer, P., Andriolo, M., Aver, C., & Ota, J. (2022). Total dissolved gases (tdg) supersaturation reduction at colider dam: First spill with horizontal deflectors verification. *Revista Brasileira de Engenharia de Barragens*.

Pereira, G. M. (2021). *Design of Hydroelectric Power Plants – Step by Step* (1st ed.). CRC Press. https://doi.org/10.1201/9781003161325

Perzyna, S. (2017). *Air return in brook intake shafts* [Master's thesis, NTNU].

Pichler, W. (1996). *Untersuchung von Fliessgewässern im Bundeland Salzburg auf kommunale Belastungen* (UBA-BE-059). Umweltbundesamt. Wien, Austria.

Pitorac, L., Vereide, K., & Lia, L. (2020). Technical Review of Existing Norwegian Pumped Storage Plants. *Energies*, *13*(18). https://doi.org/10.3390/en13184918

Pitorac, L.-I. (2017). *Numerical simulation of air injection in Francis turbines* [Master's thesis, Norwegian University of Science and Technology].

Pleizier, N., Cooke, S. J., & Brauner, C. J. (2021a). A Simple Chamber Design for Calibrating Weiss Saturometers and Recommendations for Measuring

and Reporting Total Dissolved Gases. *Water Resources Research*, *57*(8). https://doi.org/10.1029/2020wr029083

Pleizier, N. K., Nelson, C., Cooke, S. J., & Brauner, C. J. (2019). Understanding gas bubble trauma in an era of hydropower expansion: How do fish compensate at depth? *Canadian Journal of Fisheries and Aquatic Sciences*, *77*(3), 556–563. https://doi.org/10.1139/cjfas-2019-0243

Pleizier, N. K., Rost-Komiya, B., Cooke, S. J., & Brauner, C. J. (2021b). The lack of avoidance of total dissolved gas supersaturation in juvenile rainbow trout. *Hydrobiologia*, *848*(20), 4837–4850. https://doi.org/10.1007/s10750-021-04676-w

Poe, W. A., & Mokhatab, S. (2017). Chapter 1 - introduction to natural gas processing plants. In W. A. Poe & S. Mokhatab (Eds.), *Modeling, control, and optimization of natural gas processing plants* (pp. 1–72). Gulf Professional Publishing. https://doi.org/https://doi.org/10.1016/B978-0-12-802961-9.00001-2

Politano, M., Lyons, T., Anderson, K., Parkinson, S., & Weber, L. (2016). Spillway Deflector Design Using Physical and Numerical Models [Publisher: USU Libraries]. *Hydraulic Structures and Water System Management. 6th IAHR International Symposium on Hydraulic Structures*, 417–427. https://doi.org/10.15142/T3470628160853

Pollet, B. G., & Ashokkumar, M. (2019). *Introduction to Ultrasound, Sonochemistry and Sonoelectrochemistry*. Springer International Publishing. https://doi.org/10.1007/978-3-030-25862-7

Pontoni, F., Creti, A., & Joëts, M. (2018). Economic and Environmental Implications of Hydropower Concession Renewals: A Case Study in Southern France: *Revue économique*, *Vol. 69*(2), 241–266. https://doi.org/10.3917/reco.pr2.0116

Pulg, U. (2021). Nytt om gassovermetning [Presentation at Fiskesymposium.]. *NORCE*.

Pulg, U., Isaksen, T. E., Velle, G., Stranzl, S., Espedal, E. O., Vollset, K. W., Bye-Ingebrigtsen, E., & Barlaup, B. T. (2018). *Gassovermetning i vassdrag-en kunnskapsoppsummering* (No. 312). Laboratorium for ferskvannsøkologi og innlandsfiske.

Pulg, U., Stranzl, S., Vollset, K. W., Barlaup, B. T., Olsen, E., Skår, B., & Velle, G. (2016). *Gassmetning i Otra nedenfor Brokke kraftverk*.

Pulg, U., Stranzl, S., Wagner, B., Flödl, P., & Hauer, C. (2020). Gasübersättigung in Flüssen? Messung, Ursachen und Auswirkungen – Ein internationales Forschungsprojekt untersucht Verbreitung und Umwelteffekte. *Österreichische Wasser- und Abfallwirtschaft*, *72*(3-4), 142–148. https://doi.org/10.1007/s00506-020-00655-y

Richards, W. T., & Loomis, A. L. (1927). The Chemical Effects of High Frequency Sound Waves I. A Preliminary Survey. *Journal of the American Chemical Society*, *49*(12), 3086–3100. https://doi.org/10.1021/ja01411a015

Rognerud, M. E., Solemslie, B. W., Islam, H., & Pollet, B. G. (2020). How to Avoid Total Dissolved Gas Supersaturation in Water from Hydropower Plants by Employing Ultrasound. *Journal of Physics: Conference Series*, *1608*. https://doi.org/10.1088/1742-6596/1608/1/012004

Rohland, K. M., Foust, J. M., Lewis, G. D., & Sigmon, J. C. (2010). Aerating Turbines for Duke Energy's New Bridgewater Powerhouse. *Hydro Review*, *29*, 58–64.

Roy, S. M., Tanveer, M., & Machavaram, R. (2022). Applications of gravity aeration system in aquaculture—a systematic review. *Aquaculture International*, *30*(3), 1593–1621. https://doi.org/10.1007/s10499-022-00851-5

Rzechowicz, M., & Pashley, R. (2006). A membrane method for degassing non-aqueous liquids. *Journal of Colloid and Interface Science*, *298*(1), 321–326. https://doi.org/10.1016/j.jcis.2005.12.001

Sajjadi, B., Asgharzadehahmadi, S., Asaithambi, P., Raman, A. A. A., & Parthasarathy, R. (2017). Investigation of mass transfer intensification under power ultrasound irradiation using 3D computational simulation: A comparative analysis. *Ultrasonics Sonochemistry*, *34*, 504–518. https://doi.org/10.1016/j.ultsonch.2016.06.026

Santos, R. M., François, D., Mertens, G., Elsen, J., & Van Gerven, T. (2013). Ultrasound-intensified mineral carbonation. *Applied Thermal Engineering*, *57*(1-2), 154–163. https://doi.org/10.1016/j.applthermaleng.2012.03.035

Schade, H., Kunz, E., Kameier, F., & Paschereit, C. O. (2013). *Strömungslehre*. De Gruyter. https://doi.org/10.1515/9783110292237

Scharlin, P., Battino, R., Silla, E., Tuñón, I., & Pascual-Ahuir, J. L. (1998). Solubility of gases in water: Correlation between solubility and the number of water molecules in the first solvation shell. *Pure and Applied Chemistry*, *70*(10), 1895–1904. https://doi.org/10.1351/pac199870101895

Schelter, M., Zosel, J., Oelßner, W., & Mertig, M. (2014). A novel method for measuring dissolved gases in liquids. *Sensors and Actuators B: Chemical*, *193*, 113–120. https://doi.org/10.1016/j.snb.2013.11.070

Schneider, M. L., & Barko, K. (2006). *Total Dissolved Gas Characterization of the Lower Columbia River below Bonneville Dam*. U.S. Army Corps of Engineers.

Shen, X., Liu, S., Li, R., & Ou, Y. (2014). Experimental study on the impact of temperature on the dissipation process of supersaturated total dissolved gas. *Journal of Environmental Sciences*, *26*(9), 1874–1878. https://doi.org/10.1016/j.jes.2014.02.002

Shriver, D. F., & Drezdzon, M. A. (1986). *The manipulation of air-sensitive compounds* (2nd ed). Wiley.

Singh, R. (2015). Water and Membrane Treatment. In *Membrane Technology and Engineering for Water Purification* (pp. 81–178). Elsevier. https://doi.org/10.1016/B978-0-444-63362-0.00002-1

Skar, C., Jaehnert, S., Tomasgard, A., Midthun, K., & Fodstad, M. (2018). *Norway's role as a flexibility provider in a renewable Europe*. Centre for Sustainable Energy Studies (CenSES). Trondheim, Norway.

Skorpen, A. N. (2018). *Impact from flexible operations on High Head Francis turbines* [Master's thesis, Norwegian University of Science and Technology].

Smalås, A. (2021). *Climate change impact on high latitude freshwater fish populations* [Dissertation]. The Arctic University of Norway.

SnowPure Water Technologies. (2023). *Membrane Degassing Technology O2 and CO2*. Retrieved June 29, 2023, from https://www.snowpure.com/technologies/membrane-degassing-technology-liqui-cel/

Sommers, G. L. (2004). Hydropower Resources. In *Encyclopedia of Energy* (pp. 325–332). Elsevier. https://doi.org/10.1016/B0-12-176480-X/00339-9

Sörensen, C. (1936). Absorptions-, Geschwindigkeits- und Entgasungsmessungen im Ultraschallgebiet. *Annalen der Physik*, *418*(2), 121–137. https://doi.org/10.1002/andp.19364180204

Steel Melt Processing. (2008). In S. Viswanathan, D. Apelian, R. J. Donahue, B. DasGupta, M. Gywn, J. L. Jorstad, R. W. Monroe, M. Sahoo, T. E. Prucha & D. Twarog (Eds.), *Casting* (pp. 206–229, Vol. 15). ASM International. https://doi.org/10.31399/asm.hb.v15.a0005199

Stokkebø, O., Berdal, B., Brox, G., Fleischer, E., Guttormsen, O., Kjeldsen, A., & Tvinnereim, K. (1988). *Bekkeinntak på kraftverkstunneler.* (2nd edition). Vassdragsregulantenes forening. Asker.

Swinnerton, J. W., Linnenbom, V. J., & Cheek, C. H. (1962). Determination of Dissolved Gases in Aqueous Solutions by Gas Chromatography. [Publisher: American Chemical Society]. *Analytical Chemistry*, *34*(4), 483–485. https://doi.org/10.1021/ac60184a010

TETRA Technologies Inc. (2023). *Scavengers - Oxygen & CO2 Scavengers*. Retrieved June 26, 2023, from https://tetratec.com/oil-and-g

as-services/completion-fluids-additives/corrosion-control/scavengers/

Theerthagiri, J., Madhavan, J., Lee, S. J., Choi, M. Y., Ashokkumar, M., & Pollet, B. G. (2020). Sonoelectrochemistry for energy and environmental applications. *Ultrasonics Sonochemistry*, *63*. https://doi.org/10.1016/j.ultsonch.2020.104960

Touyeras, F., Hihn, J., Bourgoin, X., Jacques, B., Hallez, L., & Branger, V. (2005). Effects of ultrasonic irradiation on the properties of coatings obtained by electroless plating and electro plating. *Ultrasonics Sonochemistry*, *12*(1-2), 13–19. https://doi.org/10.1016/j.ultsonch.2004.06.002

TPWD. (2023). *Glossary of River Terminology* [Texas Parks and Wildlife Department]. Retrieved August 4, 2023, from http://www.texasthestateofwater.org/screening/html/gloassary.htm

Tribe, L. A., Briens, C. L., & Margaritis, A. (1995). Determination of the volumetric mass transfer coefficient (kLa) using the dynamic "gas out-gas in" method: Analysis of errors caused by dissolved oxygen probes. *Biotechnology and Bioengineering*, *46*(4), 388–392. https://doi.org/10.1002/bit.260460412

Trujillo, F. J., & Knoerzer, K. (2011). A computational modeling approach of the jet-like acoustic streaming and heat generation induced by low frequency high power ultrasonic horn reactors. *Ultrasonics Sonochemistry*, *18*(6), 1263–1273. https://doi.org/10.1016/j.ultsonch.2011.04.004

Turner, S. W., Ng, J. Y., & Galelli, S. (2017). Examining global electricity supply vulnerability to climate change using a high-fidelity hydropower dam model. *Science of The Total Environment*, *590-591*, 663–675. https://doi.org/10.1016/j.scitotenv.2017.03.022

USDOE. (2012). *Deaerators in Industrial Steam Systems* (DOE/GO-102012-3399). Advanced Manufacturing Office, Office of Energy Efficiency and Renewable Energy, U.S. Department of Energy. Washington, DC.

USEPA. (1976). *Quality Criteria for Water 1976*. U.S. Environmental Protection Agency. Washington, DC.

USEPA. (1986). *Quality Criteria for Water 1986* (No. 440/5-86-001). U.S. Environmental Protection Agency. Washington, DC.

USEPA. (2021a). *Climate Change Indicators: Lake Temperature* (Reports and Assessments). U.S. Environmental Protection Agency. Retrieved January 17, 2023, from https://www.epa.gov/climate-indicators/climate-change-indicators-lake-temperature

USEPA. (2021b). *Seasonality and Climate Change: A Review of Observed Evidence in the United States* (430-R-21-002). U.S. Environmental Protection Agency.

van Vliet, M. T., Wiberg, D., Leduc, S., & Riahi, K. (2016). Power-generation system vulnerability and adaptation to changes in climate and water resources. *Nature Climate Change*, *6*(4), 375–380. https://doi.org/10.1038/nclimate2903

van Vliet, M. T., Franssen, W. H., Yearsley, J. R., Ludwig, F., Haddeland, I., Lettenmaier, D. P., & Kabat, P. (2013). Global river discharge and water temperature under climate change. *Global Environmental Change*, *23*(2), 450–464. https://doi.org/10.1016/j.gloenvcha.2012.11.002

Viennet, R., Ligier, V., Hihn, J., Bereziat, D., Nika, P., & Doche, M. (2004). Visualisation and electrochemical determination of the actives zones in an ultrasonic reactor using 20 and 500 kHz frequencies. *Ultrasonics Sonochemistry*, *11*(3-4), 125–129. https://doi.org/10.1016/j.ultsonch.2004.01.007

Wang, J., Guan, Y., Wu, L., Guan, X., Cai, W., Huang, J., Dong, W., & Zhang, B. (2021). Changing Lengths of the Four Seasons by Global Warming. *Geophysical Research Letters*, *48*(6). https://doi.org/10.1029/2020GL091753

Wang, L., Guo, E., Huang, Y., & Lu, B. (2009). Rotary impeller refinement of 7075Al alloy. *Rare Metals*, *28*(3), 309–312. https://doi.org/10.1007/s12598-009-0060-0

Wang, Z., Guo, K., Liu, H., Liu, C., Geng, Y., Lu, Z., Jiao, B., & Chen, D. (2020). Effects of bubble size on the gas–liquid mass transfer of bubble swarms with Sauter mean diameters of 0.38–4.88 mm in a co-current upflow bubble column. *Journal of Chemical Technology & Biotechnology*, *95*(11), 2853–2867. https://doi.org/10.1002/jctb.6445

Warneck, P., & Williams, J. (2012). *The Atmospheric Chemist's Companion: Numerical Data for Use in the Atmospheric Sciences*. Springer Netherlands. https://doi.org/10.1007/978-94-007-2275-0

Wasti, A., Ray, P., Wi, S., Folch, C., Ubierna, M., & Karki, P. (2022). Climate change and the hydropower sector: A global review. *WIREs Climate Change*, *13*(2). https://doi.org/10.1002/wcc.757

Weitkamp, D. E., & Katz, M. (1980). A Review of Dissolved Gas Supersaturation Literature.

Wilhelms, S. C., & Martin, S. K. (1992). Gas Transfer in Diffused Bubble Plumes. *Hydraulic Engineering: Saving a Threatened Resource — In Search of*

Solutions: Proceedings of the Hydraulic Engineering sessions at Water Forum '92.

Witt, A., Stewart, K., & Hadjerioua, B. (2017). Predicting Total Dissolved Gas Travel Time in Hydropower Reservoirs. *Journal of Environmental Engineering*, *143*(12). https://doi.org/10.1061/(ASCE)EE.1943-7870.0001281

World Bank Group. (2021). *World Bank Climate Change Knowledge Portal*. Retrieved May 4, 2023, from https://climateknowledgeportal.worldbank.org/

Wu, R., Shu, D., Sun, B., Wang, J., Li, F., Chen, H., & Lu, Y. (2005). Theoretical analysis and experimental study of spray degassing method. *Materials Science and Engineering: A*, *408*(1-2), 19–25. https://doi.org/10.1016/j.msea.2005.05.055

Yamamoto, T., Hatanaka, S.-i., & Komarov, S. V. (2019). Fragmentation of cavitation bubble in ultrasound field under small pressure amplitude. *Ultrasonics Sonochemistry*, *58*. https://doi.org/10.1016/j.ultsonch.2019.104684

Yasui, K. (2002). Influence of ultrasonic frequency on multibubble sonoluminescence. *The Journal of the Acoustical Society of America*, *112*(4), 1405–1413. https://doi.org/10.1121/1.1502898

Yasui, K. (2011). Fundamentals of Acoustic Cavitation and Sonochemistry. *Theoretical and Experimental Sonochemistry Involving Inorganic Systems, by Ashokkumar, Muthupandian, ISBN 978-90-481-3886-9. Springer Science+Business Media B.V., 2011, p. 1*. https://doi.org/10.1007/978-90-481-3887-6_1

Yasui, K. (2015). Dynamics of Acoustic Bubbles. In *Sonochemistry and the Acoustic Bubble* (pp. 41–83). Elsevier. https://doi.org/10.1016/B978-0-12-801530-8.00003-7

Yasui, K. (2018). *Acoustic Cavitation and Bubble Dynamics*. Springer International Publishing. https://doi.org/10.1007/978-3-319-68237-2

Yasui, K., Tuziuti, T., Lee, J., Kozuka, T., Towata, A., & Iida, Y. (2008). The range of ambient radius for an active bubble in sonoluminescence and sonochemical reactions. *The Journal of Chemical Physics*, *128*(18). https://doi.org/10.1063/1.2919119

Ye, L., Zhu, X., & Liu, Y. (2019). Numerical study on dual-frequency ultrasonic enhancing cavitation effect based on bubble dynamic evolution. *Ultrasonics Sonochemistry*, *59*. https://doi.org/10.1016/j.ultsonch.2019.104744

Yu, H., Mei, J., & Xie, J. (2022). New ultrasonic assisted technology of freezing, cooling and thawing in solid food processing: A review. *Ultrasonics Sono-*

chemistry, *90*. https://doi.org/https://doi.org/10.1016/j.ultsonch.2022.106185

Yuan, S., Li, C., Zhang, Y., Yu, H., Xie, Y., Guo, Y., & Yao, W. (2021). Ultrasound as an emerging technology for the elimination of chemical contaminants in food: A review. *Trends in Food Science & Technology*, *109*, 374–385. https://doi.org/10.1016/j.tifs.2021.01.048

Žák, Ž. A., Zedníková, Z. M., & Moucha, T. (2023). Local volumetric mass transfer coefficients in sections of multiple-impeller stirred tank reactors: Data analysis. *Chemical Engineering Research and Design*, *190*, 829–841. https://doi.org/10.1016/j.cherd.2023.01.001

Zarfl, C., Berlekamp, J., He, F., Jähnig, S. C., Darwall, W., & Tockner, K. (2019). Future large hydropower dams impact global freshwater megafauna. *Scientific Reports*, *9*(1). https://doi.org/10.1038/s41598-019-54980-8

Zhang, P., Liu, Q., Wang, Y., Zhu, D. Z., Liang, R., Qin, L., Li, R., Ji, Q., & Li, K. (2022). River habitat assessment and restoration in high dam flood discharge systems with total dissolved gas supersaturation. *Water Research*, *221*. https://doi.org/10.1016/j.watres.2022.118833

Zhang, Q., Dong, Z., Zhao, S., Liu, Z., & Chen, G. (2021). Ultrasound-assisted gas–liquid mass transfer process in microreactors: The influence of surfactant, channel size and ultrasound frequency. *Chemical Engineering Journal*, *405*. https://doi.org/10.1016/j.cej.2020.126720

Zhang, Y., Zhou, G., & Prosperetti, A. (2017). Bubbles as a Means for the Deaeration of Water Bodies. *Journal of Environmental Engineering*, *143*(8). https://doi.org/10.1061/(ASCE)EE.1943-7870.0001205

Zhong, X., Yu, J., Guo, X., & Saeed, M. (2018). Analysis of degassing time of pressurized water reactor pressurizer. *Nuclear Engineering and Design*, *328*, 301–308. https://doi.org/10.1016/j.nucengdes.2018.01.023

Appendix A
Additional resulting data

This appendix is used to list all the data that is displayed in figures only or just mentioned as average or mean values. It is meant to be a data storage for anyone willing to continue with the work the author started, or to allow for comparison with numerical models.

A.1 Data from natural degasification in a river.

Table A.1: Maximum measured TDG saturation level at different positions in the Otra river and corresponding calculated $k_L a$ values for TDG supersaturation events in 2012 and 2013.

Date	Maximum TDG saturation [%TDG]				Calculated $k_L a$ [s^{-1}]		
	Brokke	1.2 km	1.5 km	8.0 km	1.2 km	1.5 km	8.0 km
23.07.2012	169	126	N/A	120	$3.04 \cdot 10^{-4}$	N/A	$0.61 \cdot 10^{-4}$
03.08.2012	166	128	N/A	122	$2.87 \cdot 10^{-4}$	N/A	$0.68 \cdot 10^{-4}$
07.08.2012	171	136	N/A	121	$2.90 \cdot 10^{-4}$	N/A	$0.70 \cdot 10^{-4}$
28.08.2012	169	146	N/A	122	$2.41 \cdot 10^{-4}$	N/A	$0.85 \cdot 10^{-4}$
30.08.2012	169	136	N/A	120	$2.64 \cdot 10^{-4}$	N/A	$0.74 \cdot 10^{-4}$
11.09.2012	172	153	N/A	126	$2.12 \cdot 10^{-4}$	N/A	$0.75 \cdot 10^{-4}$
14.09.2012	173	163	N/A	124	$1.75 \cdot 10^{-4}$	N/A	$0.78 \cdot 10^{-4}$
18.10.2012	166	139	133	123	$2.21 \cdot 10^{-4}$	$1.97 \cdot 10^{-4}$	$0.71 \cdot 10^{-4}$
20.10.2012	169	147	149	125	$2.11 \cdot 10^{-4}$	$2.02 \cdot 10^{-4}$	$0.72 \cdot 10^{-4}$
10.11.2012	136	114	116	104	$5.33 \cdot 10^{-4}$	$3.69 \cdot 10^{-4}$	$1.27 \cdot 10^{-4}$
12.11.2012	131	118	118	107	$2.00 \cdot 10^{-4}$	$2.02 \cdot 10^{-4}$	$0.99 \cdot 10^{-4}$
14.11.2012	169	146	143	124	$2.09 \cdot 10^{-4}$	$1.90 \cdot 10^{-4}$	$0.76 \cdot 10^{-4}$
20.11.2012	171	154	150	126	$3.37 \cdot 10^{-4}$	$2.80 \cdot 10^{-4}$	$0.93 \cdot 10^{-4}$
26.11.2012	123	117	118	111	$1.09 \cdot 10^{-4}$	$0.78 \cdot 10^{-4}$	$0.60 \cdot 10^{-4}$
18.04.2013	146	131	122	119	$2.15 \cdot 10^{-4}$	$2.29 \cdot 10^{-4}$	$0.60 \cdot 10^{-4}$
05.08.2013	150	N/A	128	N/A	N/A	$2.48 \cdot 10^{-4}$	N/A
18.09.2013	141	N/A	124	N/A	N/A	$2.77 \cdot 10^{-4}$	N/A
28.10.2013	140	N/A	117	108	N/A	$3.34 \cdot 10^{-4}$	$1.24 \cdot 10^{-4}$
16.11.2013	170	N/A	138	121	N/A	$3.23 \cdot 10^{-4}$	$0.92 \cdot 10^{-4}$
16.12.2013	168	N/A	141	120	N/A	$1.69 \cdot 10^{-4}$	$0.88 \cdot 10^{-4}$

A.2 Additional data from experiments in the batch reactor.

A.2.1 Measurement data from equipment calibration.

Table A.2: Determination of the transmitted acoustic power of a ultrasonic transducer using the calorimetric method. The measurement values are averaged. A feedback giving the output power is only available from SinpTac's NexTgen software.

Transducer	Amplitude [%]	Output power [W]	Temperature slope [°C min^{-1}]
SinapTec	33	43.44	0.45
20 kHz horn	40	81.46	0.88
	60	177.07	1.97
	80	282.40	3.15
	100	396.72	4.32
Meinhardt Ultrasonics	20	N/A	0.10
40 kHz plate	40	N/A	0.24
	60	N/A	0.34
	80	N/A	0.42
	100	N/A	0.53
Meinhardt Ultrasonics	20	N/A	0.02
580 kHz plate	40	N/A	0.06
	60	N/A	0.23
	80	N/A	0.47
	100	N/A	0.66

Table A.3: Calibration of the flow circulation pumps. Measured values are averaged.

Pump	Setting [V]	Setting [cm^3 min]	Time [s]	Volume [cm^3]
Marco Fluidtech UP2/E	3	N/A	5	163.33
electronic gear pump	6	N/A	5	321.67
	9	N/A	5	445
	12	N/A	5	520
Shenchen M6-6L	N/A	500	21	100
peristaltic pump	N/A	800	12	100
	N/A	1600	7	100
	N/A	1700	6	100
	N/A	2500	4.75	100
	N/A	2750	4	100

A.2.2 Measurement data from parameter tests.

Table A.4: Measurement and $k_L a$ data during ultrasonic degasification. The respective acoustic power is calculated using the regression curves listed in Table 4.2.

Frequency [kHz]	Acoustic power [W]	Initial TDG saturation [%TDG]	$k_L a$ [s^{-1}]
20	35.83	107.90	$1.06 \cdot 10^{-3}$
	33.94	112.12	$1.06 \cdot 10^{-3}$
	99.95	110.68	$3.18 \cdot 10^{-3}$
	161.55	113.47	$14.80 \cdot 10^{-3}$
	190.98	116.85	$16.50 \cdot 10^{-3}$
	194.58	110.72	$19.99 \cdot 10^{-3}$
	243.63	112.07	$35.99 \cdot 10^{-3}$
	247.89	119.63	$21.61 \cdot 10^{-3}$
	290.48	114.90	$34.80 \cdot 10^{-3}$
	291.26	123.99	$42.69 \cdot 10^{-3}$
	302.07	119.15	$48.98 \cdot 10^{-3}$
	313.67	114.00	$42.04 \cdot 10^{-3}$
40	37.06	110.74	$0.83 \cdot 10^{-3}$
	37.06	111.75	$0.54 \cdot 10^{-3}$
580	47.27	110.59	$1.50 \cdot 10^{-3}$
	47.27	112.89	$3.08 \cdot 10^{-3}$

Table A.5: Measurement and $k_L a$ data during flow circulation. The cross-sectional flow velocities are calculated using the pump flow rate and the cross-sectional area of the batch reactor.

Flow direction	Cross-sectional flow velocity [cm s^{-1}]	Initial TDG saturation [%TDG]	$k_L a$ [s^{-1}]
Concurrent	0.22	113.26	$1.18 \cdot 10^{-3}$
	0.43	115.96	$0.94 \cdot 10^{-3}$
	0.65	113.85	$1.10 \cdot 10^{-3}$
	0.83	110.54	$2.20 \cdot 10^{-3}$
	1.66	113.81	$2.07 \cdot 10^{-3}$
	2.30	110.10	$1.48 \cdot 10^{-3}$
Countercurrent	0.65	112.49	$2.77 \cdot 10^{-3}$
	0.83	110.21	$2.15 \cdot 10^{-3}$
	1.66	110.42	$3.84 \cdot 10^{-3}$
	2.30	111.14	$4.09 \cdot 10^{-3}$
	2.69	109.88	$2.60 \cdot 10^{-3}$

Table A.6: Measurement and $k_L a$ data during gas bubbling.

Gas diffuser	Air flow rate [dm^3 min^{-1}]	Initial TDG saturation [%TDG]	$k_L a$ [s^{-1}]
Oxygenation stone	1	112.88	$0.50 \cdot 10^{-3}$
	2	115.70	$4.30 \cdot 10^{-3}$
	3	115.18	$5.55 \cdot 10^{-3}$
	4	110.67	$10.17 \cdot 10^{-3}$
	7	112.72	$11.03 \cdot 10^{-3}$
	10	110.20	$12.62 \cdot 10^{-3}$
Ace gas diffuser	1	110.29	$3.94 \cdot 10^{-3}$
	4	111.53	$7.03 \cdot 10^{-3}$
Synthetic tube	1	117.61	$2.58 \cdot 10^{-3}$
	4	118.89	$4.75 \cdot 10^{-3}$
	7	117.96	$6.40 \cdot 10^{-3}$
	10	114.75	$9.01 \cdot 10^{-3}$

A.2.3 $k_L a$ data points calculated from measurement data during sonication of water supersaturated with different gases in the batch reactor.

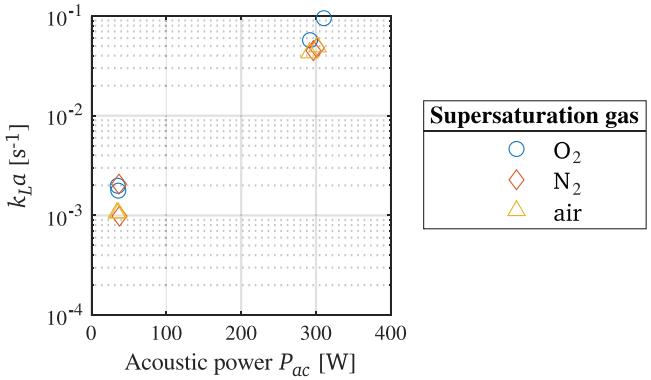

Figure A.1: Liquid-gas mass transfer coefficient, $k_L a$, during sonication of water supersaturated with different gases using using the SinapTec 20 kHz horn transducer at two different acoustic powers, P_{ac}.

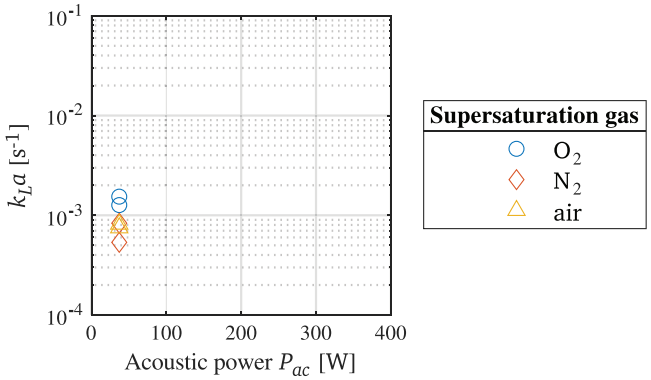

Figure A.2: Liquid-gas mass transfer coefficient, $k_L a$, during sonication of water supersaturated with different gases using the Meinhardt Ultrasonics 40 kHz plate transducer at maximum acoustic power, P_{ac} (100 % amplitude).

A.2.4 $k_L a$ data points calculated from measurement data during combination of sonication of TDG supersaturated water with selected operating parameters in the batch reactor.

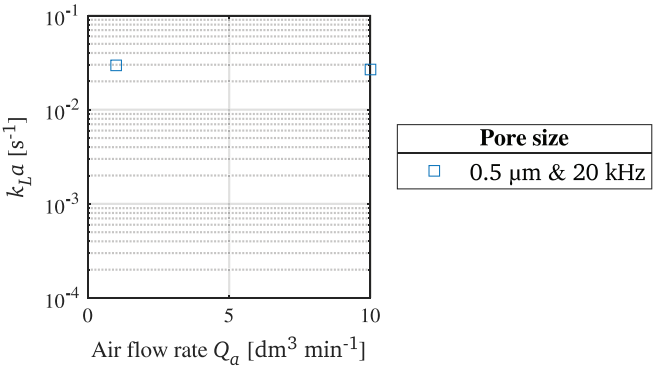

Figure A.3: Liquid-gas mass transfer coefficient, $k_L a$, during combination of sonication of TDG supersaturated water with air bubbling through the oxygenation stone at different air flow rates, Q_a.

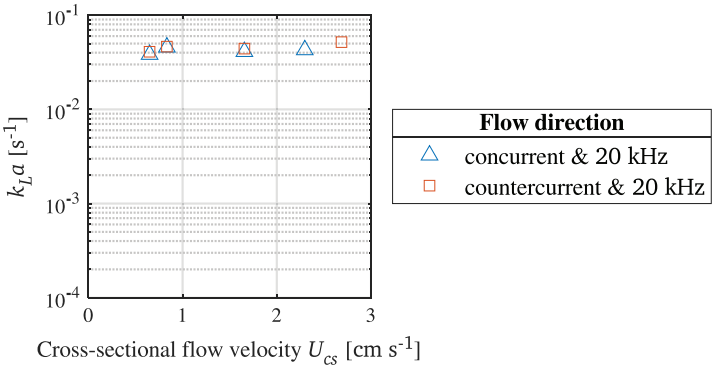

Figure A.4: Liquid-gas mass transfer coefficient, $k_L a$, during combination of sonication of TDG supersaturated water with con- and countercurrent flow circulation at different cross-sectional flow velocities, U_{cs}.

Table A.7: Measurement and $k_L a$ data during combination of ultrasonication and gas bubbling or flow circulation. The acoustic power is calculated using the regression curve for the 20 kHz transducer listed in Table 4.2.

Method & setting	Acoustic power [W]	Initial TDG saturation [%TDG]	$k_L a$ [s^{-1}]
Oxygenation stone			
1 dm^3 min^{-1}	395.22	113.05	$29.54 \cdot 10^{-3}$
10 dm^3 min^{-1}	410.39	108.70	$26.71 \cdot 10^{-3}$
Concurrent flow			
0.65 cm s^{-1}	405.05	114.76	$38.25 \cdot 10^{-3}$
0.83 cm s^{-1}	394.90	110.30	$45.69 \cdot 10^{-3}$
1.66 cm s^{-1}	401.68	112.47	$41.01 \cdot 10^{-3}$
2.30 cm s^{-1}	400.72	112.98	$42.80 \cdot 10^{-3}$
Countercurrent flow			
0.65 cm s^{-1}	390.73	113.07	$40.92 \cdot 10^{-3}$
0.83 cm s^{-1}	384.45	110.45	$46.39 \cdot 10^{-3}$
1.66 cm s^{-1}	388.01	113.36	$44.18 \cdot 10^{-3}$
2.69 cm s^{-1}	409.94	112.35	$51.78 \cdot 10^{-3}$

A.3 Additional data from experiments in the medium-sized test rig.

Table A.8: Measurement data from the parameter study on saturation increase in the pressure tank at the Waterpower Laboratory at NTNU.

Air overpressure [bar]	Bottom system pressure [bar absolute]	TDG saturation [%TDG h^{-1}]
0.5	1.49	0.45
	2.45	0.75
	2.44	2.07
	3.36	5.48
1.0	1.49	2.21
	2.46	10.59
	2.53	9.42
	3.46	7.98
1.5	1.49	1.85
	2.50	15.86
	2.54	15.97
	3.47	20.76
	3.46	19.36
	3.48	17.33
	3.53	16.00
	3.53	20.11
	3.51	19.85
	3.52	15.73
2.0	1.49	2.83
	2.52	17.45
	2.56	16.48
	3.50	18.47

Table A.9: Measurement and $k_L a$ data from ultrasonication experiments with the ultrasonic transducer installed between the first and second measurement station within the channel. The $k_L a$ values are calculated taking the *first* or the *previous* measurement station as basis.

Acoustic power [W]	Volumetric flow rate [$dm^3\ s^{-1}$]	Channel position [m]	Initial TDG saturation [%TDG]	Final TDG saturation [%TDG]	$k_L a$ (first) [s^{-1}]	$k_L a$ (previous) [s^{-1}]
128.87	3.53	0.00	182.65	N/A	N/A	N/A
		4.25	170.91	164.49	$1.34 \cdot 10^{-3}$	$1.34 \cdot 10^{-3}$
		9.25	173.20	161.52	$0.83 \cdot 10^{-3}$	$0.31 \cdot 10^{-3}$
		13.25	174.48	162.35	$0.53 \cdot 10^{-3}$	$0.09 \cdot 10^{-3}$
131.47	1.99	0.00	170.26	N/A	N/A	N/A
		4.25	161.19	157.91	$0.84 \cdot 10^{-3}$	$0.84 \cdot 10^{-3}$
		9.25	164.11	158.16	$0.38 \cdot 10^{-3}$	$0.02 \cdot 10^{-3}$
		13.25	161.14	158.13	$0.24 \cdot 10^{-3}$	$0.00 \cdot 10^{-3}$
137.07	1.49	0.00	171.54	N/A	N/A	N/A
		4.25	166.99	161.67	$0.48 \cdot 10^{-3}$	$0.48 \cdot 10^{-3}$
		9.25	167.95	156.09	$0.36 \cdot 10^{-3}$	$0.26 \cdot 10^{-3}$
		13.25	170.10	158.25	$0.20 \cdot 10^{-3}$	$0.10 \cdot 10^{-3}$
138.58	1.73	0.00	149.36	N/A	N/A	N/A
		4.25	165.05	160.00	$0.30 \cdot 10^{-3}$	$0.30 \cdot 10^{-3}$
		9.25	155.35	149.52	$0.19 \cdot 10^{-3}$	$0.61 \cdot 10^{-3}$
		13.25	158.76	154.79	$0.08 \cdot 10^{-3}$	$0.32 \cdot 10^{-3}$
315.87	1.88	0.00	175.30	N/A	N/A	N/A
		4.25	167.96	159.42	$0.97 \cdot 10^{-3}$	$0.97 \cdot 10^{-3}$
		9.25	171.39	146.76	$0.89 \cdot 10^{-3}$	$0.83 \cdot 10^{-3}$
		13.25	172.31	148.35	$0.54 \cdot 10^{-3}$	$0.12 \cdot 10^{-3}$
320.27	3.53	0.00	154.43	N/A	N/A	N/A
		4.25	172.67	159.46	$1.54 \cdot 10^{-3}$	$1.54 \cdot 10^{-3}$
		9.25	164.78	143.25	$1.42 \cdot 10^{-3}$	$2.07 \cdot 10^{-3}$
		13.25	168.03	147.95	$0.80 \cdot 10^{-3}$	$0.67 \cdot 10^{-3}$
539.35	3.51	0.00	167.85	N/A	N/A	N/A
		4.25	168.30	151.69	$2.08 \cdot 10^{-3}$	$2.08 \cdot 10^{-3}$
		9.25	166.41	143.62	$1.54 \cdot 10^{-3}$	$1.10 \cdot 10^{-3}$
		13.25	164.90	144.45	$0.96 \cdot 10^{-3}$	$0.12 \cdot 10^{-3}$

Continued on next page

Table A.9 – continued from previous page

572.07	2.23	0.00	173.47	N/A	N/A	N/A
		4.25	165.26	153.66	$1.52 \cdot 10^{-3}$	$1.52 \cdot 10^{-3}$
		9.25	170.79	143.54	$1.15 \cdot 10^{-3}$	$0.86 \cdot 10^{-3}$
		13.25	165.22	146.41	$0.66 \cdot 10^{-3}$	$0.26 \cdot 10^{-3}$
627.02	1.78	0.00	166.64	N/A	N/A	N/A
		4.25	160.62	151.40	$1.01 \cdot 10^{-3}$	$1.01 \cdot 10^{-3}$
		9.25	162.99	139.92	$0.90 \cdot 10^{-3}$	$0.83 \cdot 10^{-3}$
		13.25	163.27	145.84	$0.43 \cdot 10^{-3}$	$0.46 \cdot 10^{-3}$
638.56	1.86	0.00	151.79	N/A	N/A	N/A
		4.25	166.87	156.26	$0.70 \cdot 10^{-3}$	$0.70 \cdot 10^{-3}$
		9.25	160.87	139.58	$0.79 \cdot 10^{-3}$	$1.20 \cdot 10^{-3}$
		13.25	164.53	144.65	$0.44 \cdot 10^{-3}$	$0.41 \cdot 10^{-3}$

Table A.10: Measurement and $k_L a$ data from ultrasonication experiments with the ultrasonic transducer installed in the inlet of the degasification test rig. The $k_L a$ values are calculated taking the *inlet* measurement station as basis.

Acoustic power [W]	Volumetric flow rate [$dm^3\ s^{-1}$]	Channel position [m]	Initial TDG saturation [%TDG]	Final TDG saturation [%TDG]	$k_L a$ (inlet) [s^{-1}]
980.02	2.55	inlet	140.90	N/A	N/A
		0.00	145.94	121.67	$15.69 \cdot 10^{-3}$
		4.25	128.84	109.46	$5.85 \cdot 10^{-3}$
		9.25	158.86	138.23	$0.16 \cdot 10^{-3}$
		13.25	141.33	122.80	$0.89 \cdot 10^{-3}$
1444.22	2.40	inlet	139.50	N/A	N/A
		0.00	140.52	110.39	$28.48 \cdot 10^{-3}$
		4.25	125.50	111.70	$4.75 \cdot 10^{-3}$
		9.25	149.64	132.58	$0.42 \cdot 10^{-3}$
		13.25	137.56	117.19	$1.17 \cdot 10^{-3}$

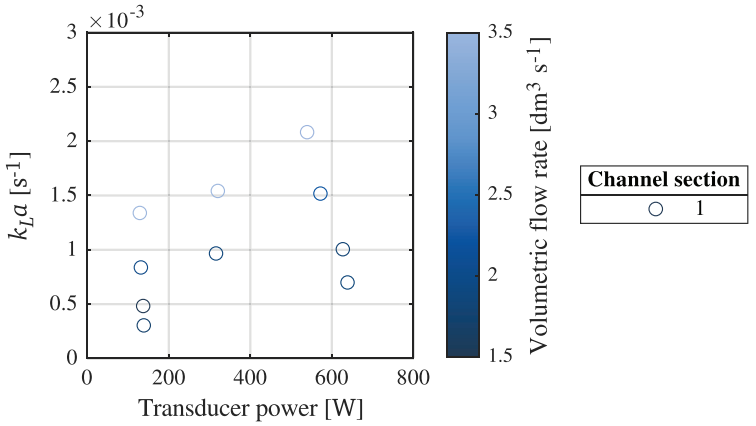

Figure A.5: Liquid-gas mass transfer coefficient, k_La, during ultrasonic degasification of TDG supersaturated, flowing water, calculated for the first section of the medium-sized test rig.

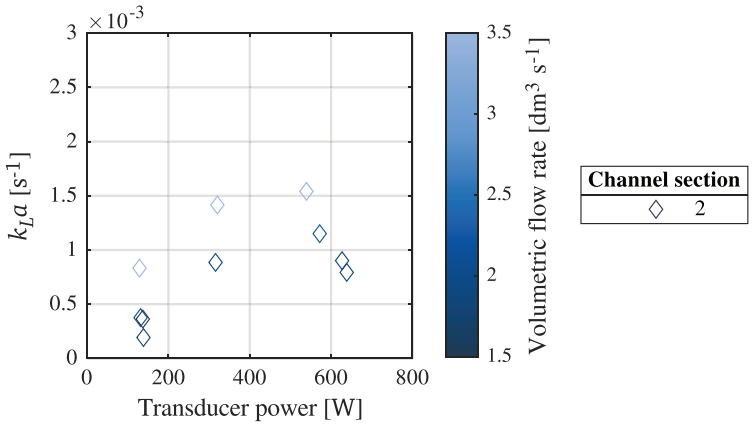

Figure A.6: Liquid-gas mass transfer coefficient, k_La, during ultrasonic degasification of TDG supersaturated, flowing water, calculated for the second section of the medium-sized test rig.

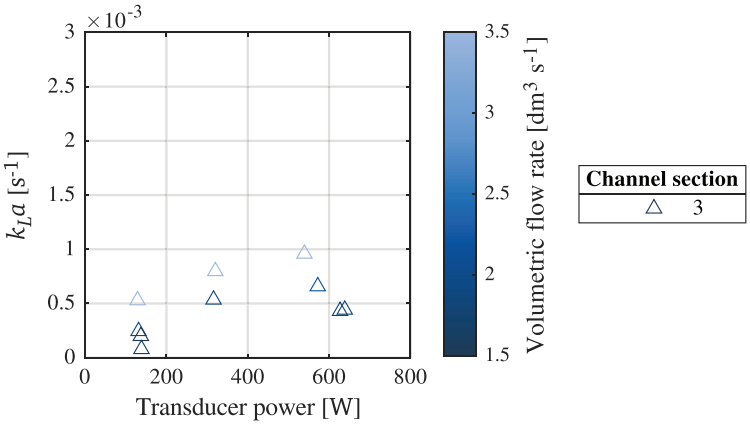

Figure A.7: Liquid-gas mass transfer coefficient, $k_L a$, during ultrasonic degasification of TDG supersaturated, flowing water, calculated for the third section of the medium-sized test rig.

Appendix B
Scientific publications

Within this appendix, the author's contribution to scientific journal publications is presented. A differentiation is made between the different status regarding publication of each paper. In addition, the abstracts are added, the Thesis author's contribution is explained, and eventual overlaps with parts of this Thesis are discussed. For publications that are in preparation, the presented texts are subject to possible adjustments.

B.1 Published

Li, P., Zhu, D. Z., Li, R., Wang, Y., Crossman, J. A., & **Kuhn, W. L.** (2022). Production of total dissolved gas supersaturation at hydropower facilities and its transport: A review. *Water Research, 223*, 119012. https://doi.org/10.1016/j.watres.2022.119012

Abstract Total dissolved gas supersaturation (TDG) is a common issue in hydropower facilities as a result of water conveyance structures that increase the amount of air entrainment from the atmosphere and dissolved into the water. Water with TDG supersaturation can negatively impact fish, aquatic invertebrates and their habitats. This study comprehensively reviewed the physical mechanisms of TDG generation and predictive TDG generation models at various facility types. To establish TDG mitigation strategies, it is essential to develop predictive tools for TDG generation that consider both facility geometry as well as the hydrology of the downstream environment. Applications of TDG prediction at different discharge modes included plunging flows, trajectory jets, plunging jets, free-falling jets, and submerged jets were discussed. TDG transport models in downstream rivers involving mixing and dissipation were introduced, which can be integrated with TDG generation models into a platform to describe TDG distribution in river systems. Subsequently, risk ranking procedures for assessing the degree of TDG risk on fish were provided. Potential measures for mitigating TDG supersatura-

tion were reviewed and included engineering, operational, and technical solutions. Outcomes from this review considered a diverse suite of studies on TDG issues in regulated rivers and allowed for recommendations to reduce uncertainties and improve environmental performance at facilities where TDG risks occur.

Contribution The author's contribution to this review consists of adding the issue of TDG supersaturation in the Norwegian context, as the focus was originally set on the generation of TDG supersaturation at high dams only. Furthermore, contributions to the mitigation strategies and the summary and future research needs were made. The author is therefore credited for investigation and writing - review and editing.

B.2 Submitted

Kuhn, W. L., Solemslie, B. W., Hihn, J.-Y., & Dahlhaug, O. G. (n.d.). Evaluating natural degassing in a river to create a baseline for comparison to technical degassing methods. *IOP Journal of Physics: Conference Series*.

Abstract In Norway, a recent project used a risk matrix to identify about 200 hydropower plants (11 % of the total number) of being in high risk of producing air-supersaturated water. The combined installed capacity of these hydropower plants amounts to more than 45 % of Norway's total installed hydropower capacity. Total dissolved gas (TDG) supersaturation in water is, dependent on the actual saturation value and the duration of the occurrence, lethal to certain types of fish and aquatic invertebrates. Natural degassing is highly dependent on the morphology of the downstream water system, but tends to be insufficiently slow with regard to lethality of TDG supersaturation. The Brokke power plant in southern Norway is known to create TDG supersaturation. Since 2012, continuous monitoring of the TDG level happens at the power plant outlet and several positions in the Otra river downstream. Measurement data has been evaluated and a method has been developed to calculate the liquid-gas mass transfer coefficient $k_L a$ as an indicator for the natural degassing efficiency within certain stretches of the river using assumptions for the river's geometry. The results are in agreement with former evaluation of the measurements. At the Waterpower Laboratory at NTNU in Trondheim, Norway, a test rig has been designed and instrumented to prove the effectiveness of degassing methods. An in-house pressure system is used to produce air-supersaturated water, which is then channeled through an open flume. At the flume's inlet, the degassing mechanism is installed. The TDG levels are monitored both upstream and downstream the degassing device. The $k_L a$ will be used to compare natural degassing in the river downstream Brokke power plant to the experimental degassing methods in the Waterpower Laboratory.

Contribution As main author, the contribution to this peer-review conference proceeding consists of conceptualization, methodology, software, validation, formal analysis, investigation, writing - original draft, and visualization. This publication consists in large parts of the establishment of a baseline liquid-gas mass transfer coefficient for natural degasification in a river, and is therefore similar to Chapter 3.2. Furthermore, a description of the degasification test rig is made, and the basic process of increasing the TDG saturation level using the in-house pressure system in the Waterpower Laboratory at NTNU is given. In this, the publication covers small parts of Section 5.1.

Piczak, M. L., McAllister, K., Bottoms, J., Grenier, G., Harper, M., Jetter, C. N., **Kuhn, W. L.**, Smith, D. A., Twardek, W. M., Sundt-Hansen, L. E., Crossman, J. A., Amundsen, P.-A., Cooke, S. J., Helland, I. P., & Power, M. (n.d.). A Winter Perspective on Fish in Hydropower Reservoirs. *Reviews in Fisheries Science and Aquaculture*.

Abstract Winter presents a challenge to aquatic organisms in north temperate regions, particularly ectothermic organisms such as fishes. The adverse conditions faced by organisms during the winter can be exacerbated by anthropogenic stressors, such as the operation of hydropower facilities and associated reservoirs. Despite emphasis on the study of hydropower impacts on fish populations, there is a paucity of studies examining the winter biology of fishes, and even fewer investigating fish in hydropower reservoirs in winter. Here, we synthesize the importance of winter and interactions with hydropower reservoirs on fish populations in north temperate regions. Hydropower reservoirs can drastically alter the environmental conditions of fish habitat during winter by changing systems from lotic to lentic, artificially modifying water levels and flow (including winter drawdowns), changing water temperatures (i.e., thermal stratification), decreasing light penetration, varying ice formation (earlier ice-on, later ice-off), and altering dissolved oxygen levels. These abiotic changes can have cascading impacts on fish and their food webs including: increased risk of mortality due to entrainment, reduced abundance of zooplankton and algae, altered fish growth and fitness, and increased risk of winter kill. With global climate changing the operation of reservoirs as a result of increased precipitation and water temperatures, fishes could be negatively impacted during the winter through shorter incubation periods (i.e., for salmonids), scoured habitats (e.g., for rearing) or altered rates of fish passage and entrainment. Taken together, the implications regarding hydropower reservoirs are far reaching with the potential to impact individual fish and the productivity of fish populations. With many questions still unanswered regarding the winter biology of fishes and many remaining unknowns stemming from climate change, we urge additional studies to contribute to more effective management of regulated ecosystems such as hydropower reservoirs to benefit fish and other aquatic life and the humans that interact with them.

Contribution This perspectives article is the outcome of a workshop, which took place in Canada in 2022 as a part of the HYCANOR project. Due to different scientific backgrounds of the participants, the workload was confined to certain sections, in which the authors were conducting research and investigation individually. The Thesis author contributed by writing a chapter about the dissolved oxygen (DO) content in hydropower reservoirs, and the effects winter has on it. Moreover, parts of the effects of climate change on hydropower reservoirs during winter were written. The author is credited with conceptualization, methodology, investigation, and writing - original draft.

B.3 In preparation

Kuhn, W. L., Solemslie, B. W., Hihn, J.-Y., & Dahlhaug, O. G. (n.d.). Decreasing the time to reach total dissolved gas supersaturation in water using air bubbling within a pressurized laboratory system. *Water Research* (target journal)

Abstract Total dissolved gas (TDG) supersaturation is an emerging problem in certain hydropower plants. Associated with spilling operations and floods, the number of occurrences of TDG supersaturation events is expected to rise due to shifting precipitation patterns in the northern hemisphere. Increased TDG saturation levels have potentially negative effects on fish and other aquatic lifeforms in the waterways downstream the hydropower plant. Therefore, research on degassing mechanisms in order to mitigate TDG supersaturation in the power plant prior to releasing water at the outlet is needed. A difficulty with researching degassing of TDG supersaturated, flowing water in larger laboratory conditions is the volume of water required for continuous experiments. At the Waterpower Laboratory at NTNU, different methods of supersaturating water with air within an in-house pressure system are investigated. Porous media at different air pressures is used to introduce microbubbles into water under different ambient pressures. The increase in TDG saturation level over time in a static volume of 15 m^3 water is compared to a volume of 38 m^3 water circulating in a closed loop. In the last case, air is introduced into the water at three different positions, while the static volume has only a single air inlet. The fastest way to increase the TDG saturation level in water is by circulating water in a closed loop and under high pressure. Turbulence within the flow helps distribute the introduced microbubbles, and the dissolution process shows a linear dependency on the pressure. The air inflow pressure has a peak at 1.5 bar above the system pressure. Below this pressure, the inflow of air into the water is too little to provide a fast increase of the TDG saturation level. A higher air pressure results in too much coalescence of bubbles before separation from the gas diffusers, which leads to slower dissolution due to a decrease in the interfacial area.

Contribution This publication is intended to take parts of Section 5.1, namely the process of TDG supersaturating water for laboratory experiments, but extends

the research by including a closed-loop water circulation to increase the available volume of TDG supersaturated water.

Kuhn, W. L., Solemslie, B. W., Hihn, J.-Y., & Dahlhaug, O. G. (n.d.). Methods to increase liquid-gas mass transfer for degasification purposes: A review. *Advanced Science* (target journal)

Abstract This paper provides a comprehensive review of methods aimed at enhancing liquid-gas mass transfer within solutions, offering a detailed overview of strategies for the removal or reduction of dissolved gas species within various fields of application. Degassing solutions frequently leads to improved product quality and increased production efficiency. Although a multitude of fields use similar degassing techniques, a broad overview of available methods has been lacking, as most industries only provide summaries of methods specific to their respective applications. To address this gap, a thorough review of publications spanning different domains was conducted, resulting in a systematic classification and comprehensive overview of contemporary methods. This compilation is poised to facilitate knowledge dissemination by granting various fields of application access to a diverse array of degassing methodologies. The process of solution degassing involves the extraction of one or multiple dissolved gas species from the liquid phase they inhabit. To achieve this, a diverse range of degassing methods employing distinct mechanisms have been developed and are employed across multiple industries. Methods to enhance liquid-gas mass transfer are categorized by their applied principle, resulting in distinct categories: chemical degasification, increased surface contact or specific interface, modified thermodynamic conditions, and mechanophysical techniques. Within those, different methods are discussed, and their respective application fields are described. This results in a comprehensive view of available degassing methods, tracing their historical evolution and enumerating the industries that employ them.

Contribution The review will take over large parts of the introduction to liquid-gas mass transfer and its enhancement, which are presented in Section 2.2 and 2.3.2, respectively.

Kuhn, W. L., Solemslie, B. W., Hihn, J.-Y., & Dahlhaug, O. G. (n.d.). Comparing and combining methods that enhance liquid-gas mass transfer in a batch reactor: ultrasonic degassing, aeration by gas bubbling, and liquid agitation. *Ultrasonics Sonochemistry* (target journal)

Abstract The present study investigates methods to enhance liquid-gas mass transfer in total dissolved gas (TDG) supersaturated water. Using a two-part experimental setup, water is first supersaturated using air, followed by an evaluation of the influence of various operating parameters on the volumetric liquid-gas mass

transfer coefficient ($k_L a$) in a batch reactor. The tested methods to enhance the degasification are: aeration by gas bubbling, agitation by flow circulation, and ultrasonic degassing. Changes in the porosity of gas diffusers and in the air pressure were applied for the first method, the circulation flow velocity was changed in case of the second method, and different ultrasonic frequencies and powers were used in the third case. Finally, a combination of the different methods was conducted to evaluate promoting effects on the liquid-gas mass transfer. High-power ultrasound proves the most potent technique overall. Only a combination with countercurrent flow leads to a further increase in the mass transfer. Combining gas bubbling and sonication elevates $k_L a$ values as well compared to gas bubbling alone, but to a lesser degree. The results indicate that power ultrasound, in combination with selected parameters, presents a compelling approach for efficient degasification of TDG supersaturated water, and offer practical insights for applications.

Contribution Here, large parts of Chapter 4, including the described methods, results, and discussion are taken over. The development of a model is left out.